

Diss. ETH No. 26251

ATTOSECOND ELECTRON DYNAMICS IN III-V SEMICONDUCTORS

A thesis submitted to attain the degree of
DOCTOR OF SCIENCES of ETH ZURICH
(Dr. sc. ETH Zurich)

presented by
FABIAN SCHLÄPFER
MSc ETH Physics, ETH Zurich

born on 11.11.1989

citizen of Herisau (AR)

accepted on the recommendation of
Prof. Dr. Dr. h. c. Ursula Keller, examiner
Prof. Dr. Adrian Cavaliere, co-examiner
PD. Dr. Lukas Gallmann, co-examiner

2019

Contents

Contents	i
List of Figures	iv
List of Tables	vi
List of Symbols and Acronyms	vii
Publications	xi
Journal Papers	xi
Conference Papers	xii
Abstract	xvii
Kurzfassung (German)	xix
1 Motivation	1
2 Attosecond Science	7
2.1 High-order Harmonic Generation	7
2.1.1 Single Atom Response	8
2.1.2 Attosecond Pulse Train	9
2.1.3 Single Attosecond Pulse	10
2.2 Attosecond Measurement Techniques	12
2.2.1 Photoelectron Spectroscopy	12
2.2.1.1 RABBITT	12
2.2.1.2 Attosecond Streak Camera	14
2.3 Absorption Spectroscopy	16
2.3.1 Membrane Thickness Limitation	18
3 Experimental Setup	21
3.1 Laser System	21

3.1.1	Ti-Sapphire Laser	21
3.1.2	Optical Parametric Amplifier	23
3.1.3	Pulse Compression	24
3.2	Attoline	25
3.3	Nano-Membrane Fabrication	30
4	Gouy Phase Shift	33
4.1	Gouy Phase Shift for Annular Beam Profiles in Attosecond Experiments	35
4.1.1	Introduction	35
4.1.2	Setup	37
4.1.3	Phase Measurement	39
4.1.4	Equivalent Photoionization Delays	45
4.1.5	Conclusion	46
5	Attosecond Transient Absorption Spectroscopy	49
5.1	Core Level Spectroscopy	51
5.2	Band Properties of GaAs and $\text{Al}_{0.8}\text{Ga}_{0.2}\text{As}$	52
5.3	Relation between Absorbance and Dielectric Function	53
5.4	Attosecond Optical-Field-Enhanced Carrier Injection into the GaAs Conduction Band	55
5.5	Attosecond Carrier Dynamics in $\text{Al}_{0.8}\text{Ga}_{0.2}\text{As}$	66
5.5.1	$\text{Al}_{0.8}\text{Ga}_{0.2}\text{As}$ Sample	66
5.5.2	Static XUV Absorption	67
5.5.3	Transient Absorption Spectroscopy	68
5.5.3.1	Energy Dependence of Oscillation Delay	69
5.5.4	Conclusion of Carrier Dynamics in $\text{Al}_{0.8}\text{Ga}_{0.2}\text{As}$	71
6	Attosecond Pump-Probe Beamline involving Two-IR Colors	73
6.1	Phase Stabilization of an Attosecond Beamline combining Two IR Colors	75
6.1.1	Introduction	76
6.1.2	Laser and Pump-Probe Schemes	77
6.1.3	Phase Stabilization Scheme	79
6.1.4	Active Interferometric Stabilization (AIS) Algorithm	82
6.1.5	Measurement	84
6.1.6	Conclusion	86
7	Conclusion and Outlook	89
A	Relation between Absorbance and Dielectric Function	93
B	Supplementary Information	99
B.1	Experimental Methods	100
B.1.1	Sample Properties and Preparation	100
B.1.2	Infrared Pulse Parameters	100
B.1.3	Single Attosecond Pulse (SAP) vs. Attosecond Pulse Train (APT)	102

B.1.4	Pump-Probe Delay Calibration	103
B.1.5	Phase and Delay Extraction	105
B.2	Theoretical Methods	107
B.2.1	First-Principles Electron Dynamics Simulation in the Time-Domain	107
B.2.2	Role of the Propagation Effect	108
B.2.3	Pump Intensity Dependence	110
B.2.4	Probe-Decomposition based on Houston States	111
B.2.5	Simplified 3-Band Model	112
B.2.5.1	Intra- and Inter-Band Limit	114
B.2.5.2	Heavy-Hole Valence Band	114
B.2.5.3	Conduction Band Population	115
B.2.6	Spin-Orbit Splitting	116
B.2.7	Multi-Photon Resonant Pump Regime	117
	Bibliography	119
	Curriculum Vitæ	131
	Acknowledgements	133

List of Figures

2.1	Typical HHG spectrum	8
2.2	HHG process illustrated with a semiclassical three-step model	9
2.3	Temporal and spectral shape of a typical APT and SAP	10
2.4	Polarization gating technique	11
2.5	Illustration of the RABBITT technique	13
2.6	Attosecond streaking spectroscopy	15
2.7	Attosecond transient absorption spectroscopy	16
2.8	Absorption in GaAs	17
2.9	Thickness-dependent XUV transmission of a GaAs membrane	18
3.1	Overview of the laser system	22
3.2	Optical parametric amplifier	24
3.3	Attoline overview	26
3.4	Illustration of different laser configurations	27
3.5	Overview of the front-end chambers	28
3.6	First experimental chamber and XUV spectrometer	29
3.7	IR beam profile	30
3.8	Nano-membrane fabrication	31
4.1	Schematic of the two-target attosecond beamline	38
4.2	Total measured electron counts of ATI spectra from ethylene as a function of the second chamber position	39
4.3	RABBITT traces	41
4.4	Energy dependence of oscillation phase	43
4.5	Gouy phase shift	44
4.6	Delay	47
5.1	Band structure and bandgap	52
5.2	Pump-probe mechanism in GaAs	57
5.3	Attosecond transient absorption spectroscopy	59
5.4	Simulated energy- and delay-dependent change of the absorbance	62
5.5	Time evolution of the real electron population n_{CB} in the CB extracted from the three-band model	63
5.6	Picture of a free-standing 100-nm-thick $\text{Al}_{0.8}\text{Ga}_{0.2}\text{As}$ membrane	67
5.7	Measured static absorption of 100-nm GaAs and $\text{Al}_{0.8}\text{Ga}_{0.2}\text{As}$	68

5.8	Transient absorbance change of an $\text{Al}_{0.8}\text{Ga}_{0.2}\text{As}$ and GaAs membrane . . .	69
5.9	Energy dependence of the oscillation delay	70
6.1	Ti:sapphire laser system, OPA and pump-probe scheme	79
6.2	Delay compensation	82
6.3	Schematic of signal processing in the active phase stabilization system . .	84
6.4	Attosecond streaking experiment as a proof-of-principle demonstration .	85
B.1	Injected carrier population vs. laser intensity	101
B.2	Single attosecond pulse reconstruction	102
B.3	Attosecond transient absorption spectroscopy measurement performed with an attosecond pulse train	103
B.4	Delay calibration	104
B.5	Phase and delay extraction	106
B.6	Propagation effect	109
B.7	First-principles simulation of absorption modulation for two IR pump intensities	110
B.8	Decomposition of the first-principles signal	112
B.9	Extraction of matrix element ρ_{vc}	114
B.10	Light-hole vs. heavy-hole valence band	115
B.11	Influence of core-level splitting	116
B.12	Number of carriers excited into the conduction band of GaAs by a 3- photon resonant pump pulse	117

List of Tables

5.1	Overview of core level binding energies	51
B.1	Laser parameters of the infrared pulse in vacuum	101

List of Symbols and Acronyms

Symbols

A	vector potential.
Abs	absorbance.
b	band index.
c	speed of light in vacuum.
d	dipole matrix element.
E	electric field.
e	electron charge.
E	energy.
E_{gap}	energy gap.
E_{kin}	kinetic energy.
ε	polarization.
$\varepsilon(\omega)$	dielectric function.
\hbar	Planck constant.
\hat{H}	Hamiltonian.
I	intensity.
I_p	ionization potential.
I_{peak}	peak intensity.
k	crystal momentum.
k_0	photon wave number in vacuum.
\tilde{k}	photon wave number in a solid.

L	membrane thickness.
λ	wavelength.
m_e	electron mass.
n	refractive index.
p	electron momentum.
p_{ij}	momentum matrix element.
φ_{CEP}	carrier envelope phase.
T	transmission.
τ	delay.
u_{bk}	Bloch orbital.
u_{bk}^H	Houston state.
U_p	ponderomotive energy.
v	potential.
\bar{v}	velocity.
ω	angular frequency.

Acronyms

AIS	active interferometric stabilization.
Al	aluminum.
AOM	acousto-optic modulator.
AOPDF	acousto-optic programmable dispersive filter.
APT	attosecond pulse train.
ATAS	attosecond transient absorption spectroscopy.
ATI	above-threshold-ionization.
BS	beam splitter.
CB	conduction band.
CCD	charge-coupled device.
CEP	carrier-envelope phase.
CM	center of mass.
CMA	central momentum approximation.
CPA	chirped pulse amplifier.
cw	continuous wave.
DFKE	dynamical Franz-Keldysh effect.
DFT	density functional theory.
DM	dichroic mirror.
DPSSL	diode-pumped solid state laser.
ePIE	extended ptychographic iterative engine.
EWP	electron wave packet.
FP	first-principle.
FROG	frequency-resolved optical gating.
FROG-CRAB	frequency-resolved optical gating for complete reconstruction of attosecond bursts.
FWHM	full width at half maximum.
GaAs	gallium arsenide.
GDD	group delay dispersion.
HH	high-order harmonic.
HHG	high-order harmonic generation.
IR	infrared.
MBE	molecular beam epitaxy.
NIR	near-infrared.
OPA	optical parametric amplifier.

PG	polarization gating.
PID	proportional-integral-derivative.
RABBITT	reconstruction of attosecond beating by interference of two-photon transitions.
rms	root mean square.
SAP	single attosecond pulse.
SB	sideband.
SH	second harmonic.
SPM	self-phase modulation.
TDDFT	time-dependent density functional theory.
Ti-sapphire	titanium-doped sapphire.
TOF	time-of-flight.
UV	ultraviolet.
VB	valence band.
XUV	extreme ultraviolet.

Publications

Parts of this doctoral thesis are published in the following journal papers and conference contributions.

Journal Papers

1. **F. Schlaepfer**,* A. Ludwig,* M. Lucchini, L. Kasmi, M. Volkov, L. Gallmann and U. Keller, "Gouy phase shift for annular beam profiles in attosecond experiments", *Optics Express* 25(4), 3646-3655 (2017), doi.org/10.1364/OE.25.003646, *authors with equal contribution.
2. **F. Schlaepfer**, M. Lucchini, S. A. Sato, M. Volkov, L. Kasmi, N. Hartmann, A. Rubio, L. Gallmann and U. Keller, "Attosecond optical-field-enhanced carrier injection into the GaAs conduction band", *Nature Physics* 14(6), 560-564 (2018), doi.org/10.1038/s41567-018-0069-0.
3. S. A. Sato, M. Lucchini, M. Volkov, **F. Schlaepfer**, L. Gallmann, U. Keller and A. Rubio, "Role of intraband transitions in photocarrier generation", *Physical Review B* 98(3), 035202 (2018), doi.org/10.1103/PhysRevB.98.035202.
4. M. Volkov, J. Pupeikis, C. R. Phillips, **F. Schlaepfer**, L. Gallmann and U. Keller, "Reduction of laser-intensity-correlated noise in

- high-harmonic generation”, *Optics Express* 27(6), 7886-7895 (2019), doi.org/10.1364/OE.27.007886.
5. **F. Schlaepfer**,* M. Volkov,* N. Hartmann, A. Niedermayr, Z. Schumacher, L. Gallmann and U. Keller, “Phase stabilization of an attosecond beamline combining two IR colors”, *Optics Express* 27(16), 22385-22392 (2019), doi.org/10.1364/OE.27.022385, *authors with equal contribution.
 6. M. Volkov, S. A. Sato, **F. Schlaepfer**, L. Kasmi, N. Hartmann, M. Lucchini, L. Gallmann, A. Rubio and U. Keller, “Attosecond screening dynamics mediated by electron-localization in transition metals”, *Nature Physics* (2019), doi.org/10.1038/s41567-019-0602-9.
 7. N. Hartmann, S. Battacharyya, **F. Schlaepfer**, M. Volkov, Z. Schumacher, M. Lucchini, L. Gallmann, U. Rothlisberger and U. Keller, “Ultrafast nuclear dynamics of the acetylene cation $C_2H_2^+$ and its impact on the IR induced C-H bond breaking efficiency”, *Physical Chemistry Chemical Physics* 21, 18380-18385 (2019), doi.org/10.1039/c9cp03138c.
 8. M. Lucchini, D. Baykusheva, L. Kasmi, H. Volkmann, V. P. Majety, M. Volkov, **F. Schlaepfer**, A. Ludwig, Z. Schumacher, L. Gallmann, H.J. Wörner, A. Scrinzi and U. Keller, “Multi-electron effect on attosecond molecular photoionization delays”, submitted to *New Journal of Physics* (2019).

Conference Papers

1. **F. Schlaepfer**, N. Hartmann, L. Kasmi, M. Volkov, A. Ludwig, M. Lucchini, P. Kraus, L. Gallmann, H. J. Wörner and U. Keller, “Attoline: 1) Gouy Phase Shift for Annularly Truncated Beams, 2) Ultrafast Fragmentation Dynamics of Acetylene”, *Molecular Ultrafast Science and Technology (MUST) Annual Meeting (7th)*, Grindelwald, Switzerland (2017). (Poster).
2. **F. Schlaepfer**, A. Ludwig, M. Lucchini, L. Kasmi, M. Volkov, L. Gallmann and U. Keller, “Gouy Phase Shift for Annularly Truncated Beam Profiles in Attosecond Pump-Probe Measurements”, *Con-*

-
- ference on Lasers and Electro-Optics (CLEO)*, San José, USA (2017). (Poster).
3. **F. Schlaepfer**, A. Ludwig, M. Lucchini, L. Kasmi, M. Volkov, L. Gallmann and U. Keller, “Gouy Phase Effects in Attosecond Photoemission Delay Measurements Using Truncated Beams”, *Conference on Lasers and Electro-Optics/Europe and European Quantum Electronics Conference (CLEO/Europe-EQEC)*, Munich, Germany (2017). (Talk).
 4. **F. Schlaepfer**, M. Lucchini, S. A. Sato, M. Volkov, L. Kasmi, N. Hartmann, A. Rubio, L. Gallmann, and U. Keller, “Attosecond carrier dynamics in gallium arsenide induced by intense resonant near-infrared laser pulses”, *Molecular Ultrafast Science and Technology (MUST) Annual Meeting (8th)*, Grindelwald, Switzerland (2018). (Talk).
 5. N. Hartmann, S. Bhattacharyya, **F. Schlaepfer**, L. Kasmi, M. Volkov, M. Lucchini, L. Gallmann, U. Röthlisberger, and U. Keller, “Photoionization induced ultrafast fragmentation dynamics of acetylene”, *Molecular Ultrafast Science and Technology (MUST) Annual Meeting (8th)*, Grindelwald, Switzerland (2018). (Poster).
 6. M. Lucchini, D. Baykusheva, L. Kasmi, M. Volkov, **F. Schlaepfer**, A. Ludwig, L. Gallmann, H. J. Wörner, and U. Keller, “Electron correlation effects in attosecond photoionization from a CO₂ molecule”, *Molecular Ultrafast Science and Technology (MUST) Annual Meeting (8th)*, Grindelwald, Switzerland (2018). (Poster).
 7. U. Keller, **F. Schlaepfer**, M. Volkov, S. A. Sato, M. Lucchini, L. Gallmann, and A. Rubio, “New physical insight gained in condensed matter with attosecond transient absorption spectroscopy”, *International Conference on Ultrafast Phenomena*, Hamburg, Germany (2018). (Invited talk).
 8. L. Gallmann, M. Lucchini, **F. Schlaepfer**, M. Volkov, S. A. Sato, L. Kasmi, N. Hartmann, A. Ludwig, J. Herrmann, Y. Shinohara, K. Yabana, A. Rubio, and U. Keller, “Attosecond electron dynamics in dielectrics, semiconductors and metals driven by optical fields”,

Non-equilibrium Dynamics of Condensed Matter in the Time Domain, Kerkrade, Netherland (2018). (Invited talk).

9. **F. Schlaepfer**, M. Lucchini, S. A. Sato, M. Volkov, L. Kasmı, N. Hartmann, A. Rubio, L. Gallmann and U. Keller, "Optically driven attosecond electron dynamics in gallium arsenide", *International Symposium of Ultrafast Science*, Lausanne, Switzerland (2018). (Poster).
10. N. Hartmann, B. Mignolet, S. Battacharyya, **F. Schlaepfer**, M. Volkov, Z. Schumacher, M. Lucchini, L. Gallmann, F. Remacle, U. Roethlisberger and U. Keller, "Ultrafast nuclear dynamics of the acetylene cation $C_2H_2^+$ and its impact on the IR induced C-H bond breaking efficiency", *International Symposium of Ultrafast Science*, Lausanne, Switzerland (2018). (Poster).
11. M. Volkov, S. A. Sato, **F. Schlaepfer**, L. Kasmı, N. Hartmann, M. Lucchini, L. Gallmann, A. Rubio and U. Keller "Probing attosecond collective electron dynamics in metals", *Molecular Ultrafast Science and Technology (MUST) Annual Meeting (9th)*, Grindelwald, Switzerland (2019). (Poster).
12. N. Hartmann, B. Mignolet, S. Battacharyya, **F. Schlaepfer**, M. Volkov, Z. Schumacher, M. Lucchini, L. Gallmann, F. Remacle, U. Rothlisberger and U. Keller, "Ultrafast nuclear dynamics of the acetylene cation $C_2H_2^+$ and its impact on the IR induced C-H bond breaking efficiency", *6th Banff Meeting on Structural Dynamics*, Alberta, Canada (2019). (Talk).
13. M. Volkov, J. Pupeikis, C. R. Phillips, **F. Schlaepfer**, L. Gallmann and U. Keller, "Reduction of Laser-Intensity-Related Noise in High-Harmonic Generation", *Conference on Lasers and Electro-Optics (CLEO)*, San José, USA (2019). (Talk).
14. **F. Schlaepfer**, M. Lucchini, S. A. Sato, M. Volkov, L. Kasmı, N. Hartmann, A. Rubio, L. Gallmann and U. Keller, "Optically driven attosecond electron dynamics in III-V semiconductors", *Conference on Lasers and Electro-Optics/Europe and European Quantum Electronics Conference (CLEO/Europe-EQEC)*, Munich, Germany (2019). (Talk).

-
15. M. Volkov, S. A. Sato, **F. Schlaepfer**, L. Kasmı, N. Hartmann, M. Lucchini, L. Gallmann, A. Rubio and U. Keller, "Attosecond electron localization and screening dynamics in metals", *Conference on Lasers and Electro-Optics/Europe and European Quantum Electronics Conference (CLEO/Europe-EQEC)*, Munich, Germany (2019). (Talk).
 16. M. Volkov, J. Pupeikis, C. R. Phillips, **F. Schlaepfer**, L. Gallmann and U. Keller, "Reducing spectral fluctuations of high-harmonics with indirect balanced detection scheme", *Conference on Lasers and Electro-Optics/Europe and European Quantum Electronics Conference (CLEO/Europe-EQEC)*, Munich, Germany (2019). (Poster).
 17. **F. Schlaepfer**, M. Lucchini, S. A. Sato, M. Volkov, L. Kasmı, N. Hartmann, A. Rubio, L. Gallmann and U. Keller, "Attosecond photocarrier excitation in III-V semiconductors", *7th International Conference on Attosecond Science and Technology (ATTO2019)*, Szeged, Hungary (2019). (Poster).
 18. M. Volkov, S. A. Sato, **F. Schlaepfer**, N. Hartmann, L. Kasmı, M. Lucchini, L. Gallmann, A. Rubio and U. Keller, "Attosecond electron localization in metallic titanium", *7th International Conference on Attosecond Science and Technology (ATTO2019)*, Szeged, Hungary (2019). (Poster).
 19. M. Volkov, J. Pupeikis, C. R. Phillips, **F. Schlaepfer**, L. Gallmann and U. Keller, "Effectively balanced detection scheme for attosecond transient absorption spectroscopy", *7th International Conference on Attosecond Science and Technology (ATTO2019)*, Szeged, Hungary (2019). (Poster).

Abstract

Shortly after the turn of the millennium, laser pulses with a sub-femtosecond duration were generated for the first time and a new research field called *attosecond science* was launched. Attosecond science studies the dynamics of electrons in atoms, molecules and solids on their natural attosecond timescale to reveal fundamental physical and chemical processes. A deep understanding of the ultrafast electron motion in condensed matter is in particular of great interest for the development of the next generation of high-speed electronics.

In the framework of this doctoral thesis, attosecond transient absorption spectroscopy measurements were performed to resolve ultrafast carrier dynamics induced by intense few-cycle infrared (IR) laser pulses in III-V semiconductors (GaAs and $\text{Al}_{0.8}\text{Ga}_{0.2}\text{As}$). Extreme-ultraviolet (XUV) pulses with a sub-femtosecond duration were used as a probe. During the light-matter interaction, two mechanisms can be induced by the optical pump: intraband motion and interband transitions of the charge carriers. The distinct role of the two processes is highly debated and not fully understood. Supported by state-of-the-art simulations, we found that intraband motion is the dominating process during the pump-interaction. Our findings represent an important step towards controlling electron dynamics in solids on the sub-femtosecond timescale.

Further, this thesis presents a detailed study of the Gouy phase shift of an annularly truncated IR beam using a two-foci beamline. In attosecond

pump-probe setups, the collinear recombination of the XUV radiation and the IR beam is commonly done with a center-hole mirror due to the lack of suitable dichroic optics. This results in a donut-like IR beam profile. The performed study demonstrates that the Gouy phase of an annular IR beam deviates significantly from the one of an ideal Gaussian beam and that it can have a non-negligible influence on attosecond measurements. Careful calibration of the Gouy phase can improve the measurement accuracy, but also prevents the extraction of unphysical time information.

Finally, this thesis discusses the implementation of a tunable optical parametric amplifier into the laser system and demonstrates a novel approach to actively stabilize the pump-probe phase in an attosecond beamline with two separate IR-colors involved, without the need of an auxiliary laser. The setup upgrade allows tuning the IR-wavelength used in the pump-probe experiment fully decoupled from the high-order harmonic generation. This enables a wide range of new experiments, e.g. studying the wavelength-dependence of pump-induced carrier dynamics.

Kurzfassung (German)

Kurz nach der Jahrtausendwende wurden erstmals Laserpulse mit einer Dauer unter einer Femtosekunde erzeugt. Dies war die Geburtsstunde eines neuen Forschungsgebiets, der *Attosekundenphysik*. Diese untersucht die Dynamik der Elektronen in Atomen, Molekülen und Festkörpern auf der Attosekunden-Zeitskala, um grundlegende physikalische und chemische Prozesse zu erklären. Ein fundamentales Verständnis der ultraschnellen Elektronenbewegungen in Festkörpern ist insbesondere für die Entwicklung einer nächsten Generation von Hochgeschwindigkeitselektronik von grossem Interesse.

Im Rahmen dieser Doktorarbeit wurden Absorptionsspektroskopie-Messungen mit einer Zeitauflösung im Attosekundenbereich an III-V-Halbleitern (GaAs und $\text{Al}_{0,8}\text{Ga}_{0,2}\text{As}$) durchgeführt. Die ultraschnellen Ladungsträgerdynamiken wurden durch intensive, kurze Laserpulse im infraroten (IR) Wellenlängenbereich induziert und danach mit Hilfe von extrem-ultravioletten (XUV) Attosekunden-Pulsen zeitlich aufgelöst beobachtet. Während der Wechselwirkung zwischen Licht und Materie können zwei Vorgänge durch den optischen Puls induziert werden: Intraband-Bewegungen und Interband-Übergänge der Ladungsträger. Die individuelle Bedeutung der beiden Prozesse ist nicht vollständig geklärt und wird kontrovers debattiert. Unterstützt durch modernste Simulationen konnten wir demonstrieren, dass die Intraband-Bewegung der dominierende Prozess während der Anregungsinteraktion ist. Unsere Ergebnisse sind ein wichtiger Schritt in Richtung Petahertz-Elektronik, welche danach strebt,

den elektrischen Zustand eines Festkörpers auf der Zeitskala unter einer Femtosekunde zu modifizieren.

Diese Doktorarbeit beinhaltet zudem eine detaillierte Studie der Gouy-Phase eines ringförmig abgeschnittenen IR-Laserstrahls, durchgeführt an einem Experimentaufbau mit einem Doppelfokus. In Anreg-Abtast-Experimenten mit Attosekunden-Auflösung wird die kollineare Rekombination der XUV-Strahlung mit dem IR-Strahl üblicherweise mit Hilfe eines Lochspiegels durchgeführt. Dies ist notwendig aufgrund des Fehlens geeigneter dichroitischer Optik und resultiert in einem ringförmigen IR-Strahlprofil. Die durchgeführten Messungen haben aufgezeigt, dass die Gouy-Phase eines solchen IR-Strahls erheblich von der eines idealen Gauss-Strahls abweicht und dass dies einen nicht zu vernachlässigenden Einfluss auf Attosekunden-Messungen haben kann. Eine genaue Kalibrierung der Gouy-Phase kann die Messgenauigkeit verbessern und verhindert die Extraktion unphysikalischer Zeitinformationen.

Schliesslich wird in dieser Arbeit die Implementierung eines abstimmbaren optisch parametrischen Verstärkers in das vorhandene Lasersystem diskutiert. Dabei wird eine neue Technik zur aktiven Stabilisierung der Anreg-Abtast-Phase in einem Experimentaufbau mit zwei unterschiedlichen IR-Wellenlängen präsentiert. Erwähnenswert ist, dass die demonstrierte Technik, anders als bisher bekannte Methoden, keinen zusätzlichen Hilfslaser benötigt. Das neue Lasersystem ermöglicht es, die IR-Wellenlänge im Anreg-Abtast-Experiment zu variieren ohne dabei die Erzeugung der höheren Harmonischen zu beeinflussen. Dies ermöglicht eine Vielzahl neuer Experimente, zum Beispiel die Untersuchung der Abhängigkeit der Elektronendynamiken von der Wellenlänge der Anregungspulse.

Chapter 1

Motivation

One attosecond is a billionth of a billionth of a second ($1 \text{ as} = 10^{-18} \text{ s}$). In other words, one attosecond in one second corresponds to one second in 31.71 billion years. Processes that occur on this ultrafast attosecond timescale are electron dynamics in atoms, molecules and condensed matter. For example, the oscillation period of a wavepacket in a two-level system is given by $\tau = h/\Delta E$ [1]. h is the Planck constant ($\sim 4.1 \text{ eV}\cdot\text{fs}$) and ΔE the energy spacing of the two eigenstates. A level spacing of a few electronvolts results in a femtosecond ($1 \text{ fs} = 10^{-15} \text{ s}$) to even sub-fs period. Since electron motion forms the basis of physical and chemical reactions, it is of great interest to resolve their dynamics on the natural attosecond timescale.

For a long time, the observation of dynamical processes has been limited to the temporal resolution of the human eye. With the invention of photography in the late 19th century, faster processes could be captured. The technology of light flashes has also been used in pump-probe experiments to study microscopic dynamics. In 1864, August Toepler investigated the evolution of air shock waves, which were generated by an electric spark and subsequently probed by a delayed light flash [2]. Even though this technology has been continuously improved over the next decades, the dynamics that could be resolved was ultimately limited by the nanosecond-long ($1 \text{ ns} = 10^{-9} \text{ s}$) pulse duration of the incoherent light sources. It was the invention of the laser by Theodore Maiman in 1960 [3], which revolutionized the real-time observation of ultrafast microscopic

processes. The breakthrough discovery of Maiman followed by the development of mode-locked laser sources enabled the generation of shorter and shorter light pulses, down to a few femtosecond duration [4]. Within only three decades, the temporal resolution of time-resolved studies could be reduced from the nano- to the few-femtosecond regime, the timescale of molecular dynamics. In 1987, the breakage of a chemical bond could be observed in real-time for the first time [5,6]. For this and other pioneering works in the field of femtochemistry, Ahmed Zewail was awarded the Noble Prize in Chemistry in 1999.

The transition from the femto- to the attosecond regime represents another milestone in the history of ultrafast spectroscopy. The compression of a light pulse is ultimately limited by the duration of one optical field cycle. For an 800-nm pulse from a titanium-doped sapphire (Ti-sapphire) laser, this corresponds to 2.7 fs. Thus, a novel technology was required for the generation of sub-fs pulses. The first train of attosecond pulses was demonstrated just after the turn of the millennium [7]. The pulse generation is based on an up-conversion process of the infrared (IR) radiation into the extreme ultraviolet (XUV) energy regime [8,9]. To date, pulse durations down to 43 as have been demonstrated [10].

Often, attosecond beamlines combine an IR pulse with an attosecond XUV pulse in a pump-probe scheme. The pump pulse induces a dynamical process, which is probed by the delayed probe pulse. Depending on the investigated process, either the IR or XUV pulse is used as the pump or probe. By scanning the delay between the two pulses, a "movie" of the induced process can be recorded to resolve the dynamics in real-time. Applying this technique with sub-femtosecond resolution allowed to reveal many fundamental processes, both in atoms and in molecules. Examples are the motion of valence electrons in atomic krypton ions [11], photoemission time delays in neon [12], charge migration in ionized iodoacetylene [13] and electron dynamics in polyatomic molecules [14], to name just a few.

In 2007, the first attosecond study of condensed matter has been performed by Cavalieri *et al.* using a tungsten crystal [15]. They employed photoemission spectroscopy and observed a relative time delay of around

100 as between electrons originating from a core level and those emitted from a conduction-band state. Further studies based on the same measurement approach investigated the influence of the band structure during the photoemission process [16, 17] and the effect of intra-atomic interactions on the photoemission delay [18].

A complementary technique to photoemission spectroscopy is attosecond transient absorption spectroscopy (ATAS). While photoemission experiments probe mainly the top most layers of the material, absorption spectroscopy is a bulk-sensitive technique. During the last six years, pioneering ATAS measurements were successfully performed in a wide range of materials to gain a fundamental understanding on how fast the electronic properties of a solid system can be modulated by an intense few-fs laser pulse [19–22]. To date, the fastest conventional transistors reach a maximum operation frequency in the GHz ($1 \text{ GHz} = 10^9 \text{ Hz}$) to the low THz regime ($1 \text{ THz} = 10^{12} \text{ Hz}$) [23, 24]. Since the duration of one field-cycle of a visible IR pulse is on the order of a few femtosecond, switching the electronic state of a solid system by an optical laser field has the potential to boost the operation rate into the petahertz regime ($1 \text{ PHz} = 10^{15} \text{ Hz}$).

The first solid state ATAS experiment has been performed in 2013 by Schultze *et al.* in silicon dioxide, a dielectric with a 9-eV bandgap [19]. Electron dynamics were induced in the strongly non-resonant pump regime by intense IR pulses (1.5 eV central energy). The authors observed a fully reversible modification of the polarizability following the intensity of the pump field. Shortly afterwards, first studies were performed in semiconductors, still with a non-resonant excitation. Schultze *et al.* studied in real-time the carrier injection from the valence band (VB) into the conduction band (CB) in pure silicon ($E_{gap}^{direct} = 3.2 \text{ eV}$) in the tunneling regime. In contrast, Mashiko *et al.* conducted a study in gallium nitride ($E_{gap} = 3.35 \text{ eV}$) in the three-pump-photon absorption regime [21]. The latter authors observed driving of the polarization with a periodicity of 860 as, which corresponds to a frequency above 1 PHz. In 2016, Lucchini *et al.* presented the first observation of the attosecond dynamical Franz-Keldysh effect driven by IR pulses in polycrystalline diamond ($E_{gap}^{direct} = 7.4 \text{ eV}$) [22].

All these mentioned ATAS experiments have in common the non-resonant pump condition. The energy of a single IR photon is smaller than the bandgap. **In this thesis, we performed the first attosecond electron dynamics study in resonantly pumped gallium arsenide (GaAs) ($E_{gap} = 1.42$ eV), a technologically relevant III-V semiconductor.** During the light-matter interaction, the IR pump pulse can induce two distinct mechanism, namely intraband motion and interband transitions. The role of the two processes is however still not fully understood and highly discussed, in particular in the field of high-order harmonic generation (HHG) in solids [25–32]. Given the resonant pump condition in GaAs, it was originally expected that the optical response will be dominated by the interband transition, rather than by the intraband motion. In contrast, the presented investigations revealed that the observed oscillations in the XUV absorption are dominated by the field-driven intraband motion. Furthermore, it was found that the intraband process enhances the injection rate of real carriers into the CB, even though it can itself only move carriers within a single band.

In addition, this thesis presents a study of IR-induced dynamics in $\text{Al}_{0.8}\text{Ga}_{0.2}\text{As}$, an indirect III-V semiconductor with a bandgap larger than the energy of a single pump photon. The comparison of the findings from the two investigated semiconductor alloys is highly interesting, since the excitation mechanism is resonant in GaAs and non-resonant in $\text{Al}_{0.8}\text{Ga}_{0.2}\text{As}$.

In the following, the structure of this doctoral thesis is outlined. In **chapter 2**, important aspects of the attosecond metrology are introduced. In particular, the generation of attosecond pulses and the concept of photoelectron and transient absorption spectroscopy are discussed.

Chapter 3 presents an overview about the laser system and the attosecond pump-probe beamline used for the experiments performed throughout this thesis. Further, the fabrication process of free-standing nano-membranes is outlined.

In **chapter 4**, a detailed study of the Gouy phase shift of an annularly truncated IR beam is presented. The performed experiment revealed that the truncated beam experiences a phase shift deviating significantly from

the one of an ideal Gaussian beam, which has to be taken carefully into account in attosecond measurements.

Chapter 5 contains a detailed discussion of the results obtained via ATAS in III-V semiconductors. First, the investigations of the electron dynamics in GaAs are discussed. In particular, the role of the intra- and interband transitions during the light-matter interaction is studied. Second, similar results from a study performed in $\text{Al}_{0.8}\text{Ga}_{0.2}\text{As}$ are presented.

Chapter 6 discusses the implementation of a tunable optical parametric amplifier (OPA) system into the experimental setup. In particular, a new approach to stabilize the pump-probe phase in an attosecond beamline with two separate IR-colors involved is presented. The performed laser upgrade yields new possibilities for investigating the wavelength-dependence of field-driven carrier dynamics.

Finally, **chapter 7** summarizes the results of this doctoral thesis and gives an outlook for potential future transient absorption experiments in condensed matter.

Attosecond Science

This chapter introduces the basic concepts of attosecond metrology. In particular, the generation of an attosecond pulse train and a single attosecond pulse is discussed. Further, several measurement techniques used during the course of this thesis are reviewed in detail, namely the RABBITT technique, the attosecond streak camera and transient absorption spectroscopy.

2.1 High-order Harmonic Generation

The compression of a laser pulse is ultimately limited by the duration of a field cycle, which is for an 800 nm laser approximately 2.7 fs. Hence, a new approach is needed to achieve a pulse duration in the sub-femtosecond range. HHG has proven to be a suitable technique for the generation of attosecond pulses [7]. The shortest pulses measured so far have a duration of 43 as [10].

HHG is an up-conversion process discovered in the eighties [8,9]. An intense laser pulse ($I_{peak} > 10^{13} \text{ W/cm}^2$) is tightly focused on a gas target. The nonlinear field interaction results in the emission of a photon spectrum that consists of odd high-order harmonics (HHs) of the fundamental driving frequency ω_{IR} and reaches the XUV spectral region, as illustrated in figure 2.1. A typical HH spectrum contains a plateau with harmonics of equal intensity. Above the cut-off energy $E_{cut-off}$, the intensity decreases abruptly.

Besides the generation of HHs in a gas target, HHG has also been successfully demonstrated in molecules [33], in a bulk-crystal [26] and in a liquid [34].

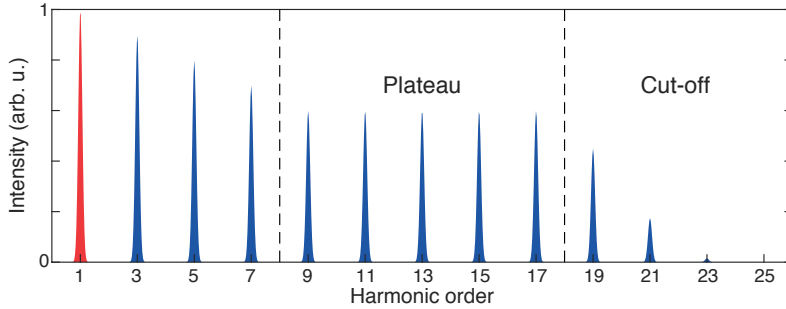


Figure 2.1: Typical HHG spectrum. The fundamental frequency is shown in red, higher harmonics in blue. The intensity of the harmonics is comparable in the plateau region before it drops abruptly above the cut-off energy.

2.1.1 Single Atom Response

The interaction of a strong laser field with an atomic target can be intuitively explained with a simple semiclassical model, known as the simple man model. It divides the HHG process into three steps [35]. In the first step, the atomic potential is bent by the strong laser field, which allows an initially bound electron to tunnel through the barrier into the continuum (figure 2.2(a)). In the second step, the free electron is accelerated by the oscillating electric field first away and then back towards the parent ion, where it finally recombines (figure 2.2(b) and (c)). During the recombination process, a photon is emitted with an energy of $\omega = I_p + E_{kin}$ (in atomic units). I_p is the ionization potential of the atom and E_{kin} describes the kinetic energy of the electron gained during the acceleration in the continuum. The cut-off energy of the emitted HHG radiation is given by the maximum energy an electron gains during the acceleration in the laser field and can be estimated as $\omega_{cut-off} \approx I_p + 3.17 \cdot U_p$ [35]. The ponderomotive energy U_p describes the cycle-averaged quiver energy of a

free electron in an oscillating electric field and is given by

$$U_P = \frac{e^2 E^2}{4m_e \omega^2} = \frac{e^2 E^2}{16\pi^2 m_e c^2} \lambda^2, \quad (2.1)$$

where e and m_e are the electron charge and mass. E and ω are the amplitude and frequency of the laser field. Since U_P scales quadratically with the wavelength λ of the driving laser, the cut-off can be shifted to higher energies by using longer-wavelength photons in the HHG process [36]. This comes at the cost of a reduced HHG flux, which scales as λ^{-5} to λ^{-6} [37].

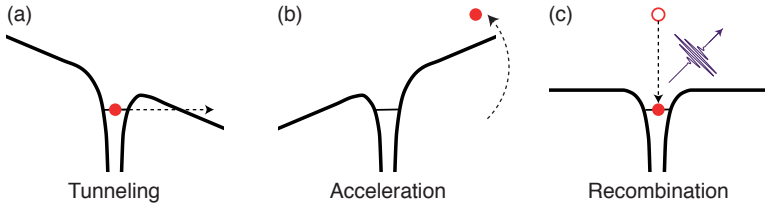


Figure 2.2: HHG process illustrated with a semiclassical three-step model. (a) Bending of atomic potential and tunneling of electron through barrier. (b) Acceleration of free electron in the continuum. (c) Recombination with parent ion and emission of XUV radiation.

2.1.2 Attosecond Pulse Train

With the three-step model, the emission of an attosecond radiation burst has been illustrated. Since this process repeats every half cycle of the laser pulse, the emitted radiation consists of a series of XUV bursts. Each pulse in a so-called attosecond pulse train (APT) has a sub-femtosecond duration and is phase-locked to the driving pulse (figure 2.3). In the energy domain, the pulse train forms a comb-like structure containing the odd HHs of the laser. The individual peaks are separated by twice the driving energy. Their widths depend on the duration of the driving pulse. The shorter it is, the wider the HHs become. With the experimental setup used during this thesis, APTs can be generated with spectra ranging from 20 to 75 eV. The shape and energy position of the generated XUV spectrum can be

tuned by changing the laser parameters (e.g. duration, intensity) as well as the gas target.

2.1.3 Single Attosecond Pulse

An isolated single attosecond pulse (SAP) consists of only one XUV burst (figure 2.3). The corresponding energy spectrum has a continuous shape, in contrast to the comb-like structure of an APT. So far, several approaches have been proposed to generate isolated attosecond pulses, e.g. amplitude gating [38], polarization gating [39], ionization gating [40] and the attosecond lighthouse technique [41].

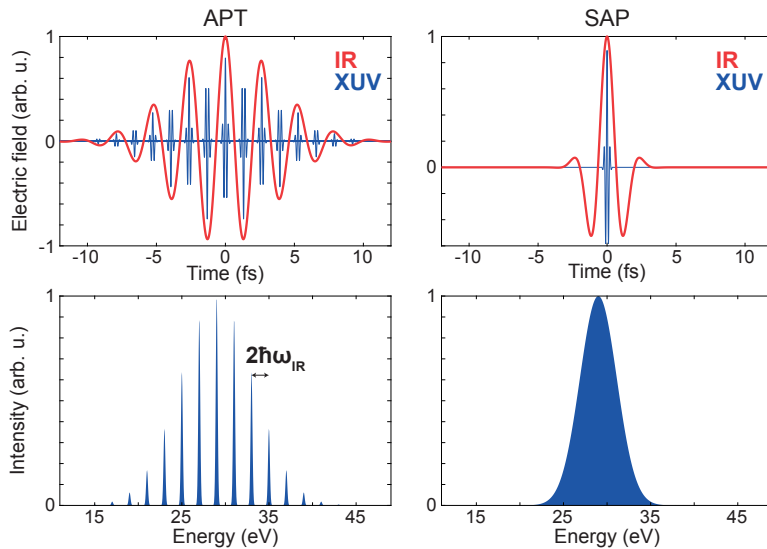


Figure 2.3: Temporal and spectral shape of a typical APT and SAP. The upper panels illustrate an APT (left) and SAP (right) generated by an IR laser pulse in the time domain. The lower panels show the corresponding energy spectra.

During the work of this thesis, the polarization gating (PG) technique was used. This technique makes use of the polarization dependence of the driving field in the HHG process [42]. The HHG efficiency drops significantly for non-linear polarized light. With the simple three-step model,

the polarization dependence can be easily understood. For circular or elliptical light, the recollision probability of the electron wave packet (EWP) with the parent ion is strongly reduced and therefore the emission of an XUV burst suppressed.

In a PG setup, a few-cycle linearly polarized IR pulse propagates through a birefringent quartz crystal followed by a quarter-wave plate (figure 2.4). The quartz plate creates two delayed orthogonally polarized replicas. After this crystal, the overall field is linearly polarized at the leading and trailing tails and elliptically polarized in between. The subsequent propagation through the quarter-wave plate transforms linear to circular polarization and vice versa. Like this, the linear polarization of the total field is restricted to a short time window, ideally corresponding to one half cycle of the driving pulse. Consequently, only one burst of XUV radiation is emitted due to the reduced efficiency of the HHG process for elliptically polarized light.

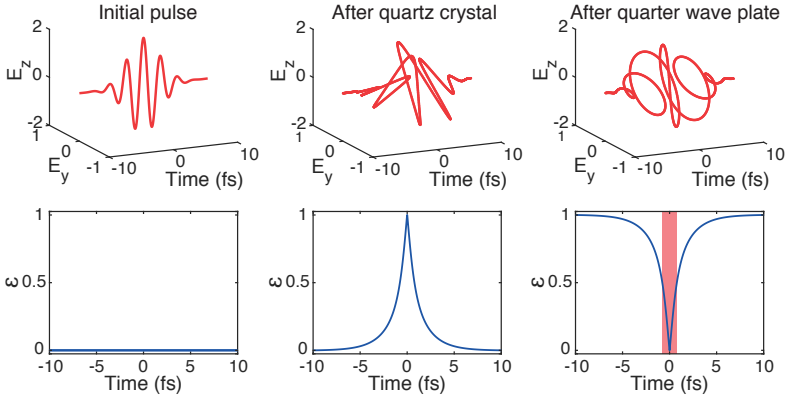


Figure 2.4: Polarization gating technique. (Left) Electric field E (in arb. u.) and ellipticity ε of the initial pulse with linear polarization. (Center) Same after the quartz crystal. (Right) Same after the quarter-wave plate. $\varepsilon = 0$ indicates linear polarization, $\varepsilon = 1$ circular polarization. HHG is only efficient for a close to linear polarization, indicated by the red shaded area in the right lower plot. The full width at half maximum (FWHM) of the initial pulse is 6 fs.

2.2 Attosecond Measurement Techniques

In the course of this work, different types of attosecond pump-probe measurement techniques have been used, namely (1) photoelectron spectroscopy and (2) transient absorption spectroscopy. Both combine an IR pulse with an attosecond XUV pulse. The role of the two contributing pulses depends on the experiment performed. While the XUV radiation acts as the pump mechanism in photoelectron spectroscopy, it probes IR-induced dynamics in transient absorption measurements. The following sections briefly introduce the techniques.

2.2.1 Photoelectron Spectroscopy

There are two different methods of photoelectron spectroscopy: (1) reconstruction of attosecond beating by interference of two-photon transitions (RABBITT) and (2) the attosecond streaking camera. They can be used to characterize the temporal shape of the involved XUV and IR pulses and to extract attosecond time information, such as the photoemission delays from atoms [12], molecules [43] and condensed matter [15,44].

2.2.1.1 RABBITT

In 2001, Paul *et al.* presented a method to characterize the shape of an APT, called RABBITT [7,45]. A RABBITT measurement combines an APT with a few-cycle phase-locked IR pulse. The two beams are focused into a gas jet, where the APT ionizes the atoms. The energy distribution of the emitted photoelectrons mimics the HH spectrum of the APT. For example, HH_{2q-1} generates electrons with energy

$$E_{2q-1}^{\text{electron}} = E_{2q-1}^{\text{XUV}} - I_P = (2q - 1) \cdot \hbar\omega_{\text{IR}} - I_P, \quad (2.2)$$

where E_{2q-1}^{XUV} describes the energy of HH_{2q-1} , I_P the ionization potential of the atom and $\hbar\omega_{\text{IR}}$ the energy of the IR pulse. q is a positive integer. When the XUV and IR pulse overlap in time, two-photon transitions involving one XUV and one IR photon can occur during the ionization process. Additionally to the XUV photon, an IR photon can be absorbed or emitted. This results in an increased or reduced energy of the photoemitted electron by $\hbar\omega_{\text{IR}}$. Thus, each harmonic peak forms an energetically lower and

higher sideband (SB). Since two neighboring harmonics are separated by twice the IR energy, the absorption of HH_{2q-1} plus an additional IR photon contributes to the same SB_{2q} as the absorption of harmonic HH_{2q+1} plus the emission of one IR photon. The interference of the two quantum pathways can be described in the framework of the second-order perturbation theory. The intensity of SB_{2q} oscillates with the pump-probe delay τ as [7,45]

$$\begin{aligned} \text{SB}_{2q}(\tau) &\propto \cos(2\omega_{\text{IR}}\tau - \Phi_{2q}) \\ &= \cos(2\omega_{\text{IR}}\tau + \Theta_{2q-1} - \Theta_{2q+1} - \Delta\varphi_{2q}^{\text{At}} + 2\varphi_{\text{IR}} + \varphi_0), \end{aligned} \quad (2.3)$$

where ω_{IR} is the IR frequency and Φ_{2q} the oscillation phase, which can be divided into four contributions. $\Delta\Theta_{2q} = \Theta_{2q+1} - \Theta_{2q-1}$ describes the phase difference of two neighboring harmonics (attochirp) and $\Delta\varphi_{2q}^{\text{At}}$ the difference of the atomic phase contributions [46–48]. φ_{IR} describes the phase of the IR pulse and φ_0 is an arbitrary phase offset. Figure 2.5 illustrates a typical RABBITT measurement conducted in neon.

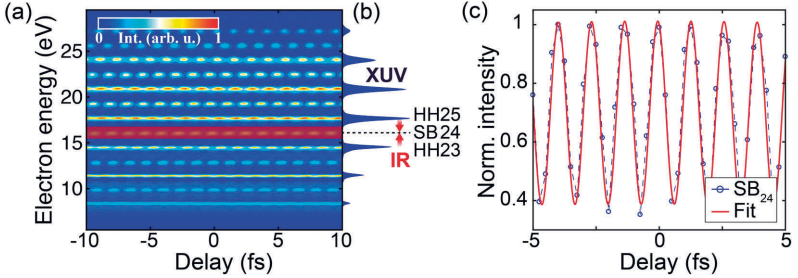


Figure 2.5: Illustration of the RABBITT technique. (a) The color plot shows a typical RABBITT trace measured with an APT in neon. During the pump-probe overlap, SB oscillations occur with an oscillation period of twice the IR frequency. (b) Illustration of the two ionization pathways contributing to the same SB signal. (c) Oscillation of SB_{24} (shaded red area in (a)). The red line is a cosine fit. Adapted from [49].

Commonly, RABBITT measurements are performed to extract the atomic delay, which contains information about the Wigner and continuum-continuum delay [50,51]. Here, in contrast, the RABBITT technique was used to measure and calibrate φ_{IR} . In particular, RABBITT mea-

measurements were performed simultaneously in two spatially separated foci to reconstruct the Gouy phase shift of an annularly truncated IR beam (see section 4, [49]).

2.2.1.2 Attosecond Streak Camera

Electron streaking is based on the interaction of a gas target with a SAP plus an IR pulse. The XUV radiation ionizes the atoms in the gas jet and creates an EWP with an energy distribution resembling the continuous shape of the SAP: $E_{electron} = E_{XUV} - I_p$, where I_p is the ionization potential. During the presence of the IR field, the liberated electrons are either accelerated or decelerated, resulting in a modulation of the final energy of the EWP (figure 2.6(a)). In the following, atomic units are used. The momentum \mathbf{p} of the EWP at time t can be written as

$$\begin{aligned}\mathbf{p}(t) &= \mathbf{A}_{IR}(t) + [\mathbf{p}_0 - \mathbf{A}_{IR}(\tau)] \\ &= \mathbf{A}_{IR}(t) + \mathbf{p}_f,\end{aligned}\tag{2.4}$$

with $\mathbf{A}_{IR}(t)$ being the vector potential of the IR pulse and \mathbf{p}_0 the initial momentum after XUV ionization. τ denotes the XUV-IR delay at the instant of ionization. The first term in equation (2.4) vanishes after the IR pulse has passed. Hence, $\mathbf{p}_f = \mathbf{p}_0 - \mathbf{A}_{IR}(\tau)$ describes the final momentum of the EWP. The pump-probe delay dependent photoelectron spectrum measured with a time-of-flight (TOF) spectrometer can be written within the strong field approximation as [52–54]

$$S(\mathbf{p}_f, \tau) = \left| \int_{-\infty}^{+\infty} dt \mathbf{E}_{XUV}(t - \tau) \mathbf{d}_{\mathbf{p}_f + \mathbf{A}_{IR}(t)} \cdot e^{i\varphi(\mathbf{p}_f, t)} e^{i(\mathbf{p}_f^2/2 + I_p)t} \right|^2, \tag{2.5}$$

$$\varphi(\mathbf{p}_f, t) = - \int_t^{\infty} dt' \left(\mathbf{p}_f \cdot \mathbf{A}_{IR}(t') + \mathbf{A}_{IR}^2(t')/2 \right), \tag{2.6}$$

where $\mathbf{E}_{XUV}(t)$ is the XUV field and $\mathbf{d}_{\mathbf{p}(t)}$ the dipole matrix element of the ground state to continuum transition. In the framework of the central momentum approximation (CMA), \mathbf{p}_0 can be replaced by the central momentum p_c of the unstreaked trace. Further, the dipole matrix element can be assumed to be constant in the streaking region, $\mathbf{d}_{\mathbf{p}(t)} = \mathbf{d}_{p_c}$. For parallel XUV/IR polarization, equation (2.5) simplifies and takes the form of a frequency-resolved optical gating (FROG) spectrogram with a pulse

$P(t)$ and gate $G(t)$ term:

$$\begin{aligned} S(p_f, \tau) &\propto \left| \int_{-\infty}^{+\infty} dt E_{XUV}(t - \tau) \cdot e^{i\varphi(p_f, t)} e^{i(p_f^2/2 + I_p)t} \right|^2 \\ &= \left| \int_{-\infty}^{+\infty} dt P(t - \tau) \cdot G(t) \cdot e^{i\omega t} \right|^2, \end{aligned} \quad (2.7)$$

with $P(t) = E_{XUV}(t)$, $G(t) = e^{i\varphi(p_f, t)}$ and $\omega = p_f^2/2 + I_p$. Hence, the pulse term is equal to the temporal shape of the XUV pulse and the gate function is a pure phase term. Various iterative algorithms have been developed to reconstruct both the pulse and gate term, known as frequency-resolved optical gating for complete reconstruction of attosecond bursts (FROG-CRAB) [55–57]. Here, the extended ptychographic iterative engine (ePIE) has been used to retrieve the temporal shape of the XUV and IR pulse [58]. Figure 2.6 illustrates a typical measured and reconstructed streaking trace.

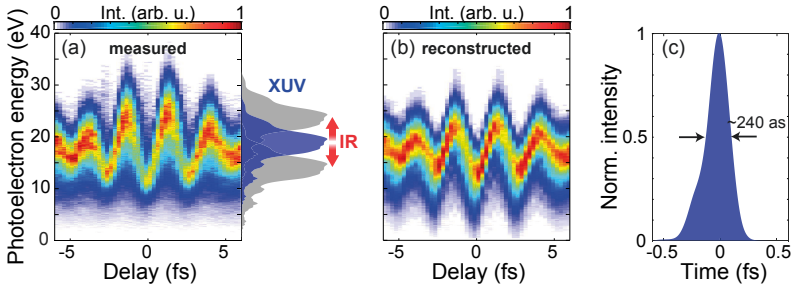


Figure 2.6: Attosecond streaking spectroscopy. (a) Measured photoelectron streaking trace. The SAP ionizes a gas target, here neon. The IR pulse accelerates or decelerates the EWP, depending on the pump-probe delay. (b) Reconstructed streaking trace with the ePIE algorithm [58]. (c) Reconstructed envelope of the SAP.

2.3 Absorption Spectroscopy

Transient absorption spectroscopy has proven to be a powerful tool to study few- to sub-femtosecond electron dynamics in solids [19–22, 59, 60]. In the absorption measurements presented in this thesis, the charge carrier dynamics are induced by intense few-cycle IR pulses and probed by delayed attosecond XUV pulses. As illustrated in figure 2.7(a), a fraction of the attosecond radiation propagates through the solid membrane and is recorded with an XUV spectrometer. The energy-dependent absorbance $Abs(E)$ of the XUV pulse is defined as

$$I_{trans}(E) = I_{in}(E)e^{-\alpha(E) \cdot L} = I_{in}(E)e^{-Abs(E)}, \quad (2.8)$$

$$Abs(E) = \ln\left(\frac{I_{in}(E)}{I_{trans}(E)}\right), \quad (2.9)$$

where $I_{in}(E)$ and $I_{trans}(E)$ are the initial and transmitted XUV spectra and $\alpha(E)$ describes the absorption per length.

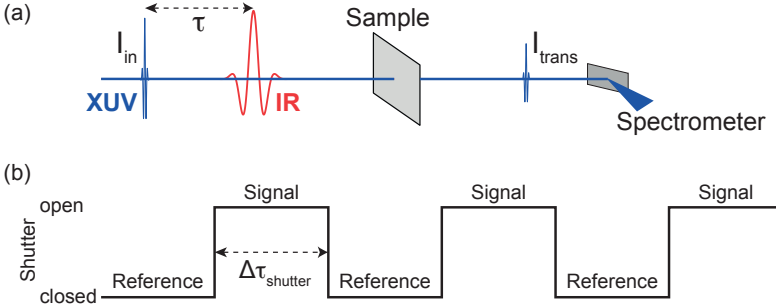


Figure 2.7: Attosecond transient absorption spectroscopy. (a) Illustration of pump-probe scheme. An XUV spectrometer records the transmitted attosecond radiation. (b) To eliminate slowly varying noise contributions, signal and reference spectra are recorded in fast sequence with and without the IR pump present. To enable this, a fast mechanical shutter is placed in the IR beam path.

An example of an ATAS measurement in GaAs is shown in figure 2.8 (see section 5 for details). The left panel compares the transmitted XUV spectra with and without the IR pump present. For certain energy regions, the absorption in the solid is increased or decreased by up to a few percent.

For a better illustration, usually the IR-induced change in absorbance is shown instead of the transmitted spectra itself (figure 2.8(b)). Red (blue) regions indicate increased (reduced) absorbance. $\Delta Abs(E)$ is defined as

$$\begin{aligned}\Delta Abs(E, \tau) &= Abs_{IR}(E, \tau) - Abs_0(E) \\ &= \ln\left(\frac{I_{in}(E)}{I_{trans}^{sig}(E, \tau)}\right) - \ln\left(\frac{I_{in}(E)}{I_{trans}^{ref}(E)}\right) \\ &= \ln\left(\frac{I_{trans}^{ref}(E)}{I_{trans}^{sig}(E, \tau)}\right),\end{aligned}\quad (2.10)$$

where $Abs_{IR}(E, \tau)$ and $Abs_0(E)$ describe the absorbance with and without the IR pulse present. $I_{in}(E)$ is the initial XUV spectrum. $I_{trans}^{sig}(E, \tau)$ and $I_{trans}^{ref}(E)$ are the transmitted spectra with (signal) and without (reference) the pump pulse. τ denotes the pump-probe delay. A fast mechanical shutter with an operating frequency of up to 150 Hz was used to measure signal and reference spectra in fast sequence (figure 2.7(b)). Like this, slowly varying noise could be eliminated and absorption changes of less than 1% could be resolved. Ideally, shot-to-shot referencing would be desirable. However, the readout time of the XUV spectrometer is significantly longer than the repetition rate of the laser system. Therefore, each signal and reference spectrum consists always of several XUV pulses.

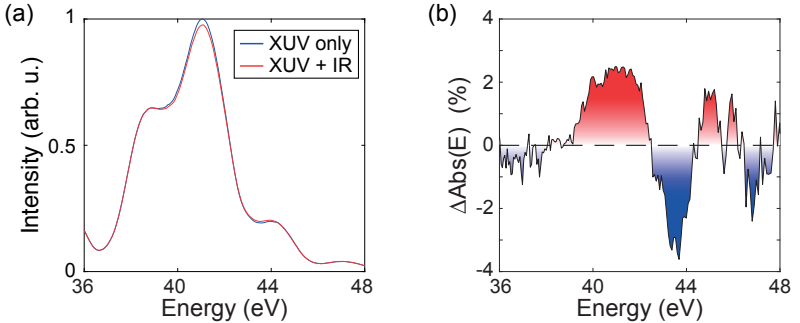


Figure 2.8: Absorption in GaAs. (a) Recorded XUV spectra after propagation through a 100-nm-thick GaAs membrane with (red) and without (blue) the IR pump pulse present. (b) Change of XUV absorbance (see equation (2.10) for definition of $\Delta Abs(E)$). Increased absorbance is highlighted in red, decreased in blue.

2.3.1 Membrane Thickness Limitation

There are two crucial points to consider when choosing the thickness of a solid sample for an ATAS measurement. First, XUV radiation is strongly absorbed in most materials. Second, the propagation velocity of the XUV and IR pulses can differ significantly in the membrane.

Figure 2.9 illustrates the XUV transmission of a GaAs membrane in the energy range from 20 to 50 eV for different sample thicknesses. Since the absorption increases exponentially with the thickness (see equation (2.8)), already 500 nm results in an almost negligible transmission. Therefore, ultra-thin samples are essential for ATAS measurements.

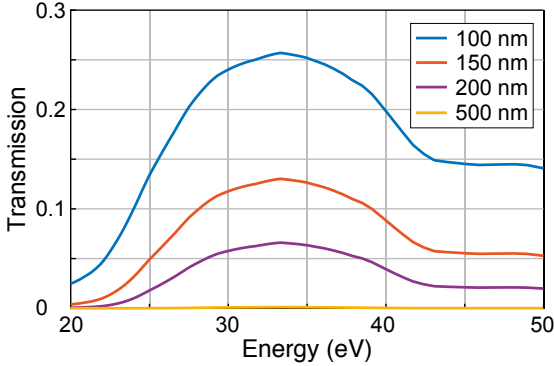


Figure 2.9: Thickness-dependent XUV transmission of a GaAs membrane. Data extracted from [61,62].

The second point becomes important if absorption oscillations are induced by the pump field on a sub-cycle timescale, as in GaAs (see section 5). The phase velocity of the IR field in the membrane is $v_{IR} = \frac{c}{n_{IR}}$. For the XUV pulse, we assume that the group velocity in the material does not deviate strongly from the speed of light in vacuum [63]. Thus, the propagation times of the IR field and the XUV pulse through a membrane with thickness d differ by

$$\Delta\tau \approx \frac{d}{c} \cdot n_{IR} - \frac{d}{c} = \frac{d}{c} \cdot (n_{IR} - 1). \quad (2.11)$$

Consequently, the measured absorption signal for an initial pump-probe delay τ is actually an average over pump-probe delays between $\tau - \Delta\tau$ and τ (see appendix B.2.2 for further details). Here, one assumes that the penetration depth d_{pen} of the IR beam is larger than the sample thickness, which is the case for the investigated 100-nm-thick GaAs membranes ($d_{pen} \approx 700$ nm for $\lambda = 780$ nm [64]).

Thus, to resolve absorption modifications oscillating at twice the IR-pump frequency, the membrane must be thinner than

$$d_{max} = \frac{\lambda_{IR}}{2 \cdot (n_{IR} - 1)}, \quad (2.12)$$

where λ_{IR} is the IR wavelength. For thicker samples, the oscillations are averaged out, since $\Delta\tau$ becomes larger than half the oscillation period of the laser field.

For GaAs, the critical membrane thickness is $d_{max} \approx 144$ nm, since $n_{780nm} \approx 3.7$ [64].

Experimental Setup

The experiments presented within this thesis have been performed at the *attoline*, a versatile attosecond pump-probe beamline with a two foci configuration. The aim of this chapter is to introduce the experimental setup. In section 3.1, the laser systems used are reviewed. In section 3.2, the individual components of the attoline are discussed. Finally, section 3.3 focuses on the fabrication process of the nano-membranes, which have been used in the experiments discussed in chapter 5.

3.1 Laser System

3.1.1 Ti-Sapphire Laser

Figure 3.1 illustrates the main laser system (Femtolasers: Femtopower Pro V CEP). It consists of three stages: An oscillator followed by two chirped pulse amplifiers (CPAs).

In the first stage, a Ti-sapphire oscillator (Femtolasers: Rainbow) is pumped with a continuous wave (cw) diode-pumped solid state laser (DPSSL) with an output power of 3 W and 532 nm wavelength (Coherent: Verdi V5). The pump laser propagates first through an acousto-optic modulator (AOM) before being focused into the oscillator crystal. By slightly moving one end-mirror of the oscillator cavity, Kerr-lens mode-locked operation can be initiated. The oscillator provides 7 fs pulses with 2.6 nJ pulse energy at a repetition rate of 77 MHz. A fast feedback loop measures

3. EXPERIMENTAL SETUP

and locks the carrier-envelope frequency to a quarter of the repetition rate by modulating the pump power with help of the AOM. This translates to a stabilized carrier-envelope phase (CEP) after the Pockels cell in the pre-amplifier.

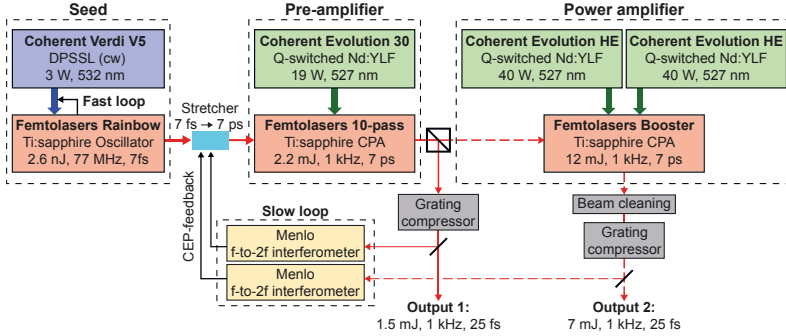


Figure 3.1: Overview of the laser system. The laser system consists of three stages: a Ti-sapphire oscillator and two CPAs.

The oscillator output is stretched to 7 ps and then amplified in a 10-pass CPA. The pre-amplifier is pumped with a 19 W Q-switched Nd:YLF laser. After the first four passes through the Ti-sapphire crystal, the beam propagates through a Pockels cell followed by an acousto-optic programmable dispersive filter (AOPDF) (Fastlite: DAZZLER). The Pockels cell acts as a pulse picker to reduce the repetition rate from 77 MHz to 1 kHz and the AOPDF acts as a pulse shaper. The pre-amplifier provides a pulse train with a repetition rate of 1 kHz, pulse energy of up to 2.2 mJ and pulse duration of 7 ps. The output can be either further amplified in a high-power CPA or employed directly for experiments. In the latter case, the pulses are compressed with a grating compressor to approximately 25 fs (output 1 in figure 3.1).

In the power amplifier, the seed passes twice through a Ti-sapphire crystal pumped with two Q-switched Nd:YLF lasers, each delivering 40 W power. The output pulses have a time duration of 7 ps, pulse energy of up to 12 mJ and a repetition rate of 1 kHz. This beam is later used to pump an OPA, which requires a good beam profile. Due to its consid-

erable intensity, the output beam of the power amplifier forms a hotspot after some meters of propagation in air. This can be prevented by filtering out undesirable noise contributions by focusing the beam onto a pinhole. The image of the beam in the focal plane is its two-dimensional Fourier transform. The undesired noise frequencies appear away from the center and can be filtered out. In the present setup, the beam is focused in vacuum onto a 3 mm long piece of a glass fiber with an inner hole diameter of 420 μm . The focusing mirror used has a radius of curvature of 4 m, which results in a $1/e^2$ beam width of $\sim 275 \mu\text{m}$ in the focus. The length and diameter of the pinhole have been chosen experimentally as a compromise between beam quality and propagated power. The alignment of the pinhole has proven to have a strong effect on the quality and power of the final beam and thus the pinhole is mounted on a 5-axis stage and the beam pointing is actively stabilized onto the filter. The beam cleaning prevents the formation of hotspots even after several meters of propagation. Finally, a grating compressor followed by chirped mirrors reduces the pulse duration to about 25 fs. The pulse energy after the filter and compressor is up to 7 mJ (output 2 in figure 3.1).

To compensate for slow CEP drifts acquired in the amplifier stages, a second stabilization loop is required. A small fraction of the amplifier output is coupled into a f -to- $2f$ interferometer, which enables to extract the CEP. A closed feedback loop adjusts the amount of glass in the stretcher to compensate for the detected CEP drifts. Like this, the CEP can be stabilized to a root mean square (rms) value below 0.15.

3.1.2 Optical Parametric Amplifier

For some experiments, it is desirable to have photons with a longer wavelength than the one provided by the Ti-sapphire laser systems. In the case of GaAs, for example, tuning the wavelength from 800 nm to 1500 nm enables studying the transition from resonant to non-resonant pump excitation.

During the scope of this thesis, a commercial OPA from Coherent (HE-TOPAS) has been installed. As illustrated in figure 3.2, the cleaned and compressed output of the power amplifier is divided with an 85/15 beam

splitter into two separate paths. The larger part is used to pump the HE-TOPAS. The wavelength of the generated signal and idler can be tuned from 1160 to 1600 nm and 1600 to 2600 nm, respectively. Their polarizations are s (signal) and p (idler). In the current configuration, only the signal is used. With a periscope, the polarization of the signal is flipped to p . At a set signal wavelength of 1500 nm, the TOPAS delivers pulses with an energy of up to 0.65 mJ and approximately 40 fs time duration.

The weaker fraction passing through the beam splitter is recombined with the TOPAS beam using a dichroic mirror. Finally, the two overlapping beams are sent collinear to the experimental setup in the neighboring laboratory.

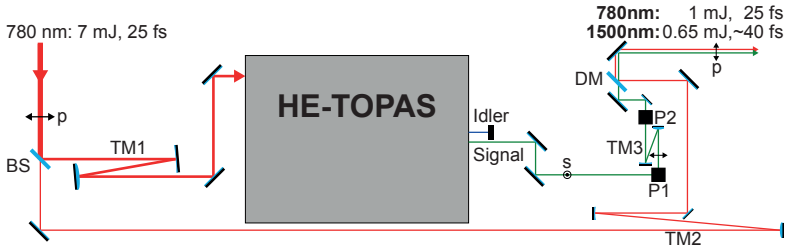


Figure 3.2: Optical parametric amplifier. The output of the Ti-sapphire power amplifier is divided in two parts. 85% are used to pump the HE-TOPAS. The generated signal is recombined with the 15% transmitted through the beam splitter (BS) with help of a dichroic mirror (DM). TM = telescope mirrors, PM = periscope mirrors.

3.1.3 Pulse Compression

The generation of a SAP requires few-cycle laser pulses. In the present setup, optical filamentation has been used to further compress the Ti-sapphire output from 25 fs to 5-6 fs [65,66]. Another widely used approach is hollow-core fiber compression [67].

The principle of filamentation is based on two counteracting nonlinear processes. The intense laser beam is loosely focused into a tube filled with a noble gas. The Kerr-lens effect leads to self-focusing of the beam due to an intensity depending refractive index ($n(I) = n + n_2 \cdot I$). Self-focusing

ultimately results in the ionization of the gas atoms and in the formation of gas plasma. The created plasma then acts as a defocusing lens and prevents a collapse of the beam. Thus, the two effects balance each other and create a stable filament. During the propagation through the gas cell, the intense beam experiences spectral broadening via self-phase modulation (SPM). The spectrally broadened pulses are finally compressed in time with chirped mirrors.

In our setup, the IR beam propagates through two sequential gas cells filled with argon and with a length of 2 and 1.7 m, respectively. Typically, the pressure in the cells is set between 400-800 mbar. For the generation of the SAP used in section 5, the tubes have been filled with 400 and 720 mbar of argon, respectively. After each gas cell, two chirped mirrors are placed. A pair of fused silica wedges is further installed to fine-tune the pulse dispersion. Like this, pulses with a duration of 5 to 6 fs and a center wavelength around 780 nm have been generated.

3.2 Attoline

The attoline is a pump-probe beamline enabling to perform simultaneous measurements in two spatially separated interaction chambers. An overview of the setup is shown in figure 3.3 and a detailed description can be found in reference [68]. The attoline can be divided into four sections: (1) the front-end chambers, (2) and (3) the first and second experimental interaction chambers and (4) the XUV spectrometer. In the following, the different parts are described.

The output of the Ti-sapphire laser and OPA are sent in evacuated tubes from the laser laboratory to the attoline. Before entering the front-end chambers, the beams are coupled out from the vacuum system for further pulse compression. Currently, only the Ti-sapphire pulses are compressed. Figure 3.4 illustrates the two possible laser operation configurations. In the first one (figure 3.4(a)), the output of the 10-pass pre-amplifier is used. In the second one (figure 3.4(b)), the signal of the OPA system (green line) plus a fraction of the 800-nm radiation of the power amplifier (red line) are sent collinear to the attoline (see figure 3.2). After compression of the Ti-sapphire beam, the two colors are guided back into the beam-

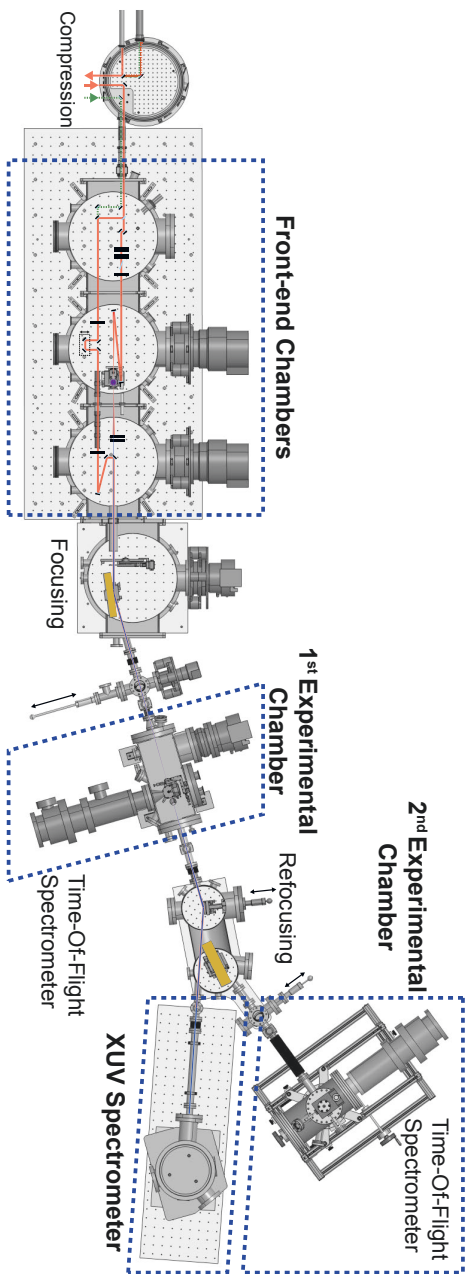


Figure 3.3: Attoline overview.

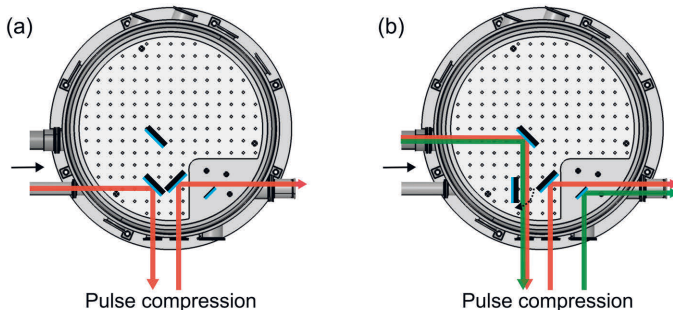


Figure 3.4: Illustration of different laser configurations. (a) The output of the Ti-sapphire pre-amplifier is used for the experiment. (b) The output of the power-amplifier is used to pump the OPA. The OPA signal (green) is sent collinear with a fraction of the Ti-sapphire beam (red) to the attoline. After compression of the Ti-sapphire beam, the two colors are sent back to the vacuum system on different paths.

line on different paths. Apart from section 6, the first laser configuration was used for the experiments discussed in this thesis.

The beam paths in the three front-end chambers of the beamline are illustrated in detail in figure 3.5. In the first chamber, the 800 nm beam is divided with an 80/20 beam splitter on two beam paths. The larger part (80%) propagates through a PG setup followed by an iris and is then focused into a gas cell for HHG. The gas cell is located in the second chamber. Depending on the orientation of the birefringent crystals in the PG setup, either an APT or a SAP can be generated (see section 2.1.3). The motorized iris is used to adjust the beam intensity. An aluminum (Al) filter with a transmission window from 15 to 73 eV, placed in the third chamber, blocks the residual IR used for HHG. Further, the positive attochirp of the XUV radiation can be compensated by the negative group delay dispersion (GDD) of the Al foil [69, 70]. In addition to the Al foil, an additional filter can be inserted into the beam path on a second filter wheel to limit the XUV spectrum to specific HHs (see for example [71]). Finally, the filtered XUV radiation is recombined with the 20% fraction of the beam reflected on the beam splitter. Due to the lack of transmissive optics in the XUV range, a drilled mirror is used for the recombination.

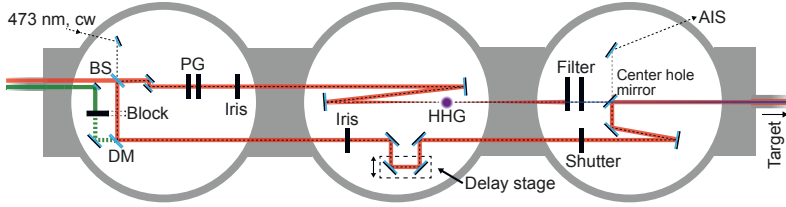


Figure 3.5: Overview of the front-end chambers. The 800 nm beam is shown in red, the OPA beam in green. Depending on the experiment, either the 800 nm or OPA beam propagates on the delay arm and is recombined with help of the center-hole mirror with the generated XUV radiation. The beam path of the cw laser used for the active interferometric stabilization (AIS) is shown in black dashed.

The XUV beam propagates through the hole, while the IR is reflected on the outer part of the mirror. This results in an annularly truncated IR beam profile, extensively discussed in section 4. On the second beam path, a motorized delay stage is installed to control the pump-probe delay. Further, a motorized iris is placed also in this arm to adjust the IR power.

In case the OPA beam is used, the 800 nm beam on the delay arm can be blocked and the OPA beam, shown in green, can propagate on this path instead. Currently, the OPA beam can only be used on the delay arm but not for HHG.

Figure 3.5 includes in addition the beam path of a cw 473 nm laser (black dashed), which is used to actively stabilize the interferometer spanning from the beam splitter to the recombination mirror, similar to reference [72].

After the front-end chambers, the pump and probe beams are focused into the first interaction region using a toroidal mirror. As shown in figure 3.6, the interaction region is equipped with a TOF spectrometer (Kaesdorf ETF11). A gas nozzle and solid target can be inserted at the same time into the focus. The spacing between the two targets is approximately 1.35 mm. This setup configuration enables measuring simultaneously streaking spectroscopy in the gas target and ATAS in the solid membrane (see section 5). Halfway between the toroidal mirror and the first interaction chamber, a mirror can be inserted to couple out the IR pulses for beam

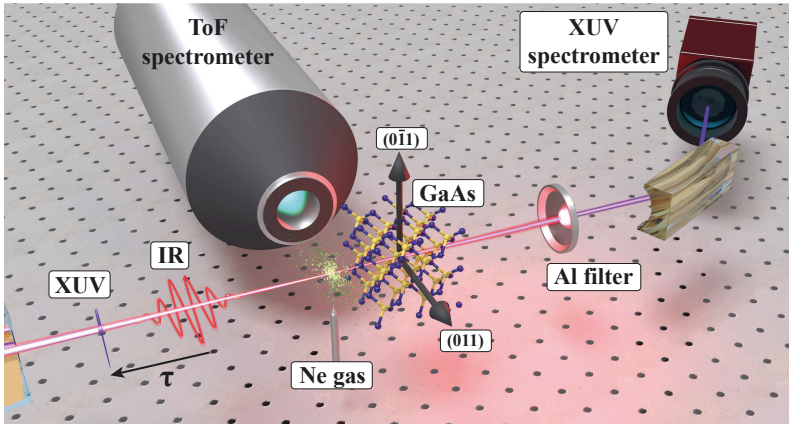


Figure 3.6: First experimental chamber and XUV spectrometer. A gas and solid target can be inserted simultaneously into the first focus, enabling simultaneous streaking and ATAS measurements. Adapted from [59].

diagnostics and to set the temporal and spatial pump-probe overlap.

After the first interaction chamber, a spherical mirror mounted on a moveable stage refocuses the XUV radiation on the $100\ \mu\text{m}$ entrance slit of the XUV spectrometer (grating: 450 grooves/mm). The spectrum is recorded with a charge-coupled device (CCD) camera (Princeton Instruments PIXIS-XO 400B).

By moving out the spherical mirror from the beam path, a second toroidal mirror creates a 1:1 image of the first focus in a second experimental chamber. This chamber is again equipped with a gas target and a TOF spectrometer. An important feature is that the TOF spectrometer can be moved together with the gas target along the beam propagation direction. This made it possible to precisely characterize the Gouy phase shift of the IR beam (see section 4, [49]). Figure 3.7 shows the IR beam profiles measured in the first and second focus. Obviously, the beam shapes deviate significantly from an ideal Gaussian. This is the result of the reflection on the center-hole mirror used for the XUV/IR recombination.

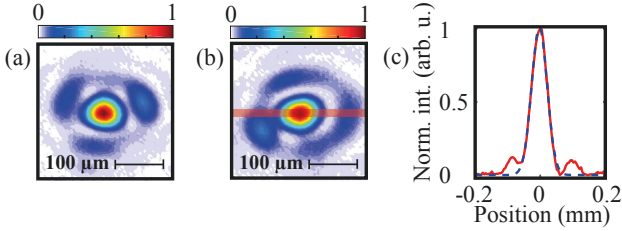


Figure 3.7: IR beam profile. Measured beam profile of the truncated IR beam in (a) the first and (b) second focus. The red curve in panel (c) shows a cut of the second focus (red bar in (b)). There is a clear deviation to an ideal Gaussian (blue dashed line). Adapted from [49].

3.3 Nano-Membrane Fabrication

In section 2.3, the measurement concept of transient absorption spectroscopy has been introduced. As discussed, the sample thickness needs to be below a critical value to resolve field-induced carrier dynamics. For GaAs the critical thickness is about 145 nm. This section will illustrate in detail the fabrication process of a GaAs nano-membrane. Similar membranes were fabricated in [73,74].

A semiconductor heterostructure is grown by molecular beam epitaxy (MBE) on a GaAs wafer (figure 3.8(a)). The heterostructure consists of a 300-nm-thick $\text{Al}_{0.8}\text{Ga}_{0.2}\text{As}$ etch stop layer and a 100-nm GaAs top layer. To place the samples later into the experimental setup, the wafer is cleaved into pieces of 5x8 mm. The sample axes point along the (011) and (0 $\bar{1}$ 1) directions. The surface of the GaAs layer is the (100) plane. In the next step, the thickness of the GaAs wafer is reduced from 620 μm to 200 μm with mechanical polishing (figure 3.8(b)). Then, both sides of the sample are coated with a negative photoresist (Ma-N 1440, figure 3.8(c)) and exposed to ultraviolet (UV) light for 80 seconds. A mask placed on the wafer side protects a small area of 0.5 mm diameter from the UV radiation (figure 3.8(d)). Areas exposed to UV light are hardened and remain after 2 minutes of development in Ma-D 533 (figure 3.8(e)). In the next step, the sample is placed into a citric acid/ H_2O_2 solution (4:1) for 7-9 hours (figure 3.8(f)). Due to the high etch rate selectivity between GaAs and

$\text{Al}_{0.8}\text{Ga}_{0.2}\text{As}$, etching stops at the etch stop layer [75]. After removing the residual photoresist with acetone (figure 3.8(g)), the etch stop layer is finally etched away with hydrogen fluoride (HF, figure 3.8(h)). The remaining free-standing GaAs membrane has a thickness of 100 nm and a lateral dimension of about 300 to 500 μm , which is significantly larger than the beam diameters of the IR and XUV in the focus of the first interaction chamber.

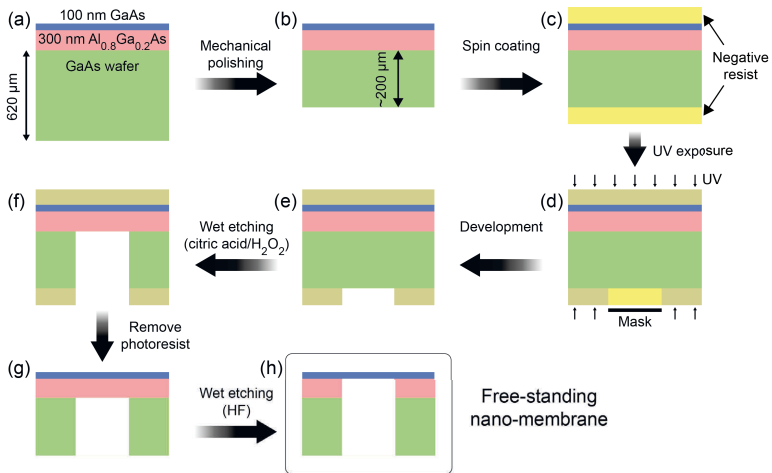


Figure 3.8: Nano-membrane fabrication. Illustration of the fabrication process of a free-standing 100-nm-thick GaAs membrane.

Gouy Phase Shift

Photoelectron spectroscopy is a widely used technique to study attosecond photoemission delays in atoms, molecules and solids, as discussed in section 2. The time information is usually extracted from the phase of an oscillating signal. In the case of the RABBITT technique, the occurring SB oscillations are analyzed (see section 2.2.1). Equation (2.4) showed however that the SB signal does not only depend on the atomic phase but also on the phase of the XUV and IR beams. Hence, a precise phase calibration of the involved laser pulses across the interaction region can be crucial for accurate attosecond delay measurements.

In an attosecond pump-probe beamline, the XUV radiation is often recombined with the IR pulse with help of a center-hole mirror. The XUV propagates through the hole, while the IR is reflected. Using this type of recombination is required due to the lack of suitable transmissive optics for the XUV radiation. This results however in an annular beam profile for the IR pulse, deviating strongly from an ideal Gaussian profile.

An ideal Gaussian beam experiences a π -shift across the focus, the so-called Gouy phase shift [76]. Previous theoretical and experimental studies have demonstrated that an annularly truncated beam can have a Gouy phase shift significantly larger than π [77–79]. This chapter presents a detailed calibration of the Gouy phase of an annular IR beam using the double RABBITT technique. Further, the impact of the phase shift on attosecond measurements is discussed.

Details about the publication printed in this chapter are listed below. The text and figures are as in the publication. Only the style of the text, figures and equations has been adapted to the style of the thesis. Further, the numbering of the figures and references has been adjusted. The reference list of the publication has been included in the reference list of the thesis.

Title: "Gouy phase shift for annular beam profiles in attosecond experiments", [49]

Journal: *Optics Express*

doi: 10.1364/OE.25.003646

URL: <https://doi.org/10.1364/OE.25.003646>

Published: 10th February 2017

©2017 Optical Society of America. One print or electronic copy may be made for personal use only. Systematic reproduction and distribution, duplication of any material in this paper for a fee or for commercial purposes, or modifications of the content of this paper are prohibited.

4.1 Gouy Phase Shift for Annular Beam Profiles in Attosecond Experiments

F. Schlaepfer^{1,2,}, A. Ludwig^{1,2}, M. Lucchini¹, L. Kasmi¹, M. Volkov¹,
L. Gallmann¹ and U. Keller¹*

¹ Department of Physics, ETH Zurich, 8093 Zurich, Switzerland

² These authors contributed equally to this work.

* *f.schlaepfer@phys.ethz.ch*

Attosecond pump-probe measurements are typically performed by combining attosecond pulses with more intense femtosecond, phase-locked infrared (IR) pulses because of the low average photon flux of attosecond light sources based on high-harmonic generation (HHG). Furthermore, the strong absorption of materials at the extreme ultraviolet (XUV) wavelengths of the attosecond pulses typically prevents the use of transmissive optics. As a result, pump and probe beams are typically recombined geometrically with a center-hole mirror that reflects the larger IR beam and transmits the smaller XUV, which leads to an annular beam profile of the IR. This modification of the IR beam can affect the pump-probe measurements because the propagation that follows the reflection on the center-hole mirror can strongly deviate from that of an ideal Gaussian beam. Here we present a detailed experimental study of the Gouy phase of an annular IR beam across the focus using a two-foci attosecond beamline and the RABBITT (reconstruction of attosecond beating by interference of two-photon transitions) technique. Our measurements show a Gouy phase shift of the truncated beam as large as 2π and a corresponding rate of 50 as/mm time delay change across the focus in a RABBITT measurement. These results are essential for attosecond pump-probe experiments that compare measurements of spatially separated targets.

4.1.1 Introduction

To date most attosecond pump-probe measurements combine extreme-ultraviolet (XUV) attosecond pulses with a few-femtosecond phase-locked

infrared (IR) pulse [1, 80]. Fundamental fast processes such as photoemission can be resolved for the first time [12, 15, 43, 46, 81–84]. The most common techniques to unravel the attosecond dynamics are either based on attosecond streaking [38, 53] or on RABBITT (Reconstruction of Attosecond Beating By Interference of Two-photon Transitions) [7, 45]. However both measurement techniques only give access to relative time delays and have different trade-offs [47]. Relative photoemission time delays have been measured between two different initial states of the same target [12, 81, 85] or between different gas targets [83], for which better accuracy is obtained with coincidence measurements [46].

Alternatively, one can use a second spatially separated target to recalibrate the measurement and obtain absolute photoemission delays [44, 86]. This approach makes it possible to study a wider range of ultrafast dynamics in gas, molecular and solid targets [19, 20, 22]. Depending on the kind of physical system under investigation, the target under test is either placed consecutively in close proximity to the reference target within the same focus [19, 20, 22] or spatially separated in a second focus using re-focusing optics after a first focus for the reference target [Fig. 4.1] [68]. Such attosecond measurements would greatly benefit from more precise and more accurate temporal calibration below 10 attoseconds. This makes it essential to better understand the wavefront properties of the pump and probe beams along the spatially separated targets.

As a beam experiences a phase shift across the focus (Gouy phase shift) [76], the phase contribution introduced through the relative position of the targets within the focus becomes essential in phase-sensitive measurements. This phase shift directly impacts the measured time delay because phase and delay are linked via an energy derivative. One approach is to simply avoid the Gouy phase by placing the target sufficiently far away from the focus [7]. This also minimizes any possible averaging effect induced by a rapidly varying Gouy phase across the extended interaction volume probed in the experiment. For an ideal Gaussian beam, 50% of the total Gouy phase shift occurs within one Rayleigh range, with much slower phase evolution outside. However, in attosecond pump-probe experiments that combine the IR and the attosecond pulses geometrically, the IR beam can strongly deviate from a theoretical Gaussian shape. Such

geometric beam combining is typically used because no suitable beamsplitters or dichroic optics are available for the XUV spectral region. A very common geometrical beam recombination scheme is to use a mirror with a center hole, for which the smaller XUV beam is transmitted through the center, while the larger IR beam is reflected on the outer mirror part. This produces an annular IR beam profile with a considerably different Gouy phase compared to an ideal Gaussian beam [77].

Previously it has been predicted by Chang [77] and measured by Lindner et al. [78] and Shivaram et al. [79] that the Gouy phase shift of a truncated few-cycle IR beam can be significantly larger than the π -shift of a Gaussian beam. Here, we used the RABBITT technique in a setup with two spatially separated foci to perform a detailed study of the Gouy phase shift of an annular IR beam produced by the reflection on a center-hole mirror. Our results show a Gouy phase shift of more than 2π and a corresponding rate of 50 as/mm time delay change across the focus in a RABBITT measurement. The result does not depend on the probing harmonic energy and shows that a precise calibration with a proper control of the target positions is mandatory in attosecond photoemission delay measurements with spatially separated targets. Our work demonstrates the feasibility of more precise attosecond pump-probe experiments, which can access absolute photoemission delays if combined with a proper choice of reference system.

4.1.2 Setup

A detailed description of the setup used in the experiment can be found in reference [68]. We used IR laser pulses with energy of up to 430 μJ , 25-fs time duration, a center wavelength of 790 nm and a pulse repetition rate of 1 kHz [Fig. 4.1]. A beamsplitter divides the IR beam into two parts. The strongest part (80%) of the IR beam is focused into a gas cell filled with argon for high-order harmonic generation (HHG). The emitted XUV spectrum consists of odd harmonics of the IR beam covering the energy range between 25 and 55 eV (harmonics 17 to 33). A 100-nm thick aluminum filter blocks the residual IR beam after HHG. The weaker part (20%) of the initial IR beam follows a delay path before being recombined with the XUV light on a center-hole mirror. The XUV beam propagates through

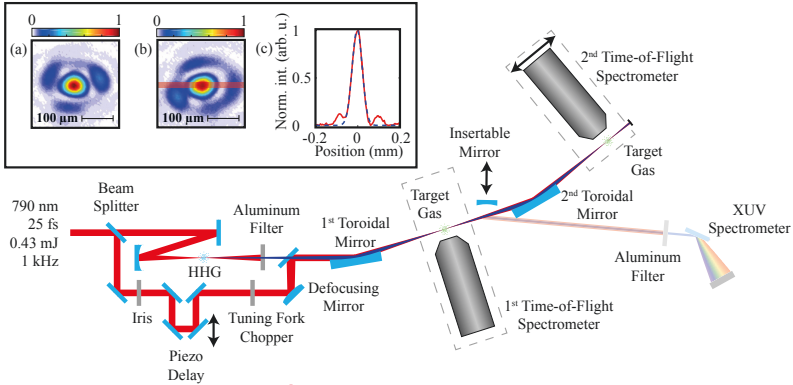


Figure 4.1: Schematic of the two-target attosecond beamline with high-order harmonic generation (HHG), the attosecond/femtosecond interferometer and the two-foci geometry [68]. A defocusing mirror in the delay path matches the wavefronts of the IR and XUV on the center-hole mirror. The second gas target and time-of-flight (ToF) spectrometer can be moved together along the beam propagation direction. The insets (a) and (b) show the measured IR beam profile in the first (a) and second (b) focus. Inset (c) shows a cut of the second focus illustrated red in (b). The red curve is the beam profile and the blue dashed line a Gaussian fit.

the hole while the mirror reflects the IR beam. The combined collinearly propagating beams after the center-hole mirror are then focused with a toroidal mirror into the first reference target interaction chamber with a neon gas target and a time-of-flight spectrometer (ToF). After this first target, a toroidal mirror makes a 1:1 image of the first focus into a second interaction chamber, which has also a neon gas target and a second ToF to fully characterize the absolute temporal accuracy of the setup. The insets (a) and (b) in Fig. 4.1 show the beam profiles of the IR beam measured in the two foci. Inset (c) illustrates a cut through the second focus. It is clearly visible that the profile (red line) deviates strongly from a Gaussian fit (blue dashed line). The beam radius of the Gaussian fit is $47.9 \mu\text{m}$, which would correspond to a Rayleigh length of 9.1 mm. The second gas target together with its ToF spectrometer can be moved along the beam propagation direction, which allows for RABBITT measurements over a propagation distance of 40 mm around the focus. The exact position of the IR beam focus in the second chamber has been determined by recording strong-field ion-

ization yields from ethylene, a molecule with low ionization potential. If the few-femtosecond IR pulse is intense enough, the molecule is ionized via above-threshold-ionization (ATI). As shown in Fig. 4.2, the integrated ATI yield strongly depends on the z -position of the target. We determined the focus position of the IR beam at the maximum total electron yield. As we will see later, this point is in full agreement with the position where the Gouy phase goes through zero.

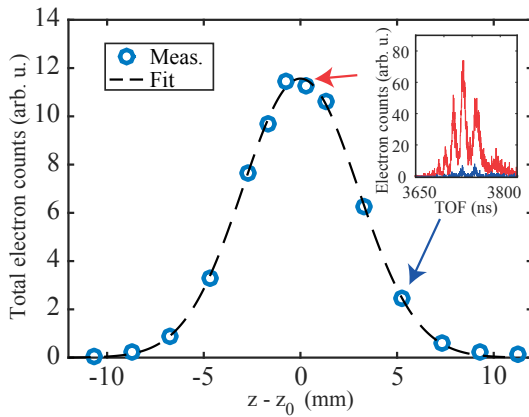


Figure 4.2: Total measured electron counts of ATI spectra from ethylene as a function of the second chamber position (blue open dots) and the Gaussian fit (black dashed curve) used to extract the focal position. The inset shows two spectra for two positions of the second time-of-flight (ToF) spectrometer nozzle assembly, $z = 0.25$ mm (red arrow) and $z = 5.25$ mm (blue arrow).

4.1.3 Phase Measurement

An example of two RABBITT traces recorded simultaneously in the two target regions is shown in Fig. 4.3. During the temporal overlap of the XUV pump and IR probe beam, oscillating sidebands appear in the photoelectron spectrum between the peaks, which originate from direct ionization via absorption of a harmonic photon. Each of these sidebands (SBs) is the result of the interference between two distinct two-photon, two-color ionization pathways. The sideband of order $2q$ originates either from the

absorption of a photon from the harmonic $2q-1$ and an additional IR photon, or from the absorption of a photon from the harmonic $2q+1$ and the emission of one IR photon [7, 45]. In the framework of the second-order perturbation theory, the SB oscillation can be described as follows:

$$SB_{2q}(\tau) \propto \cos(2\omega_{IR}\tau - \Phi_{2q}) = \cos(2\omega_{IR}\tau - \Delta\Theta_{2q} - \Delta\varphi_{2q}^{At} + 2\varphi_{IR} + \varphi_0), \quad (4.1)$$

where ω_{IR} is the IR frequency, τ is the pump-probe delay. Φ_{2q} is the total SB phase and corresponds to the phase directly measurable in the experiment. This total phase can be further decomposed into different terms: $\Delta\Theta_{2q} = \Theta_{2q+1} - \Theta_{2q-1}$ is the phase difference between consecutive harmonics (attochirp), $\Delta\varphi_{2q}^{At}$ is the difference of the atomic phase contributions [46–48], φ_{IR} is the phase of the IR beam and φ_0 the arbitrary choice of the zero phase.

Usually the term of physical interest is the atomic term, since it is related to the photoionization process in the target under test. However here in our experiment we want to investigate how φ_{IR} changes along the focus. By using the same gas target in the two foci we assure that the atomic contribution is identical in the two interaction regions, $\Delta\varphi_{2q}^{At,(1)} = \Delta\varphi_{2q}^{At,(2)} = \Delta\varphi_{2q}^{Ne}$. We will show later that the effect of the re-focusing mirror and the interaction in the first target on the phase of the XUV beam in the second target is negligible. Hence also the term $\Delta\Theta_{2q}$ does not change between the two targets. The Gouy phase shift of the XUV beam can also be neglected due to its shorter wavelength (longer Rayleigh range).

It then follows that by changing the position of the second target along the IR beam focus we change mainly φ_{IR} due to the Gouy phase shift of the IR, $\varphi_{Gouy}^{IR}(z)$. By looking at the phase difference between two simultaneously acquired RABBITT traces we thus estimate the Gouy phase of the IR pulse (up to a constant offset):

$$\Delta\Phi_{2q}(z) = \Phi_{2q}^{(1)} - \Phi_{2q}^{(2)}(z) = 2\varphi_{Gouy}^{IR}(z) + \tilde{\varphi}_0, \quad (4.2)$$

where $\Phi_{2q}^{(1)}$ and $\Phi_{2q}^{(2)}(z)$ represent the phase extracted from the oscillation of the SB with order $2q$ in the first and second ToF spectrum, respectively, and $\tilde{\varphi}_0$ is a constant phase offset due to the choice of target position in the first chamber.

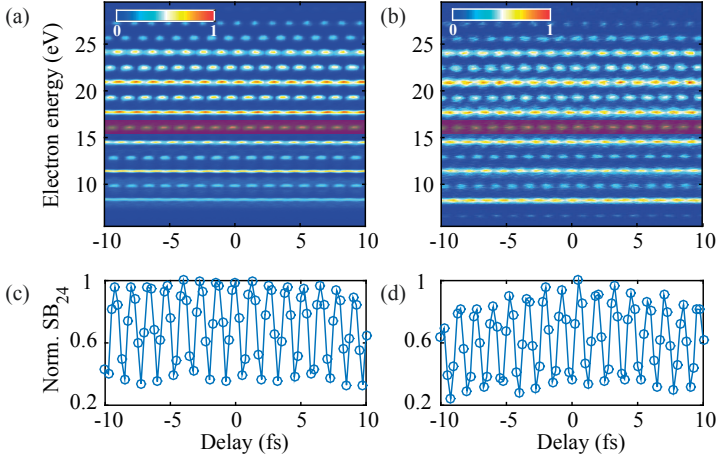


Figure 4.3: (a), (b) Simultaneously measured RABBITT traces in the first and second Ne-target regions. Oscillating SBs with order 20 (9.82 eV) to 30 (25.52 eV) are clearly visible in both traces. (c), (d) Normalized electron yield of SB 24 obtained by integrating over the energy region highlighted in red in (a) and (b).

To extract $\Phi_{2q}(z)$ from the experimental traces we looked at the product between the Fourier transform of a particular SB signal in the first chamber [Fig. 4.3(c)], $\widetilde{SB}_{2q}^{(1)}(\omega)$, and the complex conjugate of the same quantity extracted from the second ToF spectrum, $\widetilde{SB}_{2q}^{(2)*}(\omega, z)$ (Fig. 4.3(d); for further details see supplementary material of [16]):

$$C_{2q}(\omega, z) = \widetilde{SB}_{2q}^{(1)}(\omega) \cdot \widetilde{SB}_{2q}^{(2)*}(\omega, z). \quad (4.3)$$

$|C_{2q}(\omega, z)|$ has a peak at the common oscillation frequency $\omega_0^{2q} \cong 2\omega_{IR}$ of the two traces and a corresponding phase that is equal to the phase difference between the two sideband signals, $\Delta\Phi_{2q}(z)$. We first calculated the average value of ω_0^{2q} over all the SB orders and found it to be $\omega_0^{avg} = 4.77 \pm 0.06$ PHz. Then we used Eq. (4.3) to evaluate $\Delta\Phi_{2q}(z)$ for each individual SB order at the frequency ω_0^{avg} in order to ensure that the extracted phase difference always corresponds to the same oscillation period. The Gouy phase $\varphi_{Gouy}^{IR}(z)$ corresponds to half of the extracted $\Delta\Phi_{2q}(z)$ apart from the arbitrary constant $\tilde{\varphi}_0$ [Eq. (4.2)].

In a first step, we investigated in detail the dependence of the phase difference $\Delta\Phi_{2q}(z)$ on the SB order $2q$. The main phase term that is expected to change between different SBs is the attochirp of the XUV, $\Delta\Theta_{2q}$. Figure 4.4(a) shows the individual phases Φ_{2q} from the RABBITT oscillations extracted in the first (red circles) and in the second focus (blue circles, $z = -2.7$ mm) for each SB. The attochirp results in a significant change of the individual phases of more than 0.7π between SB 18 and 32. Nevertheless, one would expect the effect of the attochirp $\Delta\Theta_{2q}$ to cancel out completely in $\Delta\Phi_{2q}(z)$ [Eqs. (4.1) and (4.2)]. This is true if no significant distortion is induced in the harmonics by the refocusing toroidal mirror and if the variation of the Gouy phase of the XUV light with the harmonic order is negligible. To quantify this statement more precisely, we plot the relative phase difference $\Delta\Phi_{2q}(z)$ as a function of the SB order for several measurement points along the focus [Fig. 4.4(b)]. By comparing Fig. 4.4(a) with Fig. 4.4(b) we can show that taking the difference between the two target phases removes efficiently the attochirp. Therefore, we can conclude that the refocusing toroidal mirror in our two-foci setup does not introduce any energy-dependent delay on the harmonics. As a consequence, it is justified to assume an energy-independent propagation delay between the two spatially separated target regions. Furthermore, we can conclude that the attochirp is removed by taking the phase difference between the two spatially separated targets, independent from the exact position of the second target. The fact that we did not observe any energy dependence of the phase difference $\Delta\Phi_{2q}(z)$ also supports our assumption that the Gouy phase of each harmonic does not significantly affect the phase difference $\Delta\Phi_{2q}(z)$ and thus any spatial dependence of this quantity can be ascribed solely to the IR Gouy phase.

Figure 4.5(a) shows the extracted Gouy phase $\varphi_{Gouy}^{IR}(z)$ of the IR beam obtained with the method described above from eight different SB oscillations (orders 18-32). For all SBs, the phase experiences a change of almost 2π within a spatial range of -40 mm to 30 mm around the focus [Fig. 4.2], which exceeds by far the π -shift of an ideal Gaussian beam. The phase shifts extracted from different SBs are virtually indistinguishable. This confirms that there is no appreciable dependence on the XUV wavelength as already indicated by our data shown in Fig. 4.4. Thus, we can average

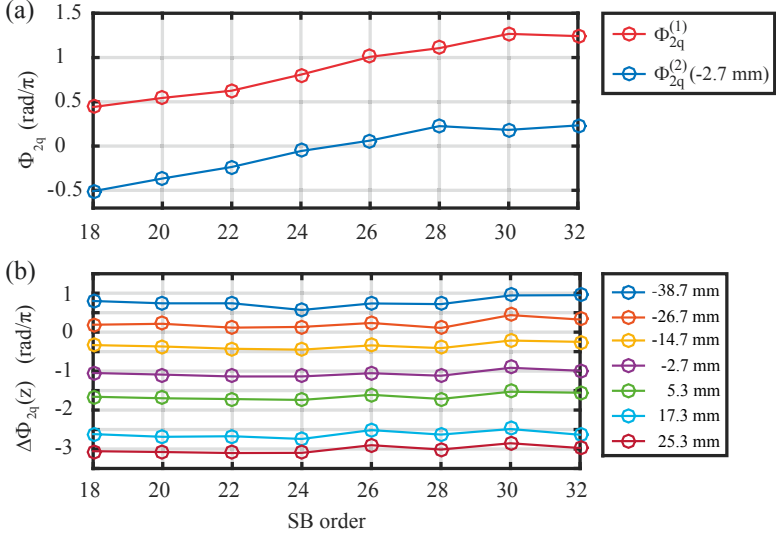


Figure 4.4: (a) Energy dependence of the oscillation phase measured in the first and second target region (red = 1st, blue = 2nd). The phase has been extracted from eight SBs. Here, the position of the second target is $z = -2.7$ mm. The phase increases clearly in both foci with increasing SB energy as a result of the XUV attochirp. (b) Energy dependence of the relative phase difference, $\Delta\Phi_{2q} = \Phi_{2q}^{(1)} - \Phi_{2q}^{(2)}(z)$, for seven positions of the second target.

the phase behavior from different SBs for a better estimate of $\varphi_{Gouy}^{IR}(z)$. Figure 4.5(b) displays $\varphi_{Gouy}^{IR}(z)$ obtained by averaging over the SB orders for two independent measurements taken under identical experimental conditions on different days. The error bars represent the standard deviation within each data set. The two curves overlap perfectly, which confirms the reproducibility of the measurements.

The Gouy phase shift of an ideal Gaussian beam is described by $\varphi = -\tan^{-1}(z/z_R)$, with z_R denoting the Rayleigh length. According to Refs [77, 87], the Gouy phase of an annular beam follows the arctan shape as well, but with an additional pre-factor $A \neq 1$, thus $\varphi = -A \cdot \tan^{-1}(z/z_R)$. If we use this expression to fit our data, we find $A = 2.45 \pm 0.37$ and $z_R = 32.7 \pm 6.8$ mm [Fig. 4.5(b)]. We can conclude as follows:

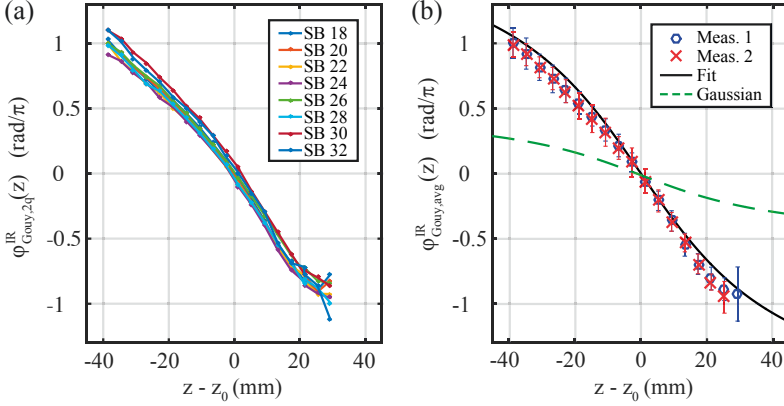


Figure 4.5: (a) Phase difference between simultaneously measured RABBITT traces obtained for eight different sidebands while varying the position of the second interaction chamber. (b) Phase difference averaged over the SB orders for two independent measurement sets. The error bars represent the corresponding standard deviation. The black line is the result of a fit with the function $\varphi = -A \cdot \tan^{-1}(z/z_R)$ giving $A = 2.45 \pm 0.37$ and $z_R = 32.7 \pm 6.8$ mm. The green dashed line illustrates the Gouy phase of a Gaussian beam with the same Rayleigh length z_R .

1. The Rayleigh length z_R is substantially larger than the one extracted from an ideal Gaussian fit of the IR beam profile ($z_R = 9.1$ mm). As shown in the setup description [Fig. 4.1] our IR beam reflected from a center-hole mirror deviates strongly from a Gaussian beam profile. Furthermore our IR beam experiences some astigmatism. As we demonstrated, the variation of the Gouy phase along the beam propagation direction z is still considerable even a few centimeters away from the focus.
2. The large pre-factor A shows clearly that the Gouy phase shift of a beam reflected on a center-hole mirror strongly deviates from the one of a beam with a Gaussian profile and cannot be simply neglected [Fig. 4.5(b)].

4.1.4 Equivalent Photoionization Delays

In attosecond pump-probe spectroscopy the spectral phase of an electron wave packet (EWP) contains time information about the system under test. In the photoemission process for example, the EWP experiences a phase offset depending on the initial state. The energy derivative of the phase corresponds to a group delay and therefore a relative phase offset between EWPs emitted from different initial states reveals directly the relative photoemission delay between them [12] as long as the continuum does not contain any resonances [46]. As the SB phase of a RABBITT measurement corresponds to a sum of phase differences [Eq. (4.1)], it is possible to directly obtain the photoemission delay associated with the two-color, two-photon ionization process [50] in the framework of the finite difference approximation as follows:

$$\tau_{2q} = \frac{\partial \Phi_{2q}}{\partial \omega} \cong \frac{\Phi_{2q}}{2\omega_{IR}} = \tau_{2q,chirp} + \tau_{2q,atom} - \tau_{IR} - \tau_0. \quad (4.4)$$

$\tau_{2q,chirp}$ is the group delay of the XUV (attochirp), $\tau_{2q,atom}$ is the atomic delay consisting of the Wigner delay and the continuum-continuum delay [50,51], τ_{IR} is the delay resulting from the IR phase and the constant τ_0 results from the arbitrary choice of delay zero. From Eq. (4.4) it becomes evident that the measurement-induced delays due to the XUV and the IR beams need to be known, calibrated or removed by measuring with respect to a reference to obtain the target specific delay $\tau_{2q,atom}$ from the measured quantity τ_{2q} .

As discussed in the introduction one possible approach is based on the relative delay between two spatially separated targets. If the measurement-induced changes are the same in both targets, the contribution of the XUV and IR beams cancels out in the delay difference:

$$\Delta \tau_{2q,atom}^{(1)-(2)} = \tau_{2q}^{(1)} - \tau_{2q}^{(2)} = \tau_{2q,atom}^{(1)} - \tau_{2q,atom}^{(2)}. \quad (4.5)$$

However, as our investigation has demonstrated, the IR phase changes significantly with the target position along the propagation direction across the focus [Fig. 4.5]. Based on Eq. (4.4) this dependence will transfer into a time delay according to $\tau_{IR}(z) = \frac{2 \cdot \varphi_{IR}(z)}{2\omega_{IR}}$. This means that any de-

lay comparison of spatially separated targets can potentially introduce an error in $\Delta\tau_{2q,atom}^{(1)-(2)}$ due to uncertainties in the target positions.

In order to evaluate this effect, we calculated the relative delay between our two targets as a function of the position of the second one. Following the earlier analysis [Fig. 4.4], we can neglect the contribution of the attochirp to the delay difference. Since we used identical gas targets, the relative delay in our case is equal to:

$$\Delta\tau_{2q}^{(1)-(2)}(z) = \tau_{2q}^{(1)} - \tau_{2q}^{(2)}(z) = \frac{2\varphi_{Gouy}^{IR}(z) + \tilde{\varphi}_0}{2\omega_{IR}} = \frac{2\varphi_{Gouy}^{IR}(z)}{2\omega_{IR}} + \tilde{\tau}_0, \quad (4.6)$$

with $\tilde{\tau}_0$ denoting the remaining constant delay offset. This offset does not depend on the target position and thus will not be considered in the following discussion. Figure 4.6(a) shows the delay calculated from Eq. (4.6) that corresponds to the extracted $\varphi_{Gouy}^{IR}(z)$ (blue circles) and a fit with the function $\tau = -B \cdot \tan^{-1}(z/z_R)$, with $B = 1.56 \pm 0.29$ and $z_R = 31.3 \pm 8.2$ mm (red curve). The modulus of the spatial derivative of the fit changes as $\frac{B \cdot z_R}{z_R^2 + z^2}$ and amounts to a maximum of 50 as/mm at the focus [Fig. 4.6(b)]. This shows clearly that the spatial dependence of the phase along the target interaction region results in a non-negligible contribution to the measured phase and group delay in a RABBITT (or streaking) experiment. Any calibration with spatially separated targets is thus affected by the Gouy phase, which needs to be taken carefully into account. This is particularly important for the case of small differences in photoemission delays, which are of the order of magnitude of a few tens to a few hundreds of attoseconds. Note in case of attosecond streaking, which is not an interferometric technique, the Gouy-phase-induced delay will be half the one measured in the RABBITT.

4.1.5 Conclusion

In conclusion, we performed a detailed study of the Gouy phase of an annular IR beam, using our two-foci measurement setup in combination with the RABBITT technique. Our results show that the corresponding Gouy phase experiences a shift of more than 2π across the focus, which exceeds by far the π -shift expected for an ideal Gaussian. The Gouy phase

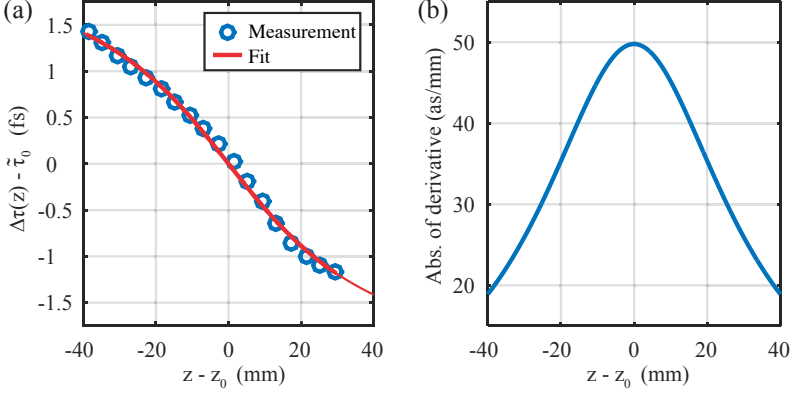


Figure 4.6: (a) Relative delay $\Delta\tau_{2q}^{(1)-(2)}(z) = \tau_{2q}^{(1)} - \tau_{2q}^{(2)}(z)$ between simultaneously measured RABBITT traces as a function of the target position in the second target chamber. A constant delay offset $\tilde{\tau}_0$ has been subtracted to obtain a zero delay at the focus. The blue circles are measurement points. The red curve is the result of a fit with the function $\tau = B \cdot \tan^{-1}(z/z_R)$. (b) Absolute value of the first derivative of the delays in (a) with respect to propagation distance across the focus showing a maximum of 50 as/mm at the focus.

contribution still varies significantly even a few centimeters away from the focus. This has two main consequences: (i) in contrast to ideal Gaussian beams, it is not possible to find a spatial region away from the focus where the Gouy phase variation is negligible. Any individual measurement will be affected by the changing IR phase for a detector integrating over the interaction volume. (ii) A spatially dependent IR phase translates into an additional phase or time delay between two spatially separated targets. As in the case of our double foci setup, this applies also to measurements of spatially separated targets within a single focus. We showed that the effect of the Gouy phase can correspond to additional 50 as/mm time delays around the focus in a RABBITT experiment for our typical beam geometry using a center-hole mirror to collinearly recombine the IR and XUV beams in attosecond pump-probe measurements. If not properly taken into account, this can prevent a reliable calibration and thus the extraction of physical meaningful attosecond delays in photoemission. Our results show that a precise positioning of the target in the focus is essen-

tial for highly accurate time delay measurements. A proper calibration of the Gouy phase of the IR field across the focus together with a suitable choice of the reference target will support better calibration for absolute time delays in attosecond pump-probe measurements using IR and XUV pulses.

Funding NCCR MUST, funded by the Swiss National Science Foundation (SNSF).

Attosecond Transient Absorption Spectroscopy

In this chapter, ultrafast electron dynamics in III-V semiconductors are investigated with transient absorption spectroscopy. This class of semiconductors is widely used in electronic devices. Thus, a fundamental understanding of the carrier processes in these materials on the ultrafast timescale is of great interest for future applications. As discussed in the motivation, switching of the electronic properties of a solid with an optical light field lays the path for high-speed electro-optical devices operating in the PHz regime [88].

This chapter is structured as follows: Sections 5.1 to 5.3 introduce the applied measurement technique, the band structure properties of the investigated semiconductors and the relation between the experimental observable and the simulated quantity. Section 5.4 contains an extensive study of attosecond electron dynamics in GaAs, which have has published in Nature Physics [59]. In section 5.5, a similar investigation performed in $\text{Al}_{0.8}\text{Ga}_{0.2}\text{As}$ is discussed. The comparison of dynamics observed in GaAs and $\text{Al}_{0.8}\text{Ga}_{0.2}\text{As}$ is in particular interesting since the IR excitation is resonant in the first material and non-resonant in the second.

Details about the publication printed in section 5.4 are listed below. The corresponding Supplementary Information is attached in appendix B of this thesis. The text is as in the publication. The figures are as in the post-print version. Only the style of the text, figures and equations has been adapted to the style of the thesis. Further, the numbering of the figures and references has been adjusted. The reference list of the publication has been included in the reference list of the thesis.

Title: "Attosecond optical-field-enhanced carrier injection into the GaAs conduction band", [59]
Journal: *Nature Physics*
doi: 10.1038/s41567-018-0069-0
URL: <https://doi.org/10.1038/s41567-018-0069-0>
Published: 12th March 2018
©2018, Springer Nature.

5.1 Core Level Spectroscopy

Transient absorption spectroscopy has proven to be a powerful technique to study ultrafast dynamics in metals [60], semiconductors [20,21,59,89,90] and dielectrics [19,22] on the attosecond timescale. In most of these experiments, the induced dynamics are probed via a core level to continuum transition. In semiconductors, for example, the IR-pump pulse redistributes the electron population around the bandgap and the XUV probes the new distribution via the excitation of a core electron to the valence and conduction bands. Thus, an essential requirement for this type of spectroscopy is that the material has a core level with a binding energy that overlaps with the energy spectrum of the XUV radiation. Throughout this thesis, the binding energy refers to the energy gap from the core level to the top of the VB.

Table 5.1 summarizes the binding energies of the least bound core levels of elements from the III, IV and V group. With the attosecond beamline used here, XUV photons within the energy window from 20 to 75 eV can be generated. Only the core levels of aluminum (Al-2*p*), germanium (Ge-3*d*), arsenide (As-3*d*), tin (Sn-4*d*) and antimony (Sb-4*d*) are in this energy range. The semiconductor alloy to be examined must therefore contain at least one of these elements.

III	IV	V
B	C	N
1s: 190.53 eV [91]	1s: 284 eV [92]	1s: 397.73 eV [91]
Al	Si	P
2p: 73.7 eV [93]	2p: 98.52 eV [20]	2p: 132.5 eV [94]
Ga	Ge	As
3d: 18.81 eV [95]	3d: 29.55 eV [95]	3d: 40.73 eV [95]
In	Sn	Sb
4d: 17.43 eV [96]	4d: 24.43 eV [97]	4d: 31.92 eV [98]

Table 5.1: Overview of core level binding energies. The least bound core level of elements from the III, IV and V group are listed. The core level splitting is not taken into account in this overview. Further details about the splitting can be found in the corresponding references.

5.2 Band Properties of GaAs and $\text{Al}_{0.8}\text{Ga}_{0.2}\text{As}$

The focus of this thesis was on the III-V semiconductors GaAs and $\text{Al}_{0.8}\text{Ga}_{0.2}\text{As}$. In these alloys, the As-3*d* core level with a binding energy around 40.7 eV is suitable to probe the IR-induced carrier dynamics.

Figure 5.1(a) illustrates the band structure of GaAs around the bandgap. The maximum of the VB, as well as the minimum of the CB, can be found at the Γ -point. GaAs has thus a so-called direct bandgap (~ 1.42 eV at room temperature [99]). The bandgap of $\text{Al}_x\text{Ga}_{1-x}\text{As}$ depends strongly on the aluminum concentration x . It can be either direct or indirect, as is shown in figure 5.1(b). For an Al concentration below 0.43, the VB maximum and CB minimum are both at the Γ symmetry point. For larger x values, the smallest gap becomes indirect with the VB top at the Γ -point and CB bottom at the X-point. The direct ($\Gamma \rightarrow \Gamma$) and indirect ($\Gamma \rightarrow X$) bandgaps of $\text{Al}_{0.8}\text{Ga}_{0.2}\text{As}$ are ~ 2.57 eV and ~ 2.09 eV, respectively [99].

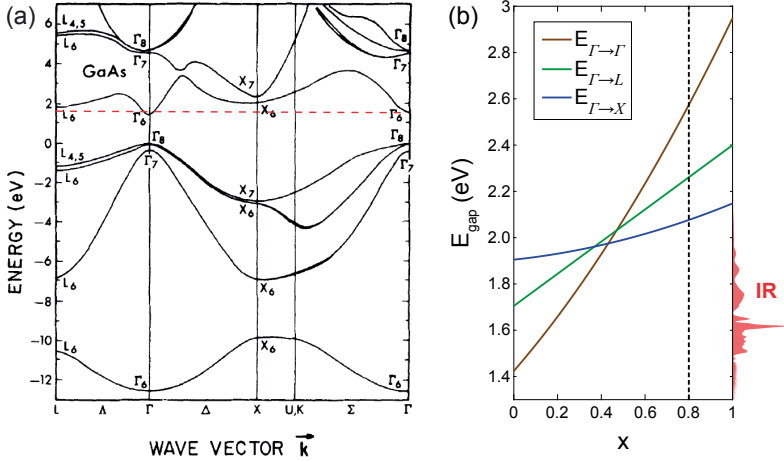


Figure 5.1: Band structure and bandgap. (a) Band structure of GaAs. The red line marks the energy of an 800-nm IR pulse with respect to the VB top ($E_{IR} \approx 1.6$ eV). Extracted from [100]. (b) Energy gap between the VB maximum (located at the Γ -point) and the CB at different symmetry points [99]. x denotes the aluminum concentration in $\text{Al}_x\text{Ga}_{1-x}\text{As}$. The vertical dashed line marks the concentration of the $\text{Al}_{0.8}\text{Ga}_{0.2}\text{As}$ sample studied in section 5.5. In addition, a typical IR-spectrum used in the following experiments is plotted.

5.3 Relation between Absorbance and Dielectric Function

This section explains briefly the relation between the change of the absorbance, ΔAbs , and the change of the dielectric function, $\Delta \epsilon$. The full derivation is given in appendix A. This connection will be important in the following section when the experimental observable ΔAbs is compared to the simulated $\Delta \epsilon$.

In a first step, the pump-probe experiment is simulated by considering a unit cell and solving the time-dependent Kohn-Sham equation with included IR pump and XUV probe fields (see for details appendix B.2.1, [101]). From this calculation, the transient probe current $J_{probe}(t)$ induced by the probe field $E_{probe}(t)$ can be extracted. The energy-dependent conductivity $\sigma(\omega)$ and dielectric function $\epsilon(\omega)$ can then be obtained as follows:

$$\sigma(\omega) = \frac{J_{probe}(\omega)}{E_{probe}(\omega)}, \quad (5.1)$$

$$\epsilon(\omega) = 1 + i \frac{2\pi}{\omega} \sigma(\omega), \quad (5.2)$$

where $J_{probe}(\omega)$ and $E_{probe}(\omega)$ are the Fourier transformations of $J_{probe}(t)$ and $E_{probe}(t)$.

Next, the propagation of the linearly polarized light field through the solid with a thickness L is calculated. We assume normal incidence and that the field consists of a single frequency ω . Solving Maxwell's equations yields the following stationary solution:

$$E_z(x, t) = \begin{cases} e^{i(k_0 x - \omega t)} + r \cdot e^{i(-k_0 x - \omega t)} & x < 0 \\ \alpha \cdot e^{i(\tilde{k} x - \omega t)} + \beta \cdot e^{i(-\tilde{k} x - \omega t)} & 0 \leq x \leq L \\ \gamma \cdot e^{i(k_0(x-L) - \omega t)} & x > L \end{cases}, \quad (5.3)$$

where $k_0 = \omega/c$ and $\tilde{k} = k_0 \sqrt{\epsilon(\omega)}$ are the wave numbers in vacuum and the solid. With these equations of the electric field and the continuity conditions at the solid-vacuum interfaces, the transmission $T(\omega) = |\gamma|^2$ can be calculated. The full derivation is given in appendix A:

$$T(\omega) = |\gamma|^2 = \left| \frac{2k_0 \tilde{k}}{2k_0 \tilde{k} \cdot \cos(\tilde{k}L) - i(k_0^2 + \tilde{k}^2) \cdot \sin(\tilde{k}L)} \right|^2. \quad (5.4)$$

Since the wave number \tilde{k} depends on the frequency ω , also the transmission T is frequency dependent. The relation between the transmission and the experimentally measured absorbance is then given by

$$Abs(\omega) = -\ln [T(\omega)] = -\ln \left| \frac{2k_0\tilde{k}}{2k_0\tilde{k} \cdot \cos(\tilde{k}L) - i(k_0^2 + \tilde{k}^2) \cdot \sin(\tilde{k}L)} \right|^2. \quad (5.5)$$

Finally, we look at the induced change in absorbance, $\Delta Abs(\omega)$, due to the IR pulse. The presence of the pump alters the dielectric function ($\varepsilon \rightarrow \varepsilon + \Delta\varepsilon$) and thus the wave number of the solid. This, in turn, has a direct influence on the absorbance. $\Delta Abs(\omega)$ is defined as follows

$$\Delta Abs(\omega) = Abs_{with\ IR}(\omega) - Abs_{without\ IR}(\omega) = \ln \left[\frac{T_{without\ IR}(\omega)}{T_{with\ IR}(\omega)} \right]. \quad (5.6)$$

By inserting equation (5.4) into (5.6), one can finally show that ΔAbs is directly proportional to the imaginary part of $\Delta\varepsilon$ (see appendix A):

$$\boxed{\Delta Abs(\omega) \propto Im(\Delta\varepsilon(\omega))}. \quad (5.7)$$

Therefore, in the following section, the measured change in absorbance will be compared with the simulated change of the imaginary part of the dielectric function.

5.4 Attosecond Optical-Field-Enhanced Carrier Injection into the GaAs Conduction Band

*F. Schlaepfer¹, M. Lucchini^{1,3}, S. A. Sato², M. Volkov¹, L. Kasmi¹,
N. Hartmann¹, A. Rubio², L. Gallmann¹ and U. Keller¹*

¹ Department of Physics, ETH Zurich, Zurich, Switzerland

² Max Planck Institute for the Structure and Dynamics of Matter, Hamburg, Germany

³ Present address: Department of Physics, Politecnico di Milano, Milano, Italy

Resolving the fundamental carrier dynamics induced in solids by strong electric fields is essential for future applications, ranging from nanoscale transistors [24,102] to high-speed electro-optical switches [88]. How fast and at what rate can electrons be injected into the conduction band of a solid? Here, we investigate the sub-femtosecond response of GaAs induced by resonant intense near-infrared laser pulses using attosecond transient absorption spectroscopy. In particular, we unravel the distinct role of intra- versus interband transitions. Surprisingly, we found that despite the resonant driving laser, the optical response during the light-matter interaction is dominated by intraband motion. Furthermore, we observed that the coupling between the two mechanisms results in a significant enhancement of the carrier injection from the valence into the conduction band. This is especially unexpected as the intraband mechanism itself can accelerate carriers only within the same band. This physical phenomenon could be used to control ultrafast carrier excitation and boost injection rates in electronic switches in the petahertz regime.

Shrinking structure sizes in integrated circuits inevitably lead to increasing field strengths in the involved semiconductor materials [24,102]. At the same time, ultrafast optical technologies enable the extension of operation frequencies of electro-optical devices to the petahertz regime [88]. Both applications ultimately require a deep fundamental understanding of ultrafast electron dynamics in solids in the presence of strong fields for the de-

velopment of the next generation of compact and fast electronic devices. A number of pioneering experiments demonstrated the potential to measure and control carrier dynamics induced by intense near-infrared laser pulses (peak intensity $I_{peak} \sim 10^{12} \text{ W cm}^{-2}$) in semiconductors [20,21,89,90,103] and dielectrics [19,22] on a sub- to few-femtosecond timescale using transient absorption and polarization spectroscopy. So far, resolving such dynamics with attosecond resolution has been limited to the non-resonant excitation regime, where the bandgap of the investigated material is larger than the energy of a single pump photon. Here, in contrast, we unravel the sub-femtosecond response of gallium arsenide (GaAs), a prototype and technologically relevant direct-bandgap semiconductor, in the resonant regime.

Besides the 'vertical' optical transition in the momentum space that corresponds to the absorption of infrared pump photons (so-called interband transition, Fig. 5.2b), the pump field can also accelerate electrons within the electronic bands (intraband motion, Fig. 5.2c). In a simplified picture, one can think of inter- and intraband transitions as a consequence of the dual nature of the pump light that behaves either as photons (interband) or as a classical electromagnetic field (intraband). The role of intra- versus interband transitions in the presence of strong electric fields is highly debated [25–31]. For the infrared intensities used in this experiment, we can neglect contributions from the magnetic laser fields [104].

In a recent publication, we demonstrated that during the interaction of a wide-bandgap dielectric such as diamond with a short, intense, non-resonant infrared pump pulse, intraband motion completely dominates the transient optical response [22]. However, it is still unclear whether and how this situation changes in the technologically much more relevant resonant case where a single photon from the pulse has enough energy to induce an interband transition that creates real carriers in the conduction band (CB). The question of whether intraband motion still dominates the interaction and how the coupling between the two mechanisms influences the carrier injection is not obvious and has not been experimentally investigated so far.

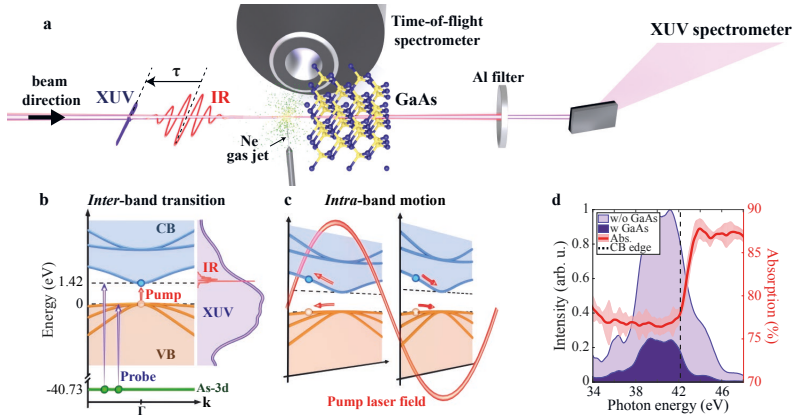


Figure 5.2: Pump-probe mechanism in GaAs. **a**, Schematic diagram of the experimental set-up with the double-target configuration to perform simultaneous streaking and transient absorption spectroscopy. **b,c**, Illustration of the pump-induced dynamics in GaAs. The strong resonant infrared pulse excites carriers either via the absorption of photons from the VB to the CB taking into account nonlinear carrier injection (interband transition, **b**) or accelerates electrons within a band (intra-band motion, **c**). The energy axis is defined with respect to the top of the VB. The bandgap of GaAs at room temperature is ~ 1.42 eV (ref. [105]). The horizontal axis illustrates the crystal momentum k around the Γ symmetry point. The SAP probe measures the distribution of electrons and holes around the bandgap through a transition from the As-3d core levels, lying around 40.73 eV below the VB edge [95], to empty states in the VB and CB (violet arrows). In **b**, the spectra for the infrared and XUV pulses are plotted with respect to the top of the VB and the As-3d core level, respectively. In **c**, the field-induced carrier motion is illustrated for two instants during the interaction with the infrared pump field. **d**, Transmitted SAP spectrum measured with and without a 100-nm GaAs membrane in the beam path. The red solid line (shaded area) represents the mean value (standard deviation) of the absorption extracted from 42 sets of spectra acquired with and without transmission through the sample.

To study the electronic response of GaAs when driven out of equilibrium, we combine a 5-6 fs infrared pump pulse (centre energy $\hbar\omega_{IR} \approx 1.59$ eV) with a delayed phase-locked single attosecond pulse (SAP) probe as illustrated in Fig. 5.2a (further details are given in the Supplementary Information and in ref. [68]). The infrared pump pulse has a peak intensity in vacuum of $\sim 2.31 \pm 0.17 \times 10^{12}$ W cm⁻², which corresponds to a peak electric field of ~ 0.42 V Å⁻¹. The estimated intensity inside the sample reaches up to 60% of the intensity in vacuum. The two beams are focused into a double target that consists of a gas jet followed by a 100-nm-thick single-crystalline GaAs membrane. The neon gas target enables the extraction of the temporal shape of both pulses as well as a precise delay calibration via a simultaneously recorded streaking measurement [38, 53]. We calibrate the time axis of the streaking trace by taking into account the spatial separation of the two targets [49].

The pump-probe principle of attosecond transient absorption spectroscopy is illustrated in Fig. 5.2. The infrared pulse can induce both inter- and intraband transitions. The SAP probes the modified charge distribution by exciting electrons from the *As-3d* core levels to available states around the bandgap region. Figure 5.2d shows the measured static absorption spectrum of the GaAs membrane. It is important to note that the broad extreme-ultraviolet (XUV) spectrum of the SAP simultaneously probes the dynamics in the valence band (VB) and the CB.

Figure 5.3a displays the absorption modification of GaAs induced by the resonant pump pulse, $\Delta\text{Abs}(E, \tau)$ (for definition, see Supplementary Information). A red (blue) region indicates increased (decreased) absorption. In the following analysis, we concentrate on two different delay regimes: (1) when the pump and probe overlap, and (2) when the probe pulse arrives well after the pump.

Without temporal overlap after the infrared pump pulse, we see a long-lasting signal (that is, regime (2) in Fig. 5.3a), which persists after the pump interaction over a considerable delay range. During the interaction, electrons are excited via interband transitions from the VB to the CB. This mechanism fully takes into account the nonlinear injection of carriers (see Supplementary Information). The creation of holes in the VB and elec-

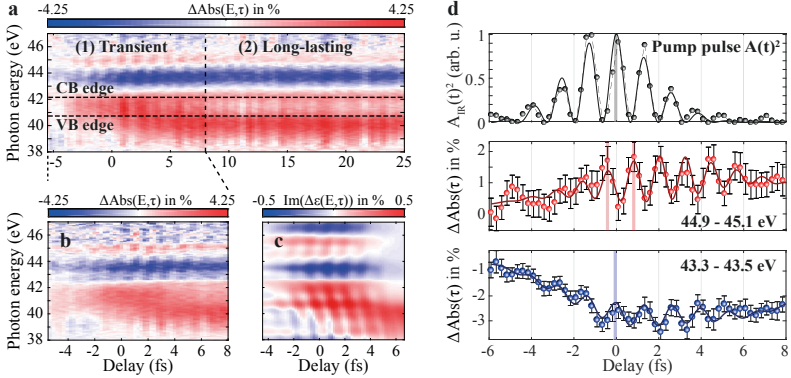


Figure 5.3: Attosecond transient absorption spectroscopy. **a**, Measured infrared-induced absorption change $\Delta\text{Abs}(E,\tau)$. The interaction is divided into two delay windows: (1) transient response during the pump-probe overlap, and (2) lasting signal after the pump interaction. A positive delay means that the infrared pump comes first and the XUV probe second. We applied a frequency filter to the measured data to reduce the high-frequency noise ($\nu > 1$ PHz). The horizontal black dashed lines mark the position of the VB and CB edge of field-free bulk GaAs. Zero delay is defined by the maximum of the squared vector potential of the pump pulse (see Supplementary Information). **b**, Separate scan over region (1) with longer signal integration, which shows the infrared-induced oscillations in the CB with higher signal fidelity. **c**, First-principles simulation of the imaginary part of the dielectric function, $\Im(\Delta\epsilon(E,\tau))$, which describes the absorption modification. A positive energy shift of 4.23 eV is applied to the numerical results to correct for the underestimation of the energy gap between the core level and the VB in the first-principles simulation (see Supplementary Information). **d**, Square of the infrared (IR) vector potential extracted from a simultaneous streaking trace and compared with the measured $\Delta\text{Abs}(E,\tau)$ at 43.4 and 45 eV in **b** (0.2 eV integration widths). The dots represent the experimental data, while the solid lines are fits with an oscillatory function to guide the eye. The vertical lines mark the peak position of the fit closest to zero time delay. The phase offset between the two energy windows is also reflected in the tilted shape of the fast oscillating features in **b**. The error bars for the attosecond transient absorption spectroscopy signals include the standard deviation of the mean extracted from 400 signal-reference means pairs acquired per delay step and the standard deviation due to the signal variation within the finite-energy integration windows.

trons in the CB causes an increased XUV absorption at the upper VB edge (around 40 eV) and a bleached absorption at the lower CB range (around 43 eV), respectively. The system returns to its equilibrium ground state through electron-hole recombination, which happens for bulk GaAs on a timescale of 2.1 ns (ref. [106]). By looking at negative delays, we can see that the absorption of the system recovers completely between subsequent pulses, which means that there are no accumulative effects and heating of the sample by the laser is negligible.

During the temporal overlap of the infrared pump and the XUV probe pulse, we observe a transient signal (that is, regime (1) in Fig. 5.3a), which oscillates with $2\omega_{IR}$ and lasts for the duration of the pump pulse (Fig. 5.3b). The oscillations are visible in a broad probe energy range, most pronounced in the CB between 42.5 and 46 eV. Below 42 eV, they are not well resolved due to stronger fluctuations of the SAP spectral amplitude. However, attosecond transient absorption spectroscopy measurements performed with attosecond pulse trains characterized by a more stable spectrum confirmed the appearance of oscillations also in the VB, around 40 eV (see Supplementary Information).

Figure 5.3d shows the squared vector potential $A(t)^2$ of the measured infrared pump and the measured transient absorbance for two energy windows. A comparison among them reveals a strong energy dependence of the oscillation phase, which is reflected in the tilted shape of the oscillation features in $\Delta\text{Abs}(E,\tau)$.

To understand the microscopic origin of the measured features, we performed a first-principles electron dynamics simulation (see Supplementary Information for details). We simulated the pump-probe experiment [101] and calculated the pump-induced change of the dielectric function including propagation effects, $\Delta\varepsilon(E,\tau)$, which is directly related to the absorption change $\Delta\text{Abs}(E,\tau)$ (ref. [22]). The numerical results show oscillations with a tilted shape and a long-lasting signal, in good agreement with the experiment (Fig. 5.3c).

With a decomposition of the probe Hamiltonian of the first-principles simulation into Houston states [22, 107], we can disentangle the contributions of the two probe transitions (As-3d level to either VB or CB) in the

observed dynamics (see Supplementary Information). The energy range above 42 eV, where the strongest transient signal appears, is dominated by probe transitions from the core level to the CB (Fig. 5.4a). Therefore, in the following, we focus on the CB response.

In a previous study [22], we demonstrated that a non-resonant pump can excite virtual electrons on a sub-femtosecond timescale via intraband motion. Virtual electron excitations live only transiently during the presence of the driving field. For the present experiment, the resonant part of the pump radiation will also inject real carriers into the CB via interband transitions. A population of real carriers persists after the driving pulse has passed and decays orders of magnitude slower than the timescale considered here. To study the ultrafast carriers, we have to investigate the respective signal contributions of infrared-induced intra- and interband transitions. Therefore, we simplify the description of our system to a three-band model, which includes the *As-3d* level, the light-hole VB and the lowest CB (see Supplementary Information). The advantage of the three-band model is that intraband motion and interband transitions between the VB and CB can be numerically included or excluded. Figure 5.4b shows the CB response with both types of transition involved. The good qualitative agreement with the first-principles decomposition (Fig. 5.4a) justifies the use of this model to study the respective optical response induced by the two mechanisms.

In the intraband limit, no real electrons are excited from the VB to the CB [108]. This explains why the dielectric function of GaAs fully recovers immediately after the pump pulse (Fig. 5.4c). In the interband limit, real carriers are injected into the CB by resonant photon absorption, thus resulting in the blue long-lasting signal around 43 eV (Fig. 5.4d).

In both cases, absorption oscillations with twice the pump frequency appear (Fig. 5.4e). They originate from the dynamical Franz-Keldysh effect (DFKE) [22,109] (intraband limit) and the dynamical Stark effect [110] (interband limit). In contrast to the interband case, the intraband limit clearly shows the strong energy dispersion as in the experiment. In addition, a closer look reveals that the intraband trace oscillates nearly in phase with the decomposed first-principles simulation and therefore with the ex-

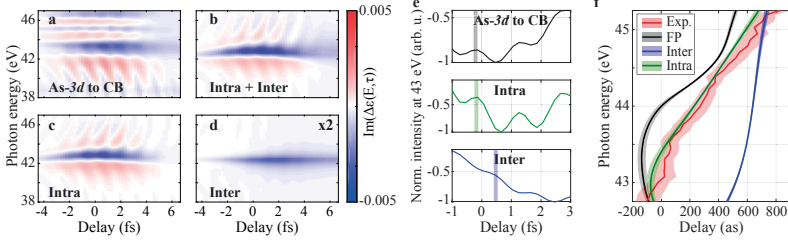


Figure 5.4: Simulated energy- and delay-dependent change of the absorbance. **a**, Houston decomposition of the first-principles result considering only the As-3*d* to CB probe transition. **b**, Conduction band response in the case of a simplified three-band model. **c,d**, The same calculation as in **b** but for the intraband (**c**) and interband (**d**) limit. **e**, Signal at 43 eV (0.2 eV integration width) extracted from **a**, **c** and **d**. **f**, Comparison of the energy-dependent delay between the driving field and the absorption response extracted from the experiment, the first-principles (FP) simulation and the three-band model in the inter- and intraband limit. The experimental delay is the statistical average of nine measurements recorded on four different days. The shaded areas represent the corresponding weighted error bars (see Supplementary Information for details about the extraction method and error definition). The intraband limit calculation is in good agreement with the experiment. The first-principles calculation shows a qualitatively similar trend, however with less good agreement. The residual temporal offset could result from the longitudinal dependence of the infrared intensity in the bulk material (see Supplementary Information). On the other hand, the interband case clearly fails to reproduce the experiment even qualitatively.

perimental results, while the inter-band picture clearly fails to reproduce the experimental phase (Fig. 5.4e).

To further verify this, we compare the energy dispersion of the oscillation delay between the measured and simulated signal for the different models and limits (Fig. 5.4f). The pure interband case of the three-band model fails to reproduce the experiment while the delay of the intraband limit shows excellent agreement with the experimental results. Therefore, by looking at the attosecond timing of the transient signal, we can conclude that infrared-induced intraband motion (namely the DFKE) dominates the ultrafast response in the CB of GaAs during the pump-probe overlap even in a resonant pumping condition. This is a surprising result, as in the case of a resonant intense pump it is believed that one should not be able to observe DFKE around the bandgap [22, 108, 109].

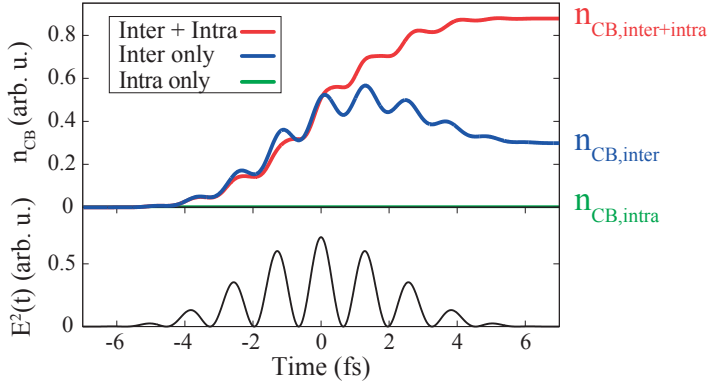


Figure 5.5: Time evolution of the real electron population n_{CB} in the CB extracted from the three-band model. The lower panel displays the square of the instantaneous infrared electric field. Time zero corresponds here to the maximum of the field intensity. In the upper panel, the blue and green curves are the calculated CB populations in the inter- and intraband limit, respectively. Rabi-flopping is responsible for the partial depopulation of the CB during the second part of the pump interaction in the interband limit. Intraband motion does not excite any real carriers into the CB itself. The red curve shows the population with both transition mechanisms involved, intra- and interband. Surprisingly, including intraband motion results in a significantly larger amount of photo-excited carriers compared to the interband limit.

Finally, we look at the injection of real carriers from the VB into the CB. We define the CB population, n_{CB} , by the projection of the time-dependent wavefunction of the three-band model on the CB state (see Supplementary Information). In the case of neglected intraband motion (only interband transitions), the calculation predicts a stepwise oscillating increase of n_{CB} following the intensity of the pump pulse (Fig. 5.5). During the second part of the pump interaction, Rabi-flopping partly depopulates the CB. Surprisingly, in the realistic case involving both excitation mechanisms, the amount of excited carriers increases by nearly a factor of three compared to the model with only interband transitions. This result shows that, although intraband motion does not create real carriers in the CB by itself [108], it assists in the carrier injection initiated by the resonant part of the pump. This indicates that the nonlinear interplay between intra- and interband transitions opens a new excitation channel via virtually excited

states at high pump intensities. It is worth emphasizing that the observed enhancement of the injection rate can also be seen in the multi-photon resonant pump regime (see Supplementary Information). Further, it does not depend on the pulse duration. However, using significantly longer pulses or continuous-wave laser light with the same field strength could lead to the target being irreversibly damaged.

To conclude, our measurements and simulations reveal the mechanisms of the sub-femtosecond electron injection in GaAs driven by intense and resonant infrared laser pulses. In contrast to expectations, our results demonstrate that ultrafast transient absorption features, which characterize the early response of the semiconductor to the resonant pump excitation, are dominated by intraband motion, rather than by interband transitions. Furthermore, our simulations show that the virtual carriers created by the intraband motion assist in the injection of real carriers from the VB into the CB. Hence, the interplay between both transition types significantly influences the injection mechanism in the presence of strong electric fields. This process is expected to be universal and persist in a large range of excitation parameters. Therefore, our observation reveals important information about sub-femtosecond electron dynamics in a solid induced by strong fields, which is required for the scaling of the next generation of efficient and fast optical switches and electronics driven in the petahertz regime.

Data availability. The data that support the plots within this paper and other findings of this study are available from the corresponding author upon reasonable request.

Acknowledgements. We thank M. C. Golling for growing the GaAs, and J. Leuthold and C. Bolognesi for helpful discussion. The authors acknowledge the support of the technology and cleanroom facility at Frontiers in Research: Space and Time (FIRST) of ETH Zurich for advanced micro- and nanotechnology. This work was supported by the National Center of Competence in Research Molecular Ultrafast Science and Technology (NCCR MUST) funded by the Swiss National Science Foundation, and by JSPS KAKENHI grant no. 26-1511.

Author contributions. F.S., M.L., L.G. and U.K. supervised the study. F.S., M.L., M.V., L.K. and N.H. conducted the experiments. M.V. also improved the experimental set-up and data acquisition system. F.S. fabricated the sample and analysed the experimental data. S.A.S. and A.R. developed the theoretical modelling. All authors were involved in the interpretation and contributed to the final manuscript.

5.5 Attosecond Carrier Dynamics in $\text{Al}_{0.8}\text{Ga}_{0.2}\text{As}$

Similar to the studies discussed in the previous section, transient absorption measurements have been performed in $\text{Al}_{0.8}\text{Ga}_{0.2}\text{As}$, which is an indirect semiconductor. The VB maximum lies at the Γ -point and the minimum of the CB is located at the X -point (see section 5.2). The indirect bandgap is ~ 2.09 eV, the direct one at the Γ -point is ~ 2.57 eV [99]. Thus, at least two 800-nm IR photons ($E_{IR} \approx 1.59$ eV) are required to excite an electron from the VB to the CB. While the IR-pump mechanism was in resonance in GaAs, it is non-resonant in $\text{Al}_{0.8}\text{Ga}_{0.2}\text{As}$. In the previous section, we found that the ultrafast optical response in GaAs is dominated by intraband motion, rather than by interband transitions. Taking the non-resonant pump condition into account, it can be expected to observe a similar response in $\text{Al}_{0.8}\text{Ga}_{0.2}\text{As}$.

We would like to note that this section contains preliminarily experimental results. The corresponding simulations are in progress. The interpretations of the $\text{Al}_{0.8}\text{Ga}_{0.2}\text{As}$ measurements are based so far on the findings in GaAs.

5.5.1 $\text{Al}_{0.8}\text{Ga}_{0.2}\text{As}$ Sample

The $\text{Al}_{0.8}\text{Ga}_{0.2}\text{As}$ samples are free-standing single crystalline membranes with a thickness of 100 nm. The fabrication process is similar to the one of a GaAs membrane (see section 3.3). While GaAs is quite resistant to oxidation, it can play a crucial role in $\text{Al}_x\text{Ga}_{1-x}\text{As}$ with a large Al content [111]. Therefore, the time between fabrication and measurement has been kept as short as possible. Nevertheless, the yellowish brown color of the $\text{Al}_{0.8}\text{Ga}_{0.2}\text{As}$ membrane shown in figure 5.6 indicates surface oxidation [112]. The influence of the oxidation on the transient absorption measurements is not yet clarified and needs to be further investigated. The wavy surface of the membrane is a results of the growth and fabrication process. The 100-nm-thick AlGaAs layer is grown by MBE on a GaAs wafer. The lattice constants for GaAs and $\text{Al}_{0.8}\text{Ga}_{0.2}\text{As}$ are 5.6533 Å and 5.65954 Å. Thus, the $\text{Al}_{0.8}\text{Ga}_{0.2}\text{As}$ crystal is squeezed during the growth. After the etching step of the supporting GaAs wafer, the free-standing membrane relaxes and becomes slightly curved.

The carrier dynamics in the $\text{Al}_{0.8}\text{Ga}_{0.2}\text{As}$ crystal are induced by IR pulses with an energy of $1.6 \mu\text{J}$, which is just below the experimentally observed damage threshold. Compared to the IR pulses used in the GaAs study, the pulse energy used here is slightly lower.

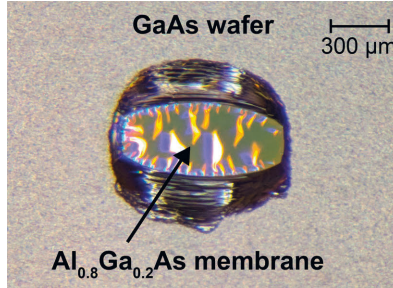


Figure 5.6: Picture of a free-standing 100-nm-thick $\text{Al}_{0.8}\text{Ga}_{0.2}\text{As}$ membrane.

5.5.2 Static XUV Absorption

The static XUV absorption of GaAs and $\text{Al}_{0.8}\text{Ga}_{0.2}\text{As}$ is shown in figure 5.7. For GaAs, the energy gaps from the As-3*d* core level to the VB maximum and CB minimum correspond to 40.73 eV and 42.15 eV, respectively. Clearly, the XUV absorption increases for energies above the CB edge (solid black line).

As described in reference [113], the binding energy of the As-3*d* core level is reduced by 0.6 eV in AlAs compared to that in GaAs. If we assume a linear relation between the shift and the Al concentration, we expect a core level shift of 0.48 eV for a concentration of $x=0.8$. Then the energy gap between the As-3*d* level and VB top is expected to be 40.25 eV in $\text{Al}_{0.8}\text{Ga}_{0.2}\text{As}$. Assuming the core level to be flat in the reciprocal space, the minimum energy difference between the core level and the CB is located at the X-point and equal to 42.34 eV (black dashed line). However, as shown in figure 5.7, the absorption increases already below this estimated CB edge, which is not yet fully understood. As shown in reference [114], oxidation can also lead to a shift of the binding energy. An increase of

up to 1 eV has been observed. Such a shift of the CB edge to even higher energies would however not match with the measured absorption curve. The influence of oxidation needs to be further investigated.

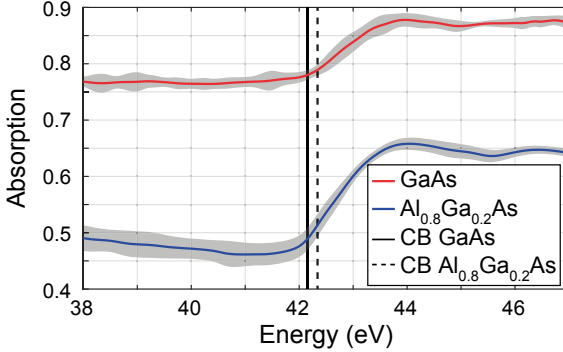


Figure 5.7: Measured static absorption of 100-nm GaAs and $\text{Al}_{0.8}\text{Ga}_{0.2}\text{As}$. The vertical lines mark the energy of the CB bottom with respect to the As-3d core level. The GaAs data have been extracted from [59]. The blue solid line and corresponding confidence interval represent the mean value and standard deviation of three absorption measurement series recorded with two different $\text{Al}_{0.8}\text{Ga}_{0.2}\text{As}$ samples.

5.5.3 Transient Absorption Spectroscopy

The energy- and delay-dependent absorbance change induced by an IR pulse in an $\text{Al}_{0.8}\text{Ga}_{0.2}\text{As}$ membrane is shown in figure 5.8(a). Here, an APT with spectrally broad HHs has been used as a probe. The advantage of using an APT with broad HHs instead of a SAP was a more stable spectrum. Since the wings of neighboring HHs were partly overlapping, the absorption modification could still be recorded continuously over a wide energy window.

$\Delta Abs(E, \tau)$ of $\text{Al}_{0.8}\text{Ga}_{0.2}\text{As}$ resembles much the one of GaAs (figure 5.8(a) vs. (b)). The phase of the transient absorption oscillations depends strongly on the probe energy, indicated by the black lines. Further, one can see that the change in absorbance is in $\text{Al}_{0.8}\text{Ga}_{0.2}\text{As}$ about six times weaker than in GaAs. This might be due to the lower peak intensity of the used pump pulses.

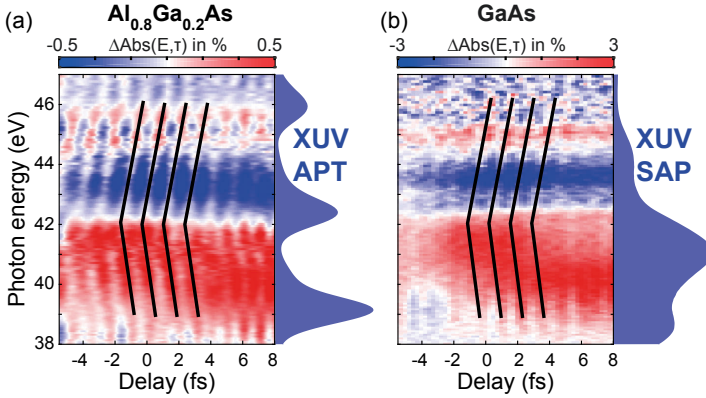


Figure 5.8: Transient absorbance change of an $\text{Al}_{0.8}\text{Ga}_{0.2}\text{As}$ and GaAs membrane. (a) Measured signal in $\text{Al}_{0.8}\text{Ga}_{0.2}\text{As}$ with an APT with spectrally broad HHHs. To reduce the fast noise ($\nu > 1$ PHz), a frequency filter is applied to the data. (b) Same in GaAs measured with a SAP. Panel (b) is adapted from [59].

5.5.3.1 Energy Dependence of Oscillation Delay

The phase of the observed transient absorption oscillations depends strongly on the XUV energy, both for GaAs and $\text{Al}_{0.8}\text{Ga}_{0.2}\text{As}$. The red curve in figure 5.9 shows the absolute delay between the squared vector potential $A^2(t)$ of the driving laser and the absorption oscillation measured in GaAs with a SAP (see section 5.4, [59]). The green and blue curves illustrate the oscillation delay measured with APTs in GaAs and $\text{Al}_{0.8}\text{Ga}_{0.2}\text{As}$. With the SAP, the phase could only be extracted between 42.5 to 45.5 eV due to strong amplitude fluctuations outside of this energy window. The disadvantage of using an APT was however that no streaking measurement could be performed simultaneously with the ATAS measurement. Thus, only a relative delay could be extracted. The extracted green and blue curves are shifted along the delay axis to overlap at 44 eV with the absolute delay measured in GaAs (red curve). Interestingly, there is a close to perfect overlap between the shape of the two materials in the full energy window shown.

In addition, figure 5.9 contains the delay simulated for a GaAs membrane (black dash-dot line, see section 5.4). The first-principle simulation

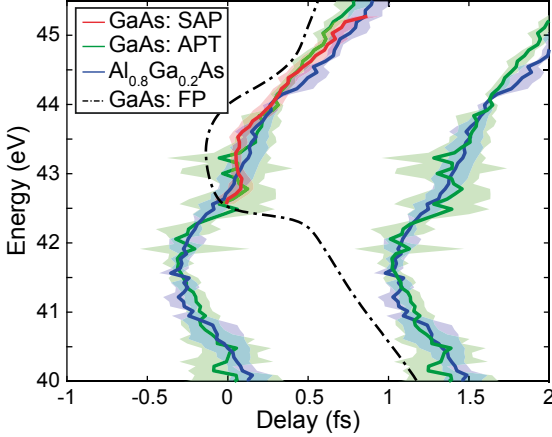


Figure 5.9: Energy dependence of the oscillation delay. Red and green curves are the delays for GaAs measured with a SAP and an APT, respectively. The blue curve is the delay for $\text{Al}_{0.8}\text{Ga}_{0.2}\text{As}$. The dash-dot line shows the first-principle (FP) simulation for GaAs. A copy of the green and blue curves shifted by one oscillation period is plotted for illustration purposes. The error bar of the green and blue curves represent the standard deviation of 5 and 3 measurements, respectively. The red and dash-dot lines are extracted from [59].

of an $\text{Al}_{0.8}\text{Ga}_{0.2}\text{As}$ membrane is in progress. The GaAs simulation matches with the measurement in the energy region above 42.5 eV. Between 42 and 42.5 eV, the calculation experiences however a strong change in slope, which has not been observed in the experiment. Below 42 eV, the simulated GaAs delay reproduces again qualitatively the measured one. For a better comparison, a copy of the green and blue experimental traces shifted by one oscillation period are plotted.

The reason for the deviation between 42 and 42.5 eV is under further investigation. A possible explanation might be the propagation effect. In the current simulation, the propagation of the IR and XUV beam through the membrane is taken into account by simply averaging the ATAS signal over a certain pump-probe delay window (see section B.2.2). We suggest performing a multi-scale simulation, which couples the ab-initio electron dynamics calculation with Maxwell's equation (similar to reference [22]). This would allow taking the propagation more accurately into account.

5.5.4 Conclusion of Carrier Dynamics in $\text{Al}_{0.8}\text{Ga}_{0.2}\text{As}$

To conclude, preliminarily results of transient absorption measurements performed in $\text{Al}_{0.8}\text{Ga}_{0.2}\text{As}$ have been presented in this section. During the presence of an intense IR pump pulse, transient oscillations in the XUV absorbance have been observed. The energy-dependent phase of the oscillation resembled strongly the one measured in GaAs. This indicates that the same physical mechanism as in GaAs is dominating the ultrafast optical response, namely the intraband motion. Given that $\text{Al}_{0.8}\text{Ga}_{0.2}\text{As}$ has a larger bandgap than GaAs, it was actually expected that the interband transition plays an even less important role in the ultrafast response.

So far, the conclusions of the dynamics in $\text{Al}_{0.8}\text{Ga}_{0.2}\text{As}$ are based on the results observed in GaAs. Simulations of an $\text{Al}_{0.8}\text{Ga}_{0.2}\text{As}$ membrane are in progress to support the above interpretations.

Additionally, the influence of oxidation is not fully understood at the present time. Ideally, the membrane would be coated with a protective layer to prevent oxidation. However, the implementation of a coating layer is non-trivial, since it needs to be compatible with the growth and fabrication process and, in addition, transparent for the XUV radiation.

Attosecond Pump-Probe Beamline involving Two-IR Colors

To the best of our knowledge, this chapter presents the first active phase-stabilized attosecond pump-probe beamline involving two separate IR-colors. The output of the Ti-sapphire power amplifier system is partly used to generate attosecond pulses via HHG and partly to pump an OPA that converts the Ti-sapphire beam to a longer wavelength. The generated beams are recombined after a more than 20-m-long Mach-Zehnder interferometer. Here, a new approach for stabilizing the relative phase between the pump and probe pulses to within 500 as rms is demonstrated, without the need of an auxiliary cw laser. This upgrade allows tuning the OPA output wavelength fully decoupled from the HHG process. Thus, the IR wavelength used in the pump-probe experiment can be tuned without affecting the spectrum of the attosecond XUV radiation. This yields a broad spectrum of potential future experiments, for example the study of the theoretically predicted wavelength-dependence of pump-induced carrier dynamics in condensed matter [22,115].

Details about the publication printed in this chapter are listed below. The text and figures are as in the publication. Only the style of the text, figures and equations has been adapted to the style of the thesis. Further, the numbering of the figures and references has been adjusted. The reference list of the publication has been included in the reference list of the thesis.

Title: "Phase stabilization of an attosecond beamline combining two IR colors", [116]

Journal: *Optics Express*

doi: 10.1364/OE.27.022385

URL: <https://doi.org/10.1364/OE.27.022385>

Published: 23th July 2019

©2019 Optical Society of America. One print or electronic copy may be made for personal use only. Systematic reproduction and distribution, duplication of any material in this paper for a fee or for commercial purposes, or modifications of the content of this paper are prohibited.

6.1 Phase Stabilization of an Attosecond Beamline combining Two IR Colors

*F. Schlaepfer^{1,2,4}, M. Volkov^{1,2,3,5}, N. Hartmann¹, A. Niedermayr¹,
Z. Schumacher¹, L. Gallmann¹ and U. Keller¹*

¹ Department of Physics, ETH Zurich, 8093 Zurich, Switzerland

² These authors contributed equally to this work.

³ Current address: Ludwig-Maximilians-Universität München, 85748 Garching, Germany

⁴ *f.schlaepfer@phys.ethz.ch*

⁵ *volkovm@phys.ethz.ch*

We present a phase-stabilized attosecond pump-probe beamline involving two separate infrared wavelengths for high-harmonic generation (HHG) and pump or probe. The output of a Ti:sapphire laser is partly used to generate attosecond pulses via HHG and partly to pump an optical parametric amplifier (OPA) that converts the primary Ti:sapphire radiation to a longer wavelength. The attosecond pulse and down-converted infrared are recombined after a more than 20-m-long Mach-Zehnder interferometer that spans across two laboratories and separate optical tables. We demonstrate a technique for active stabilization of the relative phase of the pump and probe to within 450 as rms, without the need for an auxiliary continuous wave (cw) laser. The long-term stability of our system is demonstrated with an attosecond photoelectron streaking experiment. While the technique has been shown for one specific OPA output wavelength (1560 nm), it should also be applicable to other OPA output wavelengths. Our setup design permits tuning of the OPA wavelength independently from the attosecond pulse generation. This approach yields new possibilities for studying the wavelength-dependence of field-driven attosecond electron dynamics in various systems.

6.1.1 Introduction

Typically, attosecond beamlines combine a few-cycle infrared (IR) pulse with an attosecond extreme-ultraviolet (XUV) pulse in a pump-probe setup. The XUV radiation is produced from a primary IR beam via HHG. To date, most of the setups rely on a single IR wavelength for HHG and as a pump or probe in the experiment. The stability of the pump-probe delay represents a challenge for resolving sub-femtosecond dynamics. For example, a change of the relative path length between the pump and probe arms of the setup by 100 nm results in a delay offset by 330 as. Hence, the implementation of an active delay stabilization system can be crucial for enabling accurate attosecond measurements - in particular over extended measurement times [72, 117, 118].

An often adopted attosecond beamline design incorporates a Mach-Zehnder interferometer for the pump and probe beams [39, 68]. A fraction of the IR laser beam is split off before the HHG target and later recombined with the generated XUV radiation via a center-hole mirror. In this case, the two arms of the interferometer extending from the beam splitter to the recombination point can be stabilized against each other using an auxiliary continuous wave (cw) laser. Delay stability within few tens of attoseconds has been demonstrated using this approach [60, 72, 118].

Recently, an experiment has emerged that involves two separate IR colors for HHG (1800 nm) and probe (800 nm) [119]. The XUV generated by the long-wavelength driver is recombined with the 800-nm pulse to perform a pump-probe experiment. Passive delay stability of this system was sufficient for resolving molecular dynamics on a time scale of few tens of femtoseconds. Improving the temporal resolution to the attosecond regime, however, requires active stabilization of the pump-probe delay.

In this paper, we present what is to our knowledge the first actively stabilized two-IR-color setup (780 nm, 1560 nm) with a sub-femtosecond temporal resolution. The use of an auxiliary, common-path cw laser is unpractical in a two-color beamline since an OPA system is installed in one of the pump-probe arms for the conversion of the primary Ti:sapphire beam to the desired longer wavelengths. Numerous dielectric and dichroic optics in the interferometer arms are an additional obstacle. Our approach,

presented in detail below, actively stabilizes the phase between the two separate IR colors. The relative phase stability is essential to resolve ultrafast dynamics, since most attosecond measurement techniques, as the attosecond streak camera [53], extract the time information via a phase analysis of a pump/probe induced oscillation [12, 15, 46, 85]. We demonstrate a long-term rms delay stability below 500 as despite the pump-probe interferometer arms having a length of approximately 23 m and spanning between two laboratories. We perform a proof-of-principle photoelectron streaking measurement to demonstrate the importance of the active stabilization. The stabilization approach should be applicable also for other OPA output wavelengths, as long as the second harmonic spectrum of the OPA partly overlaps with the shorter IR-wavelength.

Our beamline design allows for tuning of the photon energy of the IR pulse used in the pump-probe experiment without affecting the spectral shape of the generated XUV attosecond pulse. This will enable a frequency-dependent investigation of optical-field-induced carrier dynamics in condensed matter systems, such as the dynamical Franz-Keldysh effect [22, 115].

6.1.2 Laser and Pump-Probe Schemes

We use a commercial Ti:sapphire chirped-pulse-amplified (CPA) laser system providing near-infrared (NIR) pulses at a center wavelength of about 780 nm and operating at a repetition rate of 1 kHz. The carrier envelope offset phase (CEP [120]) is actively stabilized. A sketch of the experimental setup is shown in Fig. 6.1. The output beam of the CPA system propagates through a spatial beam cleaning system and is compressed with a combination of gratings and chirped mirrors to about 25 fs. The beam with a remaining energy of 7 mJ is divided into two parts. One part is used to pump an OPA, the other one generates attosecond high-harmonic radiation. The beam paths are described in detail below. The OPA output and attosecond pulse are finally recombined, comprising a 23-m-long Mach-Zehnder interferometer partly exposed to air and crossing between two rooms and two optical tables. The two beams are focused into the interaction chamber by a toroidal mirror. For our proof-of-principle measurement, the interaction chamber is equipped with a gas nozzle and a time-of-flight electron

spectrometer. We use several beam pointing stabilization systems (MRC, Femtolasers) in the first room with the laser systems and an additional one (Thorlabs) for the routing of the two beams via an evacuated tube to the second room with the experimental chamber.

The path length from the CPA system to the OPA accumulates to several meters due to the particular space constraints of our laboratory. The peak power of the laser pulses after compression is around 250 GW and thus significantly exceeds the critical power for self-focusing in air (10 GW [121]). As a result, any beam inhomogeneity originating from the multi-pass CPA system can be rapidly amplified by the Kerr effect within a few meters of beam routing, leading to the formation of hot spots. To mitigate this, the CPA laser output is propagated through a spatial beam cleaning system, specially designed for high-peak-power radiation. Since the peak intensity of the focused beam after compression would exceed the breakdown threshold of any material, the beam cleaning system is placed before the grating compressor (Fig. 6.1). The beam is focused onto a Fourier-plane aperture mounted inside an evacuated tube. The spatial filter is a 3-mm long slice of a fused silica hollow-core fiber with an inner diameter of 420 μm . The focusing mirror has a radius of curvature of 4 m, which results in a nominal spot size of $\sim 275 \mu\text{m}$ ($1/e^2$ beam width).

The cleaned and compressed beam is divided with an 85/15 beam splitter (BS) into two beam paths. The smaller fraction (15%) is further compressed using a filament compressor [68]. It is then guided through a polarization gating (PG [39]) setup and finally used for HHG in argon. Depending on the amount of pulse compression and the orientation of the birefringent crystals in the PG setup, either an attosecond pulse train (APT) or a single attosecond pulse (SAP) can be generated, both having a spectrum in the extreme-ultraviolet (XUV) energy regime. After the HHG gas target, a 100-nm-thick aluminum foil in the beam path filters out the residual NIR radiation.

The beam containing the 85% of the original laser output after reflection on the beam splitter is sent to an OPA from Light Conversion (HE-TOPAS prime). The output wavelength of the signal and idler of the OPA can be tuned between 1160-1600 nm and 1600-2600 nm, respectively. In the

present study, we use the signal wavelength set at 1560 nm. To avoid confusion between the Ti:sapphire (780 nm) and TOPAS (1560 nm) outputs, we label them from now as *NIR* and *OPA* beams. The OPA pulses have an energy of up to 630 μJ and a duration of approximately 40-45 fs. The OPA beam propagates further via a delay line equipped with a piezo-controlled stage and is finally recombined collinearly with the XUV radiation on the center-hole mirror, see Fig. 6.2(a).

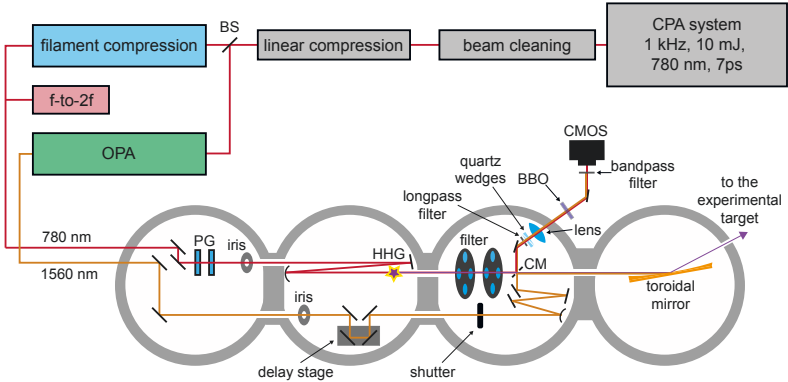


Figure 6.1: Ti:sapphire laser system, OPA and pump-probe scheme. The beam profile of the CPA output is cleaned before the linear pulse compression. An *f*-to-2*f* interferometer installed after the nonlinear filament compression monitors slow CEP drifts of the NIR radiation and feeds an error signal to an actuator in a phase-locked loop. The interferometer spans from the beam splitter (BS) to the center-hole mirror (CM) used for recombination. The optics on the path toward the CMOS camera is described in detail in the text and Fig. 6.2.

6.1.3 Phase Stabilization Scheme

The established method of using an auxiliary cw laser to stabilize the pump-probe interferometer, as described in [72], is not possible due to the OPA being present in one of the arms and numerous incompatible dielectric and dichroic optics along the beam paths. In this section, we present our approach to directly stabilize the phase between the two IR colors without the need for any additional laser.

As illustrated in Fig. 6.2(a), we use an aluminum foil after the HHG

target with a slightly smaller diameter than the NIR beam. The foil is held by a glass plate, similar to [118]. This allows the outermost part of the NIR beam to pass around the filter. The subsequent center-hole mirror geometrically separates the transmitted donut-shaped NIR from the central XUV beam. The XUV propagates through the hole and the NIR is reflected from the backside of the mirror. The OPA beam hits the center-hole mirror on the front side. While most of the OPA beam is reflected, a small fraction passes through the hole and can be used together with the residual NIR for the active phase stabilization.

The two beams are focused into a BBO crystal, which is optimized for second order harmonic generation of the OPA wavelengths. The spectra of the NIR and the second harmonic of the OPA overlap sufficiently over a sizeable fraction of the OPA tuning range. A narrow band-pass filter with a center wavelength of 780 nm ($\text{FWHM} = 10 \pm 2$ nm) is placed behind the BBO. The interference pattern resulting from the NIR and the OPA second harmonic is recorded with a CMOS camera placed behind the filter. While a small change of the angle between the two interfering beams on the camera can cause a change of the spatial frequency of the fringes, it does not affect the value of their phase. The phase is only affected by changes of the individual interferometer path lengths, which is exactly what is to be stabilized by our scheme. It is important to note that our system stabilizes the relative phase of the two pulses, rather than just their envelopes. This is very important for phase-sensitive attosecond pump-probe measurements.

Further, it would also be possible to record the spectral interference with a spectrometer instead of the spatial fringes with the CMOS camera. Such a spectrometer, however, would need sufficient resolution to resolve the interference fringes across the entire delay range to be scanned. Furthermore, a spectrometer adds additional cost compared to a CMOS camera and a band-pass filter.

However, our approach of stabilizing the NIR and OPA pulses without the help of an auxiliary laser presents some challenges and limitations:

- (i) CEP-stability of both pulses, NIR and OPA, is required for observing stable interference fringes.
- (ii) The interference signal on the camera occurs only if the two spectrally

filtered pulses are within a coherence length of each other, which limits the delay window for stabilization.

With the narrow band-pass filter used in our present implementation, we measured interference fringes during a pump-probe delay window of roughly 100 fs. This corresponds to about 19 optical cycles of the OPA pulse. In addition to the intrinsic limitations listed above, we observed a setup-specific issue, which had to be taken into account. Our design of the laser beam paths implies that when the XUV and OPA pulses temporally overlap at the experimental target, the NIR and OPA pulses going towards the CMOS camera are temporally separated. The reason for this is illustrated in Fig. 6.2(a). After the HHG process, the NIR and XUV overlap in time. The outer part of the NIR beam passes through the glass mount and is thereby delayed with respect to the HHG radiation. In addition, the NIR reflection on the center-hole mirror, which is coated on the OPA facing side, results in a further delay, as the NIR beam has to cross the mirror substrate twice. As a consequence, in the case of setting the XUV and OPA pulse to temporally overlap in the experimental target, the OPA and NIR pulses reaching the CMOS camera are delayed by about 6.6 ps with respect to each other for our design parameters.

Taking into account that the pulse durations of the NIR and OPA are less than 50 fs, it is necessary to compensate for the accumulated delay to observe interference fringes on the camera while the OPA/XUV pulses overlap at the experimental target. To do so, we use additional delay-compensating optical elements, see Fig. 6.2(b). A longpass filter (cut-on wavelength: 1000 nm) and a pair of motorized fused silica wedges are installed and vertically aligned so that the OPA propagates through them while the NIR is partly blocked by the filter. The additional glass delays the OPA with respect to the NIR. Hence, by tuning the amount of glass in the beam path, the simultaneous overlap in the experimental target and on the CMOS camera can be achieved. The wedges could in principle also be used to extend the delay range that can be stabilized beyond the limit mentioned above.

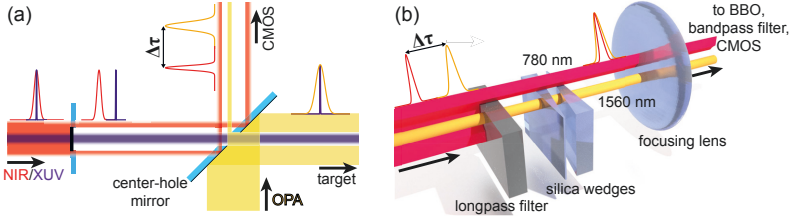


Figure 6.2: Delay compensation. (a) NIR (red), XUV (violet) and OPA (yellow) beam paths. When the XUV and OPA pulses overlap in time in the experimental target, the NIR is delayed compared to the OPA pulse on the CMOS camera by about $\Delta\tau = 6.6$ ps. (b) Additional optics installed before the camera to compensate for the acquired delay. The temporally overlapping pulses are finally focused with a lens into a BBO crystal for second order harmonic generation of the OPA beam, followed by a narrow band-pass filter (center wavelength: 780 nm, FWHM = 10 ± 2 nm) and a CMOS camera.

6.1.4 Active Interferometric Stabilization (AIS) Algorithm

As mentioned above, CEP stability is required to observe stable interference fringes. The CEP stabilization of the Ti:sapphire amplifier system consists of two loops. The fast loop acts on the oscillator and locks the carrier-envelope offset frequency to $1/4$ of the repetition rate, which translates to a constant CEP φ_{NIR}^{CEP} after the pulse-picker of the amplifier. The slow loop compensates long-term CEP drifts by adjusting a wedged glass element in the amplifier's bulk glass stretcher. Since the OPA seed is produced via white-light generation, the CEP of the OPA signal is equal to the one of the NIR pulse, $\varphi_{NIR}^{CEP} = \varphi_{OPA}^{CEP}$. At the same time, the frequency-doubled signal of the OPA used to produce interference fringes on the camera for active phase stabilization carries twice that offset, $\varphi_{SH}^{CEP} = 2\varphi_{NIR}^{CEP} + \frac{\pi}{2}$. The $\frac{\pi}{2}$ results from the second harmonic (SH) generation. As a result, the interference patterns forming on the camera are directly influenced when tuning φ_{NIR}^{CEP} :

$$\begin{aligned}
 \Delta\varphi &= \varphi_{SH} - \varphi_{NIR} \\
 &= [\varphi_{SH}^{CEP} - \varphi_{NIR}^{CEP}] + \Delta\varphi_{path}, \\
 &= \varphi_{NIR}^{CEP} + \frac{\pi}{2} + \Delta\varphi_{path}
 \end{aligned} \tag{6.1}$$

where $\Delta\varphi$ is the phase difference between the NIR and the second harmonic of the OPA detected at the CMOS camera. Thus, $\Delta\varphi$ includes the phase difference due to the path difference in the interferometer, $\Delta\varphi_{path}$, as well as the CEP of the NIR, φ_{NIR}^{CEP} . Since the feedback of the AIS only acts on $\Delta\varphi_{path}$ while still detecting φ_{NIR}^{CEP} , it is crucial to minimize any CEP fluctuations. With our system, the CEP of the NIR could be stabilized to a rms value of <0.18 rad, which corresponds to 75 as. Without having the CEP stabilization running, no interference fringes can be observed on the camera.

Figure 6.3 shows the schematic of the home-built proportional-integral-derivative (PID) software to stabilize the relative phase $\Delta\varphi$ between the NIR and OPA pulses. The stabilization loop consists of the phase extraction algorithm and the PID-controlled feedback to the piezo-driven delay stage and runs at 431 Hz, limited by the camera readout rate. This frequency is significantly higher than the dominating mechanical instabilities of the setup (<40 Hz), as was confirmed with an independent accelerometer measurement. The high acquisition rate allows for tracking the delay also in the event of occasional fast, high-amplitude mechanical perturbations. Given the short path length and the common path of the NIR and OPA beams between the center-hole mirror and the camera, we assume the noise contributions acquired in this part of the setup to be negligible compared to the fluctuations from the 23 m long interferometer arms. This assumption is supported by the attosecond streaking experiment reported in section 6.1.5.

From time to time, the CEP stabilization is interrupted, e.g. when the oscillator loop moves the intra-cavity glass wedges that are used for coarse adjustment of the CEP offset. The resulting very fast CEP jumps cannot be distinguished from changes in the propagation phase $\Delta\varphi_{path}$ by our detection system and ultimately lead to loss of the phase tracking. To overcome this issue, an additional logical signal, shown as the green arrow in Fig. 6.3, is implemented in the PID software. It interrupts the phase acquisition from the CMOS while the CEP is unstable. The last measured phase is kept for subsequent tracking once CEP stability is regained.

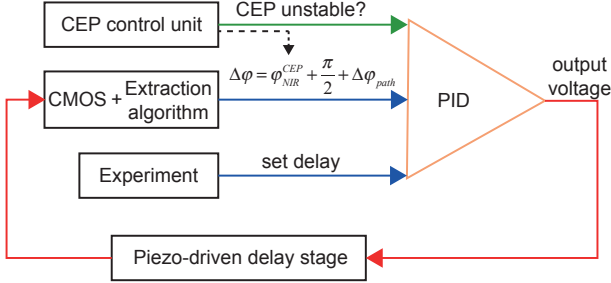


Figure 6.3: Schematic of signal processing in the active phase stabilization system. The black dashed arrow indicates that the CEP stabilization of the NIR beam affects the interference fringes observed with the CMOS camera.

6.1.5 Measurement

To demonstrate the stability as well as the importance of the active phase correction system, we performed a series of photoelectron streaking measurements. Photoelectron streaking is a commonly used technique for studying attosecond dynamics [53]. In a streaking experiment, a single attosecond pulse (SAP) ionizes a gas target (here, neon). The spectrum of the used SAP is shown in Fig. 6.4(a). The kinetic energy distribution of the electrons photo-emitted from the gas atoms corresponds to the spectrum of the SAP minus the ionization energy ($E_{Ne} = 21.56$ eV). We use a time-of-flight spectrometer to detect the electron kinetic energies. During the overlap of the XUV and OPA pulses, the energy distribution is additionally shifted by the vector potential of the OPA pulse and thus oscillates with the pump-probe delay. The oscillation frequency corresponds to the optical frequency of the OPA beam.

Figure 6.4(b) illustrates a typical streaking trace recorded around the pump-probe overlap. To the best of our knowledge, this is the first streaking demonstration involving two different IR colors for HHG and to streak the photo-emitted electrons. The red curve in Fig. 6.4(b) indicates the center of mass. Phase instabilities and temporal drifts between the pump-probe pulses are directly imprinted in a streaking trace. Consequently, this technique is a good test for the reliability of the phase stabilization system.

We recorded a set of three streaking traces measured in sequence, with an acquisition time of about 10 minutes per trace followed by a 2-3 minutes break between two consecutive runs. Figure 6.4(c) compares the center-of-mass traces extracted from the three data sets. In addition, we plot in Fig. 6.4(d) the correction applied by the stabilization system during this measurement period. The correction between the first and the last scan amounts to almost 8 fs, which is significantly more than the oscillation period at the OPA wavelength ($\tau \approx 5.2$ fs). The rms error between the set and the in-loop delay, extracted with the AIS software, amounted to about 450 as for the proof-of-principle measurement. Further, we performed an additional stability measurement, where the pump-probe delay has been kept at a fixed value for 30 min. Here, a rms value below 300 as has been extracted while the stabilization loop had to compensate for a drift on the order of 20 fs. Thus, the reported 450 as represent the in-loop delay stability achievable under dynamic operation of the system.

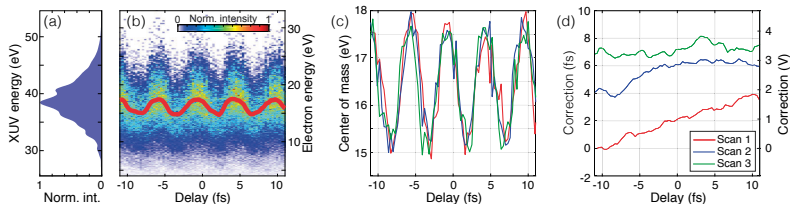


Figure 6.4: Attosecond streaking experiment as a proof-of-principle demonstration. (a) Normalized XUV spectrum of the SAP. (b) Typical streaking trace of the photo-emitted electrons recorded with a time-of-flight spectrometer. The red line marks the center of mass of the energy distribution at each pump-probe delay. (c) Extracted center-of-mass traces from three delay scans recorded in sequence. (d) Correction to the pump-probe delay applied by the stabilization system (in fs and Volt)

Our phase acquisition software could in principle also be used for only tracking the phase without providing a feedback to the piezo that controls the delay. This could potentially reduce noise contributions induced by the feedback loop. The tracked fluctuations could then be used as a correction in the post-processing of the recorded data. In our case we observed however that even after warming up the system for several hours, delay

drifts of several femtosecond per hour and thus on the order of the pump-probe overlap occur. Since a typical attosecond pump-probe experiment can take up to several hours, an active feedback is therefore preferred in our system. Furthermore, the post-correction cannot be applied if the measurement involves long exposures, i.e. if the exposure is slower than the correction frequency. In this case, the signal will be averaged over a potentially large range of relative phases and post-processing will not be able to recover delay-resolution in the pump-probe signal.

6.1.6 Conclusion

To conclude, we demonstrated active phase stabilization of an attosecond pump-probe beamline involving two IR colors. In our setup, the output of a Ti:sapphire amplifier is divided in two. One part pumps an OPA while the other one generates the attosecond XUV pulse. The signal beam from the OPA system is later recombined with the attosecond pulse to perform pump-probe measurements. The pump-probe interferometer from the first beam splitter to the recombination optics has a total arm length of about 23 m, with most of the beam path in open air.

Our system directly stabilizes the relative phase between the two colors propagating along the different interferometer arms. The direct phase sensitivity would not be possible if an auxiliary cw laser was used for the stabilization. In our approach, a fraction of the HHG driving beam is focused together with a part of the OPA beam into a BBO crystal followed by a camera. The overlapping spectral portion of the Ti:sapphire pulse and the second harmonic of the OPA is extracted with a narrow-bandwidth bandpass filter and produces an interference pattern on the camera.

With a home-built PID feedback algorithm, the interference fringes are stabilized and with it the relative phase of the involved pulses. We demonstrate delay stabilization between two IR colors to within 450 as rms. To prove the long-term sub-femtosecond stability of our system, we recorded a series of attosecond streaking traces. This experiment also illustrates that active stabilization is essential to resolve sub-femtosecond dynamics with a beamline involving two IR colors accurately. Without active stabilization, drifts of several femtosecond per hour occur.

Funding NCCR MUST, funded by the Swiss National Science Foundation (SNSF); ETH Zurich Postdoctoral Fellowship Program.

Conclusion and Outlook

In this doctoral thesis, three main projects were discussed. Chapter 4 presented a detailed study of the Gouy phase shift of a truncated beam and its influence on attosecond pump-probe measurements. In chapter 5, ATAS measurements recorded in III-V semiconductors have been discussed. Finally, chapter 6 reviewed the implementation of a tunable OPA in the laser system. In the following, the findings and results of these projects are summarized and potential future experiments are proposed.

Attosecond pump-probe beamlines commonly combine a few-cycle IR laser pulse with an attosecond XUV pulse. Due to the strong XUV absorption of most materials, the collinear recombination of the two pulses is often done geometrically with a center-hole mirror. The smaller XUV beam propagates through the hole, while the IR radiation is reflected at the mirror. This results in a donut-like shape of the reflected beam, deviating significantly from an ideal Gaussian. **Chapter 4 presented a detailed study of the Gouy phase of such an annularly truncated IR beam using the two-foci beamline [49].** By simultaneously recording RABBITT traces in the first and second focus, the IR phase across the focus could be reconstructed. While an ideal Gaussian beam experiences a phase shift of π , **the performed measurement showed a Gouy phase shift of more than 2π .** Since attosecond measurement techniques are highly phase sensitive, **the Gouy phase of the IR beam can result in a change of the extracted time information by 50 as/mm around the focus in a RABBITT measurement.** The presented findings emphasize the importance of accurate sample posi-

tioning in attosecond experiments. It is particularly important to carefully consider the Gouy phase shift in the case of spatially separated targets. The calibration of the IR Gouy phase is important for any future experiment performed with the attosecond beamline used here.

In chapter 5, ATAS measurements performed in III-V semiconductors were presented. First, the dynamics induced in GaAs by an intense resonant IR pulse were discussed. The pump pulse can induce two distinct mechanisms in the semiconductor: intraband motion and interband transitions. The relative importance of the two processes during the light-matter interaction is highly discussed. The induced carrier dynamics were probed with a SAP via core level to VB and CB transitions. We observed transient oscillations in the XUV absorption during the presence of the IR pump pulse, followed by a long-lasting signal decaying on the long ps- to ns-timescale. The focus of this thesis was on the transient signal. The period of the absorption oscillations was found to correspond to half a cycle of the IR pump-field. The experimental findings were complemented with first-principle simulations and a simplified three-level model. **This revealed that the transient modulation in the optical response in GaAs is dominated by intraband motion, contrary to the intuitive expectations [59]. In addition, the simulations showed that intraband acceleration significantly assists the injection of real carriers from the VB into the CB induced by the interband transition, even though it can itself only move carriers within a single band.** The role of the intraband transition during the injection process has been investigated in further detail for different photon energy excitation regimes [122]. The enhancement of the injection rate due to the complex interplay of the intra- and interband transitions was found to be universal.

A similar transient absorption study has been performed in $\text{Al}_{0.8}\text{Ga}_{0.2}\text{As}$. In contrast to GaAs, $\text{Al}_{0.8}\text{Ga}_{0.2}\text{As}$ has a bandgap larger than the energy of a single IR pump photon. Thus, the excitation mechanism was here non-resonant. Transient oscillations in the XUV absorption were recorded with an energy dispersion relation similar to the one observed in GaAs. **The similarity of the measured oscillation phase in GaAs and $\text{Al}_{0.8}\text{Ga}_{0.2}\text{As}$ suggests that the transient optical response is dominated by the same dynamics, namely the intraband motion.** Given the larger

bandgap, it was also expected that the interband transition plays an even less important role. Nevertheless, further calculations are required to confirm this conclusion. In particular, we suggest to perform a multi-scale simulation, which couples the ab-initio electron dynamics calculation with Maxwell's equation. Such a simulation takes the propagation of the pump and probe pulses in the condensed matter more accurately into account.

Finally, chapter 6 discussed the laser upgrade performed during the scope of this thesis. To date, most attosecond pump-probe beamlines rely on a single IR wavelength for the generation of attosecond pulses via HHG and as a pump or probe in the experiment. Recently, a setup with two distinct IR-colors involved has been presented and used to study molecular dynamics [119]. Passive delay stabilization in their system was sufficient to resolve dynamics occurring on the low femtosecond timescale. Improving the temporal resolution to the sub-femtosecond domain requires however an active pump-probe delay stabilization. **In this thesis, to the best of our knowledge, we presented the first active phase-stabilized attosecond beamline with two separate IR-colors involved** [116]. In the beamline used, the output of a Ti-sapphire power amplifier was split into two parts. One part pumped an OPA system converting the Ti-sapphire radiation to a longer wavelength. The second part was used for the generation of attosecond pulses via HHG. The OPA output and attosecond pulses were finally recombined and used for pump-probe experiments. The resulting interferometer spanned over two laboratories and had an arm length of about 23 m. A common technique to stabilize a Mach-Zehnder-like interferometer uses a co-propagating cw laser [72]. This approach was however unfeasible in the present setup due to the OPA installed in one interferometer arm. **Here, we presented a new technique to directly stabilize the relative phase of the two IR-colors propagating on the different arms to within 500 as rms, without the need for an auxiliary laser.** The long-term stability of the system has been demonstrated with photoelectron streaking spectroscopy. Without the active stabilization system running, pump-probe delay drifts of several femtoseconds per hour were observed. Since a typical attosecond experiment can take up to several hours, active stabilization is considered to be essential to study dynamics occurring on the sub-femtosecond timescale.

In recent years, transient absorption spectroscopy has proven to be a powerful tool for resolving and controlling charge carrier dynamics in metals, semiconductors and dielectrics on the attosecond timescale. Within the scope of this work the resonant excitation regime in a semiconductor material was studied for the first time. It would be highly interesting to increase the complexity of the investigated structures in future projects, e.g. to study semiconductor heterostructures, metal-semiconductor junctions, quantum wells or two-dimensional electron gases. Further, the combination of transient absorption spectroscopy with photoemission spectroscopy could reveal interesting dynamics. Since the first technique is bulk and the second one surface sensitive, they complement each other perfectly. Finally, the implemented OPA system enables a wide range of new experiments, such as the study of the wavelength-dependence of field-driven electron dynamics in solid systems, as theoretically predicted in reference [115]. Furthermore, the excitation mechanism can be switched between resonant and non-resonant by adjusting the pump wavelength. In summary, the performed studies and improved experimental setups provide a solid basis for future investigations of attosecond carrier dynamics in condensed matter.

Relation between Absorbance and Dielectric Function

In this section, the relation between the absorbance and the dielectric function is derived. In a first step, the transmission of a linearly polarized cw light field through a thin membrane with thickness L at normal incidence is calculated. The propagation direction is the x -axis. The stationary solution of Maxwell's equations for the different regions is given by

$$E_z(x, t) = \begin{cases} e^{i(k_0x - \omega t)} + r \cdot e^{i(-k_0x - \omega t)} & x < 0 \\ \alpha \cdot e^{i(\tilde{k}x - \omega t)} + \beta \cdot e^{i(-\tilde{k}x - \omega t)} & 0 \leq x \leq L \\ \gamma \cdot e^{i(k_0(x-L) - \omega t)} & x > L \end{cases} \quad (\text{A.1})$$

where $k_0 = \omega/c$ and $\tilde{k} = k_0\sqrt{\varepsilon(\omega)}$ are the wave numbers in vacuum ($\varepsilon = 1$) and the solid. ω is the frequency of the field.

With the continuity conditions of the field $E_z(x, t)$ and its derivative $\frac{\partial E_z(x, t)}{\partial x}$ at the first interface ($x = 0$), one gets

$$1 + r = \alpha + \beta \quad (\text{A.2})$$

$$k_0(1 - r) = \tilde{k}(\alpha - \beta) \quad (\text{A.3})$$

The same at the second interface ($x = L$) gives

$$\alpha e^{i\tilde{k}L} + \beta e^{-i\tilde{k}L} = \gamma \quad (\text{A.4})$$

$$\tilde{k}(\alpha e^{i\tilde{k}L} - \beta e^{-i\tilde{k}L}) = k_0\gamma \quad (\text{A.5})$$

In the following lines, these four equations are solved for γ :

Eq. (A.2)· k_0 + eq. (A.3)

$$2k_0 = (k_0 + \tilde{k})\alpha + (k_0 - \tilde{k})\beta \quad (\text{A.6})$$

Eq. (A.4)· k_0 - eq. (A.5)

$$(k_0 - \tilde{k})\alpha e^{i\tilde{k}L} + (k_0 + \tilde{k})\beta e^{-i\tilde{k}L} = 0 \quad (\text{A.7})$$

$$\Rightarrow \alpha = -\frac{(k_0 + \tilde{k})}{(k_0 - \tilde{k})} e^{-2i\tilde{k}L} \beta \quad (\text{A.8})$$

Insert eq. (A.8) in eq. (A.6)

$$2k_0 = \left[(k_0 + \tilde{k}) \left(-\frac{(k_0 + \tilde{k})}{(k_0 - \tilde{k})} e^{-2i\tilde{k}L} \right) + (k_0 - \tilde{k}) \right] \beta \quad (\text{A.9})$$

$$\Rightarrow \beta = \frac{2k_0}{\left[-(k_0 + \tilde{k}) \left(\frac{(k_0 + \tilde{k})}{(k_0 - \tilde{k})} e^{-2i\tilde{k}L} \right) + (k_0 - \tilde{k}) \right]} \quad (\text{A.10})$$

$$= \frac{2k_0(k_0 - \tilde{k})e^{i\tilde{k}L}}{\left[-(k_0 + \tilde{k})^2 e^{-i\tilde{k}L} + (k_0 - \tilde{k})^2 e^{i\tilde{k}L} \right]} \quad (\text{A.11})$$

Insert eq. (A.11) in eq. (A.8)

$$\alpha = -\frac{(k_0 + \tilde{k})}{(k_0 - \tilde{k})} e^{-2i\tilde{k}L} \frac{2k_0(k_0 - \tilde{k})e^{i\tilde{k}L}}{\left[-(k_0 + \tilde{k})^2 e^{-i\tilde{k}L} + (k_0 - \tilde{k})^2 e^{i\tilde{k}L} \right]} \quad (\text{A.12})$$

$$= -\frac{2k_0(k_0 + \tilde{k})e^{-i\tilde{k}L}}{\left[-(k_0 + \tilde{k})^2 e^{-i\tilde{k}L} + (k_0 - \tilde{k})^2 e^{i\tilde{k}L} \right]} \quad (\text{A.13})$$

Insert eq. (A.11) and (A.13) in eq. (A.4)

$$\gamma = -\frac{2k_0(k_0 + \tilde{k})}{\left[-(k_0 + \tilde{k})^2 e^{-i\tilde{k}L} + (k_0 - \tilde{k})^2 e^{i\tilde{k}L} \right]} + \frac{2k_0(k_0 - \tilde{k})}{\left[-(k_0 + \tilde{k})^2 e^{-i\tilde{k}L} + (k_0 - \tilde{k})^2 e^{i\tilde{k}L} \right]} \quad (\text{A.14})$$

$$\Rightarrow \gamma = - \frac{4k_0\tilde{k}}{\left[-(k_0 + \tilde{k})^2 e^{-i\tilde{k}L} + (k_0 - \tilde{k})^2 e^{i\tilde{k}L} \right]} \quad (\text{A.15})$$

Expand the exponential functions in the denominator of eq. (A.15)

$$\gamma = - \frac{4k_0\tilde{k}}{\left[-(k_0^2 + 2k_0\tilde{k} + \tilde{k}^2)(\cos(\tilde{k}L) - i \cdot \sin(\tilde{k}L)) + (k_0^2 - 2k_0\tilde{k} + \tilde{k}^2)(\cos(\tilde{k}L) + i \cdot \sin(\tilde{k}L)) \right]} \quad (\text{A.16})$$

$$= \frac{2k_0\tilde{k}}{2k_0\tilde{k}\cos(\tilde{k}L) - i(k_0^2 + \tilde{k}^2)\sin(\tilde{k}L)} \quad (\text{A.17})$$

Therefore, the transmission through the film is

$$T = |\gamma|^2 = \left| \frac{2k_0\tilde{k}}{2k_0\tilde{k}\cos(\tilde{k}L) - i(k_0^2 + \tilde{k}^2)\sin(\tilde{k}L)} \right|^2 \quad (\text{A.18})$$

and the absorbance $Abs(\omega)$ becomes (see eq. (2.9))

$$Abs(\omega) = -\ln(T) = -\ln \left| \frac{2k_0\tilde{k}}{2k_0\tilde{k}\cos(\tilde{k}L) - i(k_0^2 + \tilde{k}^2)\sin(\tilde{k}L)} \right|^2 \quad (\text{A.19})$$

Please note that $Abs(\omega)$ is energy dependent due to the energy-dependence of $\tilde{k} = k_0\sqrt{\varepsilon(\omega)}$.

Equations (A.18) and (A.19) are the equations (5.4) and (5.5) given in chapter 5. In the following, the relation between the change in absorbance, $\Delta Abs(\omega)$, and the change in the imaginary part of the dielectric function, $Im(\Delta\varepsilon(\omega))$, is derived. We write \tilde{k} as

$$\tilde{k} = k_0\sqrt{\varepsilon} = k_0Re[\sqrt{\varepsilon}] + ik_0Im[\sqrt{\varepsilon}] \quad (\text{A.20})$$

For sufficient large L , equation (A.15) can be approximated as

$$\gamma = - \frac{4k_0\tilde{k}}{\left[-(k_0 + \tilde{k})^2 e^{-ik_0Re[\sqrt{\varepsilon}]L + k_0Im[\sqrt{\varepsilon}]L} + (k_0 - \tilde{k})^2 e^{ik_0Re[\sqrt{\varepsilon}]L - k_0Im[\sqrt{\varepsilon}]L} \right]} \quad (\text{A.21})$$

$$\gamma \approx \frac{4k_0\tilde{k}}{(k_0 + \tilde{k})^2 \cdot e^{-ik_0Re[\sqrt{\varepsilon}]L} \cdot e^{k_0Im[\sqrt{\varepsilon}]L}} \quad (\text{A.22})$$

For the transmission, one gets

$$T \approx \left| \frac{4k_0\tilde{k}}{(k_0 + \tilde{k})^2} \right|^2 \cdot e^{-2k_0\text{Im}[\sqrt{\tilde{\epsilon}}]L} \quad (\text{A.23})$$

$$= \left| \frac{4k_0^2\sqrt{\tilde{\epsilon}}}{k_0^2(1 + \sqrt{\tilde{\epsilon}})^2} \right|^2 \cdot e^{-2k_0\text{Im}[\sqrt{\tilde{\epsilon}}]L} \quad (\text{A.24})$$

$$= \left| \frac{(1 + \sqrt{\tilde{\epsilon}})^2 - (1 - \sqrt{\tilde{\epsilon}})^2}{(1 + \sqrt{\tilde{\epsilon}})^2} \right|^2 \cdot e^{-2k_0\text{Im}[\sqrt{\tilde{\epsilon}}]L} \quad (\text{A.25})$$

$$= \left| 1 - \frac{(1 - \sqrt{\tilde{\epsilon}})^2}{(1 + \sqrt{\tilde{\epsilon}})^2} \right|^2 \cdot e^{-2k_0\text{Im}[\sqrt{\tilde{\epsilon}}]L} \quad (\text{A.26})$$

The transmission described by equation (A.26) can be divided into two parts. The first factor describes the reduction of the transmission due to the reflection on the front and rear surface of the membrane:

$$\left| 1 - \frac{(1 - \sqrt{\tilde{\epsilon}})^2}{(1 + \sqrt{\tilde{\epsilon}})^2} \right|^2 = |1 - R|^2 = (1 - R) \cdot (1 - R) \quad (\text{A.27})$$

where R is the reflectivity.

The second factor, $e^{-2k_0\text{Im}[\sqrt{\tilde{\epsilon}}]L}$, describes the absorption. For sufficiently large L , the transmission T is dominated by the second factor and therefore by absorption. In the following, we only consider the second dominating factor.

Finally, we look at the induced change of absorbance due to an IR pump. The perturbation results in a modification of the dielectric function, $\epsilon \rightarrow \epsilon + \Delta\epsilon$, and therefore also of the transmission. The relation between the change in absorbance and transmission with and without the IR pulse has been derived in section 2.3 (see eq. 2.10):

$$\Delta Abs = \ln\left(\frac{T_{without IR}}{T_{with IR}}\right) \quad (\text{A.28})$$

By inserting the dominating factor of equation (A.26) into equation (A.28) and Taylor expanding the square root of the dielectric function,

one gets

$$\Delta Abs = \ln \left(\frac{e^{-2k_0 \text{Im}[\sqrt{\varepsilon}]L}}{e^{-2k_0 \text{Im}[\sqrt{\varepsilon+\Delta\varepsilon}]L}} \right) \quad (\text{A.29})$$

$$= \ln \left(e^{-2k_0 \text{Im}[\sqrt{\varepsilon}-\sqrt{\varepsilon+\Delta\varepsilon}]L} \right) \quad (\text{A.30})$$

$$\approx \ln \left(e^{-2k_0 \text{Im}[\sqrt{\varepsilon}-(\sqrt{\varepsilon}+\frac{1}{2}\frac{\Delta\varepsilon}{\sqrt{\varepsilon}})]L} \right) \quad (\text{A.31})$$

$$= \ln \left(e^{k_0 \text{Im}[\frac{\Delta\varepsilon}{\sqrt{\varepsilon}}]L} \right) \quad (\text{A.32})$$

$$= k_0 \text{Im}[\frac{\Delta\varepsilon}{\sqrt{\varepsilon}}]L \quad (\text{A.33})$$

$\sqrt{\varepsilon}$ can be replaced by the complex index of refraction as

$$\sqrt{\varepsilon} = n + i\kappa \quad (\text{A.34})$$

In the XUV regime of the attosecond radiation, we can assume $n \approx 1$ and κ to be small ($\kappa \ll n$). With these approximations, equation (A.33) simplifies to

$$\boxed{\Delta Abs = \frac{k_0 L}{n} \text{Im}[\Delta\varepsilon] \propto \text{Im}[\Delta\varepsilon]} \quad (\text{A.35})$$

Hence, the IR-induced change in absorbance is proportional to the change in the imaginary part of the dielectric function.

**Supplementary Information:
Attosecond Optical-Field-Enhanced Carrier
Injection into the GaAs Conduction Band**

This appendix contains the Supplementary Information of the publication listed below. The corresponding paper is printed in section 5.4. The text and figures are as in the post-print version of the publication. Only the style of the text, figures and equations has been adapted to the style of the thesis. Further, the numbering of the figures and references has been adjusted. The reference list of the publication has been included in the reference list of the thesis. Sections S1.1 and S1.2 of the published Supplementary Information are already discussed elsewhere in this thesis and therefore not printed here.

Title: "Attosecond optical-field-enhanced carrier injection into the GaAs conduction band", [59]

Journal: *Nature Physics*

doi: 10.1038/s41567-018-0069-0

URL: <https://doi.org/10.1038/s41567-018-0069-0>

Published: 12th March 2018

©2018, Springer Nature.

B.1 Experimental Methods

B.1.1 Sample Properties and Preparation

The sample measured here is a freestanding single-crystalline GaAs membrane with a thickness of 100 nm. The illuminated top surface is the (100) plane. The linear pump and probe polarizations point both along the (011) crystal orientation, which means that we probe along the Σ -symmetry line in the reciprocal space. The fabrication process of the nanomembrane involves a combination of mechanical polishing and chemical wet etching of a semiconductor heterostructure grown by molecular beam epitaxy (MBE) [73,74]. Both, growth and etching, were done in the clean room facility FIRST at ETH Zurich. The clear aperture of the membrane is around 0.4×0.6 mm. Due to the growth by MBE, we assume a uniform thickness and quality over the whole membrane. Nevertheless, the measurements have been repeated on different spots on two different samples to test the reproducibility of the experiment.

B.1.2 Infrared Pulse Parameters

Table B.1 summarizes the parameters of the IR-pump pulse used for the measurement. A spectrum of the pulse is shown in Fig. 5.2 of the main manuscript. One can see that the pump is clearly in resonance with the bandgap of GaAs, which is at room temperature approximately 1.42 eV [105]. The IR peak intensity and electric field strength have been estimated from the spatial and temporal profiles. These profiles have been obtained with a beam profiler camera and streaking measurements, respectively. Breakdown (laser induced damage) of the GaAs membrane was observed at a pulse energy of around $2.25 \mu\text{J}$ (corresponding to a peak intensity of approximately $2.6 \times 10^{12} \text{ W/cm}^2$). The IR intensity inside the sample has been computed taking into account the dielectric function of GaAs [123] and the stationary solution of Maxwell's equations. The result gives a maximum intensity that changes along the beam propagation direction inside the sample and peaks at approximately 60% of the incident intensity. Therefore, the peak intensity of the pump inside the membrane is up to $\approx 1.39 \times 10^{12} \text{ W/cm}^2$ and the peak electric field strength up to $\approx 0.32 \text{ V/\AA}$. Figure B.1 shows the laser intensity dependence of the num-

ber of injected carriers from the VB into the CB computed by the first-principles calculation (see section B.2). While the carrier population is proportional to the laser intensity in the weak intensity region, it shows a nonlinear response in the high intensity region. This result indicates that the injection mechanism in the current experiment is in the non-linear regime.

Energy	$\sim 2 \mu\text{J}$
Pulse duration (FWHM)	$5.45 \pm 0.71 \text{ fs}$
Beam waist	$\sim 74.4 \mu\text{m}$
Peak intensity	$(2.31 \pm 0.17) \times 10^{12} \text{ W/cm}^2$
Peak electric field strength	$0.42 \pm 0.02 \text{ V/\AA}$

Table B.1: Laser parameters of the infrared pulse in vacuum. The intensity inside the membrane is up to 60% compared to the vacuum.

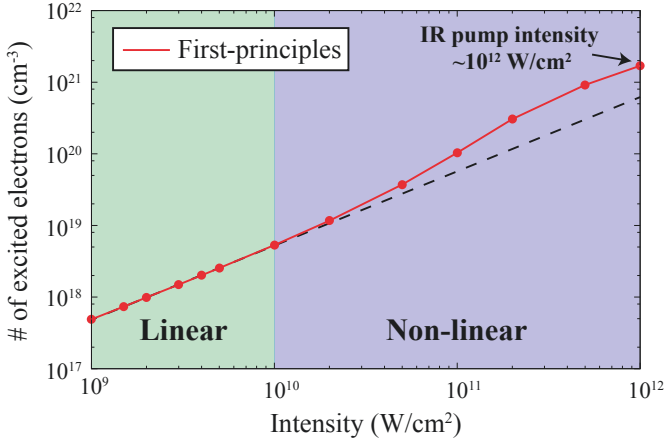


Figure B.1: Injected carrier population vs. laser intensity. For low pump intensities, a first-principles calculation predicts a linear relation between the number of carrier excited from the VB into the CB and the pump intensity. For intensities exceeding 10^{10} W/cm^2 , the number of carriers deviates from the linear relation (black dashed line). Hence, in the current experiment with a pump intensity of $\sim 10^{12} \text{ W/cm}^2$, the carrier injection mechanism is in the non-linear regime.

B.1.3 Single Attosecond Pulse (SAP) vs. Attosecond Pulse Train (APT)

The ATAS measurements shown in Fig. 5.3 of the main manuscript are measured with single attosecond pulses (SAPs). The temporal characterization of the SAP is obtained with the FROG-CRAB technique using the ePIE [58]. In Fig. B.2, a typical energy spectrum of a SAP together with its temporal reconstruction is shown. The pulse duration is approximately 200 as.

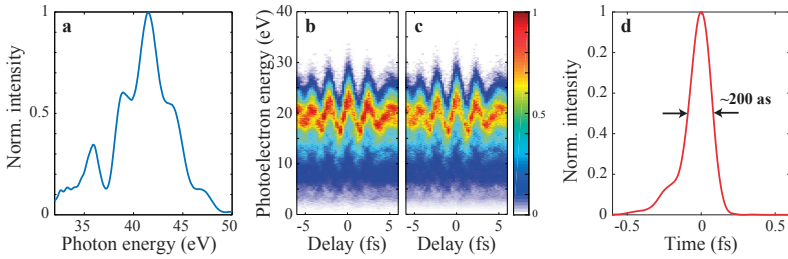


Figure B.2: Single attosecond pulse (SAP) reconstruction. (a) XUV spectrum. (b) Measured streaking trace. (c) Reconstructed streaking trace. (d) Reconstructed SAP.

One advantage of using a SAP in the current experiment is the broad continuous spectrum, which makes it possible to study electron dynamics in the valence (VB) and conduction band (CB) at the same time. Compared to an APT however, SAPs are characterized by a lower photon flux and thus higher spectral noise. Due to the use of the PG technique, the SAPs used in our experiment are characterized by a strong dependence of the spectral amplitude around 40 eV on the carrier-envelope offset phase (CEP) of the driving pulses. Even if the CEP was actively stabilized to a *rms* value of < 0.15 rad during the measurements, we were unable to resolve the characteristic oscillations in the transient absorption signal from the VB (in contrast to those at the higher photon energies probing the CB). Figure B.3 shows a measurement with an APT, whose spectral amplitude does not depend on the IR CEP value. Here, $2\omega_{IR}$ -oscillations are clearly visible both in the VB and in the CB (40.4 eV and 43.6 eV, respectively).

This confirms the theoretical predictions reported in Fig. 5.3(c) of the main manuscript.

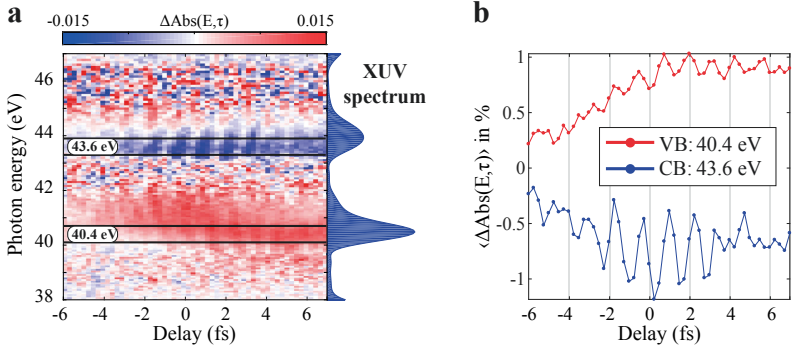


Figure B.3: Attosecond transient absorption spectroscopy (ATAS) measurement performed with an attosecond pulse train (APT). (a) ATAS trace with the corresponding XUV spectrum. (b) Energy averaged signal in the valence band (VB) (40.4 eV, red) and conduction band (CB) region (43.6 eV, blue). The integration intervals are shown in (a) with the black solid lines. The absorption change at 40.4 eV confirms the presence of $2\omega_{IR}$ -oscillations also in the VB signal below 42 eV.

B.1.4 Pump-Probe Delay Calibration

A precise pump-probe delay calibration is crucial for a comparison of the absolute phases of the absorption oscillations as discussed in Fig. 5.4(f) of the main manuscript. Figure B.4(a) shows a typical streaking trace measured simultaneously with an ATAS trace. The negative vector potential $-A(t)$ of the IR pulse follows approximately the center of mass (CM) of the streaking signal. In Fig. B.4(b), $A(t)^2$ is plotted together with the following fit function:

$$F(t) = \left((a \cdot \cos(b \cdot (t - c) + d) \cdot \exp\left(-\frac{(t - c)^2}{2e^2}\right)) + f \right)^2, \quad (\text{B.1})$$

where a , b , c , d , e and f are fitting parameters. We define delay zero as the local maximum closest to the maximum of the envelope.

For the calibration of the timing between the pump and probe pulse, we take into account the following two issues:

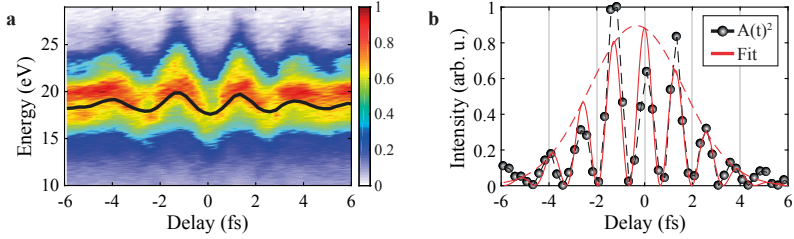


Figure B.4: Delay calibration. (a) Typical streaking trace measured simultaneously with the ATAS trace. The temporal shape of the vector potential $A(t)$ follows the center of mass (black solid curve), but with opposite sign. (b) The black circles show the square of the extracted vector potential, $A(t)^2$, as extracted from (a). The amplitude mismatch between the experimental data and fit can be explained by the asymmetry in the streaking trace. Delay zero is defined as the local maximum of the fit (red line) being closest to the maximum of the envelope (red dashed line).

(1) *Spatial separation between the streaking and ATAS target*

In a recent publication, we demonstrated that the Gouy phase shift of the IR beam has a non-negligible influence onto attosecond pump-probe measurements with spatially separated targets [49]. In particular, for our focusing condition we found that the Gouy phase results in a phase shift for the IR beam of around minus 25 as/mm around the focus. In the experiment here, the spacing between the gas nozzle and GaAs membrane is 1.35 mm. Consequently, the IR electric field experiences a phase shift of minus ≈ 34 as while it propagates from the neon target to the GaAs membrane target.

(2) *Effect of the cross-section and atomic delay in the streaking reconstruction*

Above, we extracted the IR vector potential directly from the center of mass (CM) of the streaking without any reconstruction algorithm. Hence, the cross-section and atomic delay of the target gas are not taken into account. To estimate the error induced by this, we performed a simulation of a streaking trace and compared the input IR field $E_{in}(t)$ with the reconstructed field defined as $E_{rec}(t) \propto -\partial CM/\partial t$. Including both the cross-section and atomic delay in the simulation results in a temporal offset between $E_{in}(t)$ and $E_{rec}(t)$ of ≈ 30 as. Hence, the reconstructed field defined as $E_{rec}(t) \propto -\partial CM/\partial t$ has to be shifted by 30 as to positive delays to get the proper input field $E_{in}(t)$.

Both time shifts discussed above give a comparable but opposite shift to the IR pump field and therefore they practically cancel out. Therefore, in our analysis we took directly the CM extracted from the streaking trace without applying any further correction to reconstruct the IR vector potential ($A(t) \propto -CM$).

B.1.5 Phase and Delay Extraction

As discussed in the main manuscript, the phase of the absorption oscillations in the measured and simulated ATAS traces depends strongly on the photon energy E of the XUV pump pulse, which results in the tilted features in the signal. We extract the phase and delay between the squared vector potential of the IR pulse ($S_1(t) = A(t)^2$) and the ATAS oscillation ($S_2(E, t) = ATAS(E, t)$) for each XUV photon energy by looking at the following product, as in Ref. [49]:

$$C(E, \omega) = \tilde{S}_1(\omega) \cdot \tilde{S}_2(E, \omega)^*, \quad (\text{B.2})$$

where $\tilde{S}_1(\omega)$ is the Fourier transform of $S_1(t)$ and $\tilde{S}_2(E, \omega)^*$ is the complex conjugate of the Fourier transform of $S_2(E, t)$. $|C(E, \omega)|$ has a peak at the shared oscillation frequency of the two signals, which is equal to twice the IR frequency (Fig. B.5). The phase of C , instead, gives the phase difference between S_1 and S_2 , $\Delta\Phi(E, \omega)$. Hence, the relative phase offset between local maxima of the squared vector potential and the maxima of the induced absorption modulation is extracted without any time-zero calibration. This avoids introducing an uncertainty in the phase difference through an uncertainty in the delay calibration. Finally, the energy dependence of the delay between the squared IR vector potential and the ATAS oscillations can be calculated as:

$$\langle \tau(E) \rangle = \frac{\int I(E, \omega) \cdot \frac{\Delta\Phi(E, \omega)}{\omega} d\omega}{\int I(E, \omega) d\omega}, \quad (\text{B.3})$$

$$\sigma_{\langle \tau \rangle}^2(E) = \frac{\int I(E, \omega) \cdot \left[\frac{\Delta\Phi(E, \omega)}{\omega} - \langle \tau(E) \rangle \right]^2 d\omega}{\int I(E, \omega) d\omega}. \quad (\text{B.4})$$

Here, $I(E, \omega)$ is a weighting function, equal to a Gaussian fit of $|C(E, \omega)|$ within its full-width-at-half-maximum around the peak (Fig. B.5). Equa-

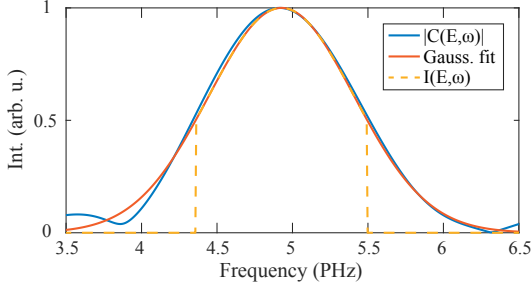


Figure B.5: Phase and delay extraction. The blue curve illustrates $|C(E, \omega)|$ extracted from a simultaneously recorded streaking and ATAS trace ($E = 46.6$ eV). $|C(E, \omega)|$ has a peak at the common oscillation frequency of the squared IR field and ATAS trace ($\omega_{peak} \approx 2\omega_{IR}$). The red curve is a Gaussian fit of $|C(E, \omega)|$. The weighting function $I(E, \omega)$ used in Eqs. (B.3) and (B.4) is equal to the Gaussian fit within its FWHM window (yellow curve).

tions (B.3) and (B.4) represent the delay and second momentum extracted from a single measurement/simulation.

The experimental delay in Fig. 5.4 of the main manuscript shows the statistical average of nine measurements recorded on four different days. The average experimental delay is calculated as follows:

$$\tau_{avg}(E) = \frac{\sum_{i=1}^N \sigma_{\langle \tau_i \rangle}^{-2}(E) \cdot \langle \tau_i(E) \rangle}{\sum_{i=1}^N \sigma_{\langle \tau_i \rangle}^{-2}(E)}, \quad (\text{B.5})$$

where $\langle \tau_i(E) \rangle$ and $\sigma_{\langle \tau_i \rangle}(E)$ represents the delay and uncertainty of the individual measurements and N the number of measurements. The error bar of the presented experimental delay is:

$$\delta\tau_{avg}(E) = \sqrt{\frac{N}{N-1} \frac{\sum_{i=1}^N \sigma_{\langle \tau_i \rangle}^{-2}(E) \cdot |\langle \tau_i(E) \rangle - \tau_{avg}(E)|^2}{\sum_{i=1}^N \sigma_{\langle \tau_i \rangle}^{-2}(E)} + \left(\frac{\sum_{i=1}^N \sigma_{\langle \tau_i \rangle}^{-1}(E)}{\sum_{i=1}^N \sigma_{\langle \tau_i \rangle}^{-2}(E)} \right)^2}. \quad (\text{B.6})$$

The first term in the square root is the weighted variance of the nine individual delays $\langle \tau_i(E) \rangle$ with respect to $\tau_{avg}(E)$. The second term is the weighted mean of the individual uncertainties $\sigma_{\langle \tau_i \rangle}(E)$.

B.2 Theoretical Methods

In order to gain insights into the underlying physical dynamics for the observed features in the experiment, we employ two different theoretical models: (1) An *ab-initio* model based on first-principles density functional calculations and (2) a simplified three-band model. In this section, we briefly introduce both models and explain the simulation results.

B.2.1 First-Principles Electron Dynamics Simulation in the Time-Domain

To simulate the optical response of GaAs from first-principles, we solve the following one-body Schrödinger equation in the time-domain,

$$i\hbar \frac{\partial}{\partial t} u_{bk}(\mathbf{r}, t) = \left[\frac{1}{2m} \left\{ \mathbf{p} + \hbar \mathbf{k} + \frac{e}{c} \mathbf{A}(t) \right\}^2 + v(\mathbf{r}) \right] u_{bk}(\mathbf{r}, t), \quad (\text{B.7})$$

where $u_{bk}(\mathbf{r}, t)$ describes the Bloch orbital with the band index b and crystal momentum $\hbar \mathbf{k}$. The one-body potential $v(\mathbf{r})$ is approximated by the Kohn-Sham potential in the static density functional theory (DFT). Thus, equation (B.7) is nothing but the time-dependent Kohn-Sham equation of the time-dependent density functional theory (TDDFT) [124] with frozen Hartree and exchange-correlation potentials.

In more detail, we perform a DFT calculation with a pseudopotential-based real-space TDDFT code (*Ab-initio* Real-Time Electron Dynamics simulator; ARTED [125]) to construct the one-body potential $v(\mathbf{r})$. We treat $3d$, $4s$, and $4p$ electrons of the Ga and As atoms as valence electrons. The exchange-correlation potential in the DFT calculation is given by a meta-GGA potential [126] with an optimized mixing-parameter, c , to reproduce the band-gap of GaAs at zero Kelvin [127]. In the experiment, the GaAs membrane is at room temperature and has therefore a reduced bandgap due to phononic effects. In the simulations however, we completely freeze the ions. Thus, to keep the treatment for electrons and phonons consistent, we consider the zero-temperature properties in the simulations for both.

Based on the above *ab-initio* modeling, we perform pump-probe simulations [101] and compute the transient modification of the imaginary part of the dielectric function, $\text{Im}(\Delta\epsilon)$, which is directly related to a change in the

absorption [22]. We use a pump pulse with a peak electric field strength of 2.75×10^9 V/m, a mean frequency of 1.55 eV/ \hbar and a pulse width of about 5 fs. For the probe pulse, we set the peak field strength to 2.75×10^8 V/m, the mean frequency to 40 eV/ \hbar and the pulse duration to 250 as.

For the simulations in this paper, we employ a primitive unit cell of GaAs, which consists of a single Ga and As pair. We discretize the Brillouin zone into 12^3 k -points. As in the experimental setup, the polarization of the pump and probe pulses are along the (011) crystal orientation. To numerically solve equation (B.7) in the time-domain, we employ a basis expansion method with eigenstates of the static Kohn-Sham Hamiltonian using the momentum-shift technique [128].

As mentioned in the main manuscript, we applied an energy shift of 4.23 eV to the first-principles results. The reason for this shift is due to the fact that the TDDFT calculation underestimates the energy gap between the core level and the top of the valence band. In our specific case, the simulated transition energy is 36.5 eV instead of 40.73 eV [95]. We corrected for this underestimation by shifting the absorption signal by 4.23 eV.

B.2.2 Role of the Propagation Effect

The frequency dependence of the refractive index of GaAs results in a different propagation speed of the IR-pump and XUV-probe pulse. The phase velocity of the IR pulse is about $v_{IR} = c/n_{IR} \approx c/3.7$ [123], where c describes the speed of light in vacuum. For a 100-nm thick GaAs membrane, the resulting propagation time for the pump pulse is about 1.233 fs. By assuming that the group velocity of the XUV pulse inside the bulk does not change much compared to the vacuum, the travel time of the probe is about 0.333 fs. Two pulses with an initial delay of zero femtosecond are therefore temporally separated by 900 as after the GaAs membrane. Consequently, the ATAS signal measured for a certain delay τ is actually a signal averaged over pump-probe delays between $t = \tau$ and $t = \tau - 900$ as. The minus sign results from the delay definition used.

In the simulations, this propagation effect is not directly included. In

order to take it into account, the theoretical signal has to be averaged by

$$\Delta\tilde{\epsilon}(E, \tau) = \frac{1}{\Delta T} \int_{\tau-\Delta T}^{\tau} \Delta\epsilon(E, t) dt, \quad (\text{B.8})$$

with ΔT equal to 900 as. $\Delta\epsilon(E, t)$ is the change of the dielectric function simulated with the *ab-initio* and three-band models, respectively. As illustrated in Fig. B.6, the averaging has an important effect onto the signal. With neglected propagation, the offset between the experimental and the simulated trace is approximately 600 as. Taking the propagation into account results in a reduced phase offset of below 250 as. The residual offset between the experiment and simulation might result from the longitudinal dependence of the non-uniform IR field distribution in the bulk material. As described above, we include the macroscopic propagation in a simplified way by averaging the signal (Eq. (B.8)). It is however important to note that taking propagation into account results mainly in a shift of the energy dispersion shown in Fig. 5.4(f) of the main manuscript along the delay axis without any significant change to its shape. All simulations shown in the main manuscript take the propagation effects according to equation (B.8) into account.

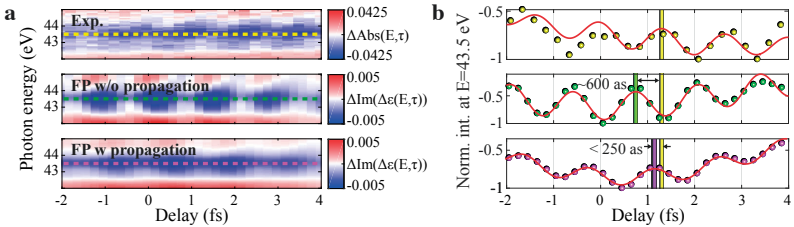


Figure B.6: Propagation effect. (a) Comparison of the experimental signal (upper) with the first-principles simulation without (middle) and with (lower) propagation included. (b) Energy averaged signal around 43.5 eV for the three traces in (a) (integration width of 0.2 eV). The vertical lines compare the individual peak positions. As we can see, taking the propagation into account results in a significant reduction of the phase offset between the experiment and simulation.

B.2.3 Pump Intensity Dependence

Studying the dependence of the ATAS signal on varying IR pump intensity experimentally is challenging. Reducing the pump intensity results in a significantly weaker signal and is limited by the achievable signal-to-noise ratio. Increasing it leads to irreversible damage of the membrane. The experimental traces presented in the main manuscript are recorded with an IR pump intensity close to the damage threshold of the GaAs target.

Nevertheless, to study the intensity-scaling of the signal, we performed first-principles simulations with varying IR-pump intensity. First, we computed the number of carriers injected by the pump (see section B.1.2). Figure B.1 shows the carrier population as a function of the laser intensity. One can clearly see the nonlinearity of the carrier injection mechanism. Second, we performed simulations of the transient absorption with different pump intensities. Figure B.7 shows two example traces for $5 \times 10^{11} \text{ W/cm}^2$ and $1 \times 10^{12} \text{ W/cm}^2$. Reducing the pump intensity results in a smaller absorption change. However, the shape is preserved. This fact indicates that the modification of the optical properties has a linear dependence on the laser intensity, while the carrier injection mechanism has a nonlinear dependence. This is consistent with our finding that the transient modification of the optical property is dominated by the virtual carrier effect of the intra-band transition, which scales linearly, while the carrier-injection is enhanced by the coupling of the intra- and inter-band transition, which scales nonlinearly.

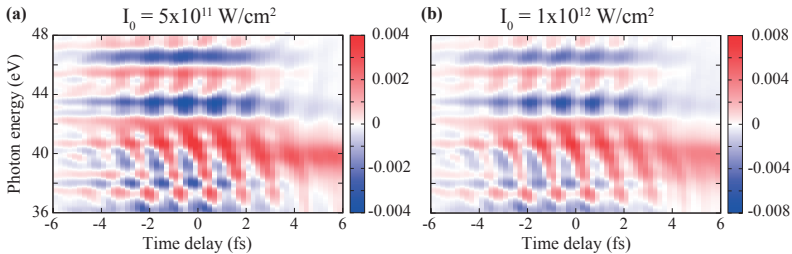


Figure B.7: First-principles simulation of absorption modulation for two IR pump intensities. (a) $5 \times 10^{11} \text{ W/cm}^2$. (b) $1 \times 10^{12} \text{ W/cm}^2$.

B.2.4 Probe-Decomposition based on Houston States

The first-principles calculations with the propagation effects reproduce the experimental result very well. In order to clarify the microscopic origin of the signal, it is helpful to apply a probe-decomposition based on Houston states [22].

For the decomposition, we first consider a decomposition of the full Hamiltonian into the pump and the probe part: $\hat{H}_{pump-probe} = \hat{H}_{pump} + \hat{H}_{probe}$. $\hat{H}_{pump-probe}$ is the one-body Hamiltonian in equation (B.7), while \hat{H}_{pump} is the Hamiltonian only including the pump pulse. The probe part, \hat{H}_{probe} , is defined by the difference of $\hat{H}_{pump-probe}$ and \hat{H}_{pump} .

Next, we consider the matrix representation of the probe Hamiltonian based on the instantaneous eigenstates $u_{bk}^P(\mathbf{r}, t)$ of the pump Hamiltonian, also known as Houston states [107, 129],

$$\left[\frac{1}{2m} \left\{ \mathbf{p} + \hbar \mathbf{k} + \frac{e}{c} \mathbf{A}_{pump}(t) \right\}^2 + v(\mathbf{r}) \right] u_{bk}^P(\mathbf{r}, t) = \varepsilon_{bk + \frac{e}{\hbar c} \mathbf{A}_{pump}(t)} u_{bk}^P(\mathbf{r}, t). \quad (\text{B.9})$$

Finally, by partially including/omitting the matrix elements of the probe Hamiltonian in the simulation, we can investigate dynamics induced by a specific probe transition. It is important to note that the pump mechanism is not influenced by the probe decomposition discussed here. Only the probe transitions between different energy levels are modified.

Figure B.8 illustrates the probe decomposition of the first-principles simulation. As we can see, the full signal (Fig. B.8(a)) is almost perfectly reproduced by the decomposed signal when including only the probe transition from the As-3*d* core level to the VB and CB (Fig. B.8(b)). The transient signal in this energy regime is therefore dominated by probe transitions involving the As-3*d* core level as expected.

For a more detailed understanding, we further decompose the first-principles signal into the CB (Fig. B.8(c)) and the VB response (Fig. B.8(d)). In these cases, only probe transitions from the core level to either the CB or VB are allowed. One can see that the transient features in the absorption around 43 eV come mainly from probe transition between the As-3*d* level

and the CB. Based on this, we focus on the CB response in the following analysis using the three-band model.

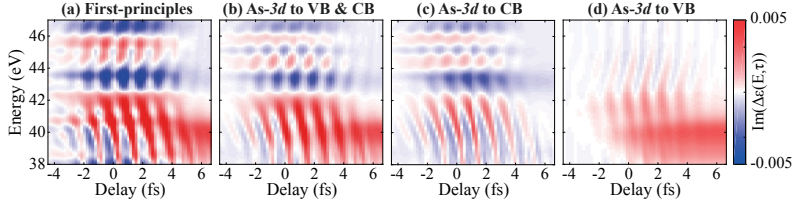


Figure B.8: Decomposition of the first-principles signal. (a) Full signal without any decomposition. (b) Decomposed signal with probe transitions from As-3d bands to valence and conduction bands, (c) from As-3d to only conduction bands (CB response), and (d) from As-3d to only valence bands (VB response).

B.2.5 Simplified 3-Band Model

To investigate the role of *intra*- and *inter*-band transitions in the transient response of GaAs, we employ a simple model consisting of only three bands: A flat band, which mimics the As-3d core level, and two parabolic bands representing the VB and CB. We set the energy level of the As-3d band to -40.73 eV with respect to the VB edge [95]. The band gap is $\varepsilon_{gap} = 1.52$ eV, which is equal to the band gap of GaAs at zero Kelvin [105]. The shape of the parabolic bands is given by the corresponding effective electron masses ($m_{CB} = 0.067 m_e$ [105], $m_{lh,VB} = 0.08 m_e$ [130]). For the VB, we choose the light-hole mass rather than the heavy-hole mass, as the simulation with this choice reproduces the experiment better (see Section B.2.5.2).

Based on the above assumptions, one can consider the following Houston expansion [129] with three instantaneous eigenstates of the time-dependent Hamiltonian for each crystal momentum,

$$u_{\mathbf{k}}(\mathbf{r}, t) = c_{dk}(t)u_{dk}^H(\mathbf{r}, t) + c_{vk}(t)u_{vk}^H(\mathbf{r}, t) + c_{ck}(t)u_{ck}^H(\mathbf{r}, t), \quad (\text{B.10})$$

where $u_{dk}^H(\mathbf{r}, t)$, $u_{vk}^H(\mathbf{r}, t)$ and $u_{ck}^H(\mathbf{r}, t)$ are the instantaneous eigenstates of the As-3d level, VB and CB, respectively. The dynamics of the three-band model is described by the following Schrödinger equation for the time-

dependent coefficients:

$$i\hbar \frac{\partial}{\partial t} \begin{pmatrix} c_{dk}(t) \\ c_{vk}(t) \\ c_{ck}(t) \end{pmatrix} = \begin{pmatrix} \varepsilon_d & h_{dv,\mathbf{K}(t)} & h_{dc,\mathbf{K}(t)} \\ h_{dv,\mathbf{K}(t)}^* & \varepsilon_{v,\mathbf{K}(t)} & h_{vc,\mathbf{K}(t)} \\ h_{dc,\mathbf{K}(t)}^* & h_{vc,\mathbf{K}(t)}^* & \varepsilon_{c,\mathbf{K}(t)} \end{pmatrix} \cdot \begin{pmatrix} c_{dk}(t) \\ c_{vk}(t) \\ c_{ck}(t) \end{pmatrix}, \quad (\text{B.11})$$

where the crystal momentum $\hbar\mathbf{K}(t)$ is shifted by the vector field, $\hbar\mathbf{K}(t) = \hbar\mathbf{k} + \mathbf{A}(t)/c$. The matrix elements are defined as:

$$\varepsilon_{v,\mathbf{K}(t)} = -\frac{\mathbf{K}(t)^2}{2m_{lh,VB}}, \quad \varepsilon_{c,\mathbf{K}(t)} = \varepsilon_{gap} + \frac{\mathbf{K}(t)^2}{2m_{CB}}, \quad \varepsilon_d = -40.73 \text{ eV}, \quad (\text{B.12})$$

$$h_{ij,\mathbf{K}(t)} = -ip_{ij} \cdot \frac{E(t)}{(\varepsilon_{i,\mathbf{K}(t)} - \varepsilon_{j,\mathbf{K}(t)})}. \quad (\text{B.13})$$

The diagonal elements of the 3x3 matrix describe the electronic structure of the three-band model with the energy levels and effective masses introduced above. The off-diagonal elements are defined by the corresponding momentum matrix elements, p_{ij} . To investigate the probe-induced transition from the semi-core to the CB in the main manuscript (CB response), we set p_{dv} to zero. Here, we note that the momentum matrix element between the As-3d band and the CB, p_{dc} , does not have any effect on the structure of the induced signal since there is no nonlinear effect from the semi-core transition at the present laser intensity. It only affects the absolute value of the signal.

In order to further construct the model, we need to define the momentum matrix element between the VB and CB, p_{vc} . For this purpose, we compute the signal with the three-band model for different values of the matrix element. Figure B.9 compares the corresponding energy-averaged signals (integration interval: 42.5 to 43.0 eV) with the *ab-initio* simulation. The black-solid line follows the signal extracted from the first-principles calculation. The other lines show the signals of the three-band model for different values of the matrix element. As seen from the figure, a squared matrix element p_{vc}^2 of 0.02 a.u. reproduces the first-principles simulation best, especially the ratio of the transient and long-lasting signal. Therefore, we chose this value for the three-band model simulations shown in the main manuscript.

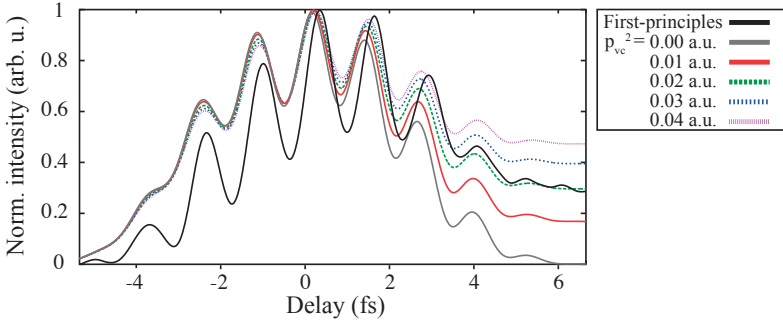


Figure B.9: Extraction of matrix element p_{vc} . Here, the energy-averaged signals (integration interval: 42.5 to 43 eV) extracted from the first-principles calculation and three-band model simulations for different matrix elements are compared. A value of $p_{vc}^2=0.02$ a.u. reproduces the first-principles simulation best.

B.2.5.1 Intra- and Inter-Band Limit

The advantage of this three-band model is that *intra*-band and *inter*-band transitions are described by different matrix elements of the Hamiltonian in equation (B.11). On one hand, *intra*-band motion is described by the modification of the single-particle energy levels, which are given by the diagonal elements. The change of the energies is due to the crystal momentum shift, $\hbar\mathbf{K}(t) = \hbar\mathbf{k} + \mathbf{A}(t)/c$. On the other hand, *inter*-band transitions are described via off-diagonal elements. In the main text, we investigate the *intra*-band transition limit by neglecting the off-diagonal elements in the Hamiltonian (Fig. 5.4(c) of the main manuscript) and the *inter*-band transition limit by neglecting the modification of the single-particle energies (Fig. 5.4(d) of the main manuscript).

B.2.5.2 Heavy-Hole Valence Band

As mentioned above, we assume the light-hole mass for the VB in the three-band model calculations. To justify our choice, we compare here the response of the model with the (a) light-hole VB and (b) heavy-hole VB. To investigate the VB response, we set the matrix element between core level and CB, $p_{dc'}$, to zero.

As was done for the light-hole band, we find the momentum matrix element p_{vc} for the heavy-hole band, which reproduces the first-principles result best. We find that a p_{vc}^2 of 0.01 a.u. yields the best match. Figure B.10 shows the VB response computed for both, light-hole and heavy-hole, cases. By comparison with the corresponding decomposition of the first-principles signal (Fig. B.8(d)), one finds that the signal with the light-hole band yields a better agreement; i.e., it reproduces correctly the wider distribution in the long-lasting component, and the V-shaped structure in the transient signal.

Based on this analysis, we chose the light-hole band instead of the heavy-hole band in the three-band simulations.

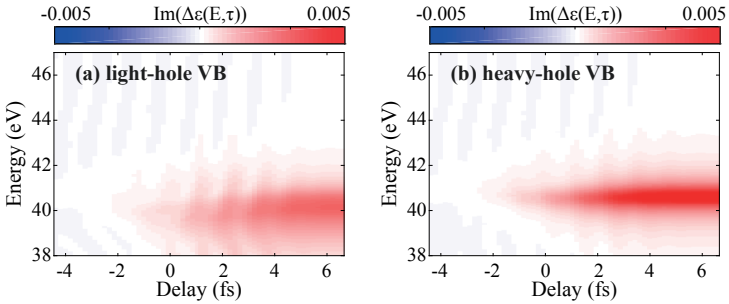


Figure B.10: Light-hole vs. heavy-hole valence band. Comparison of the valence band responses from a three-band model including (a) a light-hole and (b) a heavy-hole valence band, respectively.

B.2.5.3 Conduction Band Population

The population of the CB discussed in the main manuscript is defined by the projection of the time-dependent wave function $u_k(r, t)$ onto the instantaneous eigenstate of the CB, $u_{ck}^H(r, t)$:

$$n_{CB}(t) = \frac{2}{(2\pi)^3} \int dk \left| \langle u_{ck}^H(t) | u_k(t) \rangle \right|^2 = \frac{2}{(2\pi)^3} \int dk |c_{ck}(t)|^2, \quad (\text{B.14})$$

where $c_{ck}(t)$ is the CB coefficient derived from equation (B.11). To investigate only the population dynamics between VB and CB in Fig. 5.5 of the main manuscript, we set both p_{dv} and p_{dc} to zero.

B.2.6 Spin-Orbit Splitting

The As- $3d$ core level is divided into the $3d_{5/2}$ and $3d_{3/2}$ states due to the spin-orbit splitting. The level separation is 0.68 eV [131]. As the probe pulse can excite electrons from both core levels to the bandgap region, the measured signal can actually be seen as a superposition of two ATAS traces. In our simulations, no splitting is taken into account. Only one core level lying 40.73 eV below the valence band maximum is included [95]. To estimate the influence of the splitting on the calculated signal, we can look at

$$\Delta\varepsilon_{SO}(E, \tau) = 6 \cdot \text{Im}(\Delta\varepsilon(E + \frac{\Delta E_{SO}}{2}, \tau)) + 4 \cdot \text{Im}(\Delta\varepsilon(E - \frac{\Delta E_{SO}}{2}, \tau)), \quad (\text{B.15})$$

where $\Delta\varepsilon(E, \tau)$ is the simulated change of the dielectric function without splitting. E and τ describe the energy and delay dependence. ΔE_{SO} is the energy splitting of the core levels. The pre-factors 6 and 4 represent the degeneracy of the two core levels. By comparing the first-principles calculations without (Fig. B.11(a)) and with (Fig. B.11(b)) the splitting included, one finds that the core level splitting does not have a significant influence on the main features of the transient and long-lasting signal. It mainly results in an energy averaging. Therefore, we neglected the spin-orbit splitting in all calculations shown in this manuscript.

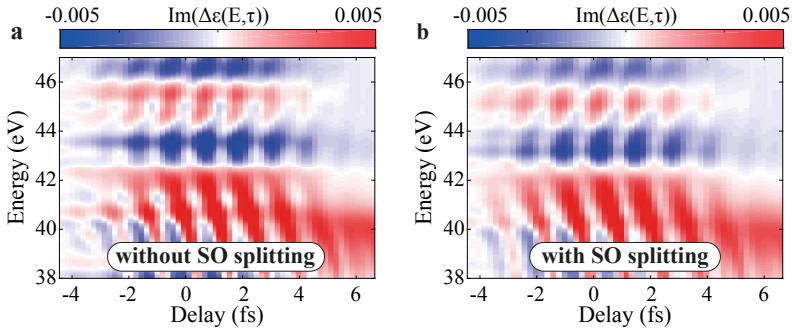


Figure B.11: Influence of core-level splitting. First-principles simulation (a) without and (b) with included spin-orbit splitting of the As- $3d$ core level. As one can see, the splitting results only in an energy averaging of the signal without any significant influence on the main features.

B.2.7 Multi-Photon Resonant Pump Regime

Using our simplified 3-band model, we calculated the number of carriers excited into the conduction band of GaAs ($E_{gap} = 1.52$ eV) for the case of a multi-photon resonant pump pulse. The pump photon energy used in the following is $1.52/3$ eV. The pump intensity has been set to 10^{10} W/cm². The corresponding Keldysh parameter is ~ 1.55 , which suggests that multi-photon excitation is more likely to occur than tunneling excitation.

In Fig. B.12, we show the corresponding conduction band population for the full model, including both transition types, and for the inter-band-only case on a linear (a) and logarithmic (b) axis. As in the resonant pump regime, we can clearly see that including intra-band motion results in an enhanced injection rate.

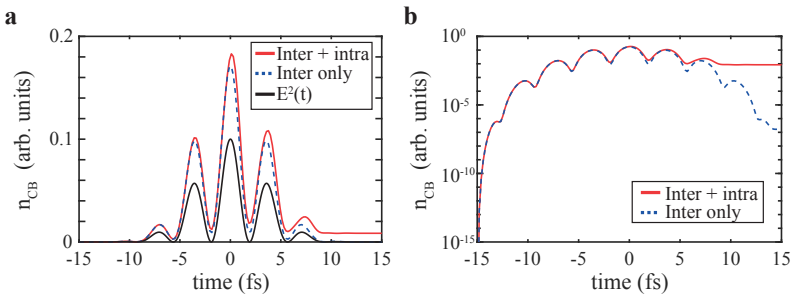


Figure B.12: Number of carriers excited into the conduction band of GaAs by a 3-photon resonant pump pulse. The black solid line in (a) illustrates the temporal shape of the pump intensity. Including intra-band motion into the simulations results in an enhancement of the number of excited carriers as in the single-photon resonant pump regime. In (b), the CB population is plotted on a logarithmic scale.

Bibliography

- [1] F. Krausz and M. Ivanov. Attosecond physics. *Reviews of Modern Physics*, 81(1):163–234, 2009.
- [2] P. Krehl and S. Engemann. August Toepler - The first who visualized shock waves. *Shock Waves*, 5:1–18, 1995.
- [3] T. H. Maiman. Stimulated Optical Radiation in Ruby. *Nature*, 187(4736):493–494, 1960.
- [4] G. Steinmeyer, D. H. Sutter, L. Gallmann, N. Matuschek, and U. Keller. Frontiers in Ultrashort Pulse Generation: Pushing the Limits in Linear and Nonlinear Optics. *Science*, 286(5444):1507–1512, 1999.
- [5] M. Dantus, M. J. Rosker, and A. H. Zewail. Real-time femtosecond probing of "transition states" in chemical reactions. *The Journal of Chemical Physics*, 87(4):2395–2397, 1987.
- [6] F. C. De Schryver, S. De Feyter, and G. Schweitzer. *Femtochemistry*, volume 3. Wiley, Weinheim, FRG, 2001.
- [7] P. M. Paul, E. S. Toma, P. Breger, G. Mullot, F. Augé, Ph. Balcou, H. G. Muller, and P. Agostini. Observation of a Train of Attosecond Pulses from High Harmonic Generation. *Science*, 292(5522):1689–1692, 2001.
- [8] A. McPherson, G. Gibson, H. Jara, U. Johann, T. S. Luk, I. A. McIntyre, K. Boyer, and C. K. Rhodes. Studies of multiphoton production of vacuum-ultraviolet radiation in the rare gases. *Journal of the Optical Society of America B*, 4(4):595–601, 1987.
- [9] M. Ferray, A. L'Huillier, X. F. Li, L. A. Lompré, G. Mainfray, and C. Manus. Multiple-harmonic conversion of 1064 nm radiation in rare gases. *Journal of Physics B: Atomic, Molecular and Optical Physics*, 21:L31–L35, 1988.

- [10] T. Gaumnitz, A. Jain, Y. Pertot, M. Huppert, I. Jordan, F. Ardana-Lamas, and H. J. Wörner. Streaking of 43-attosecond soft-X-ray pulses generated by a passively CEP-stable mid-infrared driver. *Opt. Express*, 25(22):27506–27518, 2017.
- [11] E. Goulielmakis, Z.-H. Loh, A. Wirth, R. Santra, N. Rohringer, V. S. Yakovlev, S. Zherebtsov, T. Pfeifer, A. M. Azzeer, M. F. Kling, S. R. Leone, and F. Krausz. Real-time observation of valence electron motion. *Nature*, 466(7307):739–743, 2010.
- [12] M. Schultze, M. Fieß, N. Karpowicz, J. Gagnon, M. Korbman, M. Hofstetter, S. Neppl, A. L. Cavalieri, Y. Komninos, Th. Mercouris, C. A. Nicolaides, R. Pazourek, S. Nagele, J. Feist, J. Burgdörfer, A. M. Azzeer, R. Ernstorfer, R. Kienberger, U. Kleineberg, E. Goulielmakis, F. Krausz, and V. S. Yakovlev. Delay in Photoemission. *Science*, 328(5986):1658–1662, 2010.
- [13] P. M. Kraus, B. Mignolet, D. Baykusheva, A. Rupenyan, L. Horný, E. F. Penka, G. Grassi, O. I. Tolstikhin, J. Schneider, F. Jensen, L. B. Madsen, A. D. Bandrauk, F. Remacle, and H. J. Wörner. Measurement and laser control of attosecond charge migration in ionized iodoacetylene. *Science*, 350(6262):790–795, 2015.
- [14] F. Calegari, D. Ayuso, A. Trabattoni, L. Belshaw, S. De Camillis, S. Anumula, F. Frassetto, L. Poletto, A. Palacios, P. Decleva, J. B. Greenwood, F. Martín, and M. Nisoli. Ultrafast electron dynamics in phenylalanine initiated by attosecond pulses. *Science*, 346(6207):336–339, 2014.
- [15] A. L. Cavalieri, N. Müller, Th. Uphues, V. S. Yakovlev, A. Baltuška, B. Horvath, B. Schmidt, L. Blümel, R. Holzwarth, S. Hendel, M. Drescher, U. Kleineberg, P. M. Echenique, R. Kienberger, F. Krausz, and U. Heinzmann. Attosecond spectroscopy in condensed matter. *Nature*, 449(7165):1029–1032, 2007.
- [16] Z. Tao, C. Chen, T. Szilvási, M. Keller, M. Mavrikakis, H. Kapteyn, and M. Murnane. Direct time-domain observation of attosecond final-state lifetimes in photoemission from solids. *Science*, 353(6294):62–67, 2016.
- [17] L. Kasmi, M. Lucchini, L. Castiglioni, P. Kliuiev, J. Osterwalder, M. Hengsberger, L. Gallmann, P. Krüger, and U. Keller. Effective mass effect in attosecond electron transport. *Optica*, 4(12):1492–1497, 2017.
- [18] F. Siek, S. Neb, P. Bartz, M. Hensen, C. Strüber, S. Fiechter, M. Torrent-Sucarrat, V. M. Silkin, E. E. Krasovskii, N. M. Kabachnik, S. Fritzsche, R. D. Muiño, P. M. Echenique, A. K. Kazansky,

- N. Müller, W. Pfeiffer, and U. Heinzmann. Angular momentum-induced delays in solid-state photoemission enhanced by intra-atomic interactions. *Science*, 357(6357):1274–1277, 2017.
- [19] M. Schultze, E. M. Bothschafter, A. Sommer, S. Holzner, W. Schweinberger, M. Fiess, M. Hofstetter, R. Kienberger, V. Apalkov, V. S. Yakovlev, M. I. Stockman, and F. Krausz. Controlling dielectrics with the electric field of light. *Nature*, 493(7430):75–78, 2013.
- [20] M. Schultze, K. Ramasesha, C. D. Pemmaraju, S. A. Sato, D. Whitmore, A. Gandman, J. S. Prell, L. J. Borja, D. Prendergast, K. Yabana, D. M. Neumark, and S. R. Leone. Attosecond band-gap dynamics in silicon. *Science*, 346(6215):1348–1352, 2014.
- [21] H. Mashiko, K. Oguri, T. Yamaguchi, A. Suda, and H. Gotoh. Petahertz optical drive with wide-bandgap semiconductor. *Nature Physics*, 12(8):741–745, 2016.
- [22] M. Lucchini, S. A. Sato, A. Ludwig, J. Herrmann, M. Volkov, L. Kasmi, Y. Shinohara, K. Yabana, L. Gallmann, and U. Keller. Attosecond dynamical Franz-Keldysh effect in polycrystalline diamond. *Science*, 353(6302):916 – 919, 2016.
- [23] P. Hommelhoff and M. F. Kling. *Attosecond Nanophysics*. Wiley-VCH Verlag GmbH & Co. KGaA, Weinheim, Germany, 2014.
- [24] X. Mei, W. Yoshida, M. Lange, J. Lee, J. Zhou, P. H. Liu, K. Leong, A. Zamora, J. Padilla, S. Sarkozy, R. Lai, and W. R. Deal. First Demonstration of Amplification at 1 THz Using 25-nm InP High Electron Mobility Transistor Process. *IEEE Electron Device Letters*, 36(4):327–329, 2015.
- [25] D. Golde, T. Meier, and S. W. Koch. High harmonics generated in semiconductor nanostructures by the coupled dynamics of optical inter- and intraband excitations. *Physical Review B*, 77(7):075330, 2008.
- [26] S. Ghimire, A. D. DiChiara, E. Sistrunk, P. Agostini, L. F. DiMauro, and D. A. Reis. Observation of high-order harmonic generation in a bulk crystal. *Nature Physics*, 7(2):138–141, 2011.
- [27] L. M. Malard, K. Fai Mak, A. H. Castro Neto, N. M. R. Peres, and T. F. Heinz. Observation of intra- and inter-band transitions in the transient optical response of graphene. *New Journal of Physics*, 15:015009, 2013.
- [28] I. Al-Naib, J. E. Sipe, and M. M. Dignam. High harmonic generation in undoped graphene: Interplay of inter- and intraband dynamics. *Physical Review B*, 90(24):245423, 2014.

- [29] T. T. Luu, M. Garg, S. Yu. Kruchinin, A. Moulet, M. Th. Hassan, and E. Goulielmakis. Extreme ultraviolet high-harmonic spectroscopy of solids. *Nature*, 521:498–502, 2015.
- [30] M. S. Wismer, S. Yu. Kruchinin, M. Ciappina, M. I. Stockman, and V. S. Yakovlev. Strong-Field Resonant Dynamics in Semiconductors. *Physical Review Letters*, 116(19):197401, 2016.
- [31] T. Paasch-Colberg, S. Yu. Kruchinin, Ö. Saglam, S. Kapser, S. Cabrini, S. Muehlbrandt, J. Reichert, J. V. Barth, R. Ernstorfer, R. Kienberger, V. S. Yakovlev, N. Karpowicz, and A. Schiffrin. Sub-cycle optical control of current in a semiconductor: from the multiphoton to the tunneling regime. *Optica*, 3(12):1358–1361, 2016.
- [32] A. Picón, L. Plaja, and J. Biegert. Attosecond x-ray transient absorption in condensed-matter: a core-state-resolved Bloch model. *New Journal of Physics*, 21(4):043029, 2019.
- [33] J. Itatani, J. Lavesque, D. Zeidler, H. Niikura, H. Pépin, J. C. Kieffer, P. B. Corkum, and D. M. Villeneuve. Tomographic imaging of molecular orbitals. *Nature*, 432(7019):867–871, 2004.
- [34] T. T. Luu, Z. Yin, A. Jain, T. Gaumnitz, Y. Pertot, J. Ma, and H. J. Wörner. Extreme-ultraviolet high-harmonic generation in liquids. *Nature Communications*, 9:3723, 2018.
- [35] P. B. Corkum. Plasma Perspective on Strong Field Multiphoton Ionization. *Physical Review Letters*, 71(13):1994–1997, 1993.
- [36] S. L. Cousin, F. Silva, S. Teichmann, M. Hemmer, B. Buades, and J. Biegert. High-flux table-top soft x-ray source driven by sub-2-cycle, CEP stable, 185- μm 1-kHz pulses for carbon K-edge spectroscopy. *Optics Letters*, 39(18):5383–5386, 2014.
- [37] J. Tate, T. Augustine, H. G. Muller, P. Salières, P. Agostini, and L. F. DiMauro. Scaling of Wave-Packet Dynamics in an Intense Midinfrared Field. *Physical Review Letters*, 98(1):013901, 2007.
- [38] M. Hentschel, R. Kienberger, Ch. Spielmann, G. A. Reider, N. Milosevic, T. Brabec, P. Corkum, U. Heinzmann, M. Drescher, and F. Krausz. Attosecond metrology. *Nature*, 414(6863):509–513, 2001.
- [39] G. Sansone, E. Benedetti, F. Calegari, C. Vozzi, L. Avaldi, R. Flammini, L. Poletto, P. Villoresi, C. Altucci, R. Velotta, S. Stagira, S. De Silvestri, and M. Nisoli. Isolated Single-Cycle Attosecond Pulses. *Science*, 314(5798):443–446, 2006.
- [40] T. Pfeifer, A. Jullien, M. J. Abel, P. M. Nagel, L. Gallmann, D. M. Neumark, and S. R. Leone. Generating coherent broadband continuum soft-x-ray radiation by attosecond ionization gating. *Optics Express*, 15(25):17120, 2007.

-
- [41] J. A. Wheeler, A. Borot, S. Monchocé, H. Vincenti, A. Ricci, A. Malvache, R. Lopez-Martens, and F. Quéré. Attosecond lighthouses from plasma mirrors. *Nature Photonics*, 6(12):829–833, 2012.
- [42] K. S. Budil, P. Salières, A. L’Huillier, T. Ditmire, and M. D. Perry. Influence of ellipticity on harmonic generation. *Physical Review A*, 48(5):R3437–R3440, 1993.
- [43] S. Haessler, B. Fabre, J. Higuette, J. Caillat, T. Ruchon, P. Breger, B. Carré, E. Constant, A. Maquet, E. Mével, P. Salières, R. Taïeb, and Y. Mairesse. Phase-resolved attosecond near-threshold photoionization of molecular nitrogen. *Physical Review A*, 80(1):011404, 2009.
- [44] R. Locher, L. Castiglioni, M. Lucchini, M. Greif, L. Gallmann, J. Osterwalder, M. Hengsberger, and U. Keller. Energy-dependent photoemission delays from noble metal surfaces by attosecond interferometry. *Optica*, 2(5):405–410, 2015.
- [45] H. G. Muller. Reconstruction of attosecond harmonic beating by interference of two-photon transitions. *Applied Physics B: Lasers and Optics*, 74:S17–S21, 2002.
- [46] M. Sabbar, S. Heuser, R. Boge, M. Lucchini, T. Carette, E. Lindroth, L. Gallmann, C. Cirelli, and U. Keller. Resonance Effects in Photoemission Time Delays. *Physical Review Letters*, 115(13):133001, 2015.
- [47] L. Cattaneo, J. Vos, M. Lucchini, L. Gallmann, C. Cirelli, and U. Keller. Comparison of attosecond streaking and RABBITT. *Optics Express*, 24(25):29060–29076, 2016.
- [48] C. Cirelli, M. Sabbar, S. Heuser, R. Boge, M. Lucchini, L. Gallmann, and U. Keller. Energy-Dependent Photoemission Time Delays of Noble Gas Atoms Using Coincidence Attosecond Streaking. *IEEE Journal on Selected Topics in Quantum Electronics*, 21(5):8700307, 2015.
- [49] F. Schlaepfer, A. Ludwig, M. Lucchini, L. Kasmí, M. Volkov, L. Gallmann, and U. Keller. Gouy phase shift for annular beam profiles in attosecond experiments. *Optics Express*, 25(4):3646–3655, 2017.
- [50] J. M. Dahlström, A. L’Huillier, and A. Maquet. Introduction to attosecond delays in photoionization. *Journal of Physics B: Atomic, Molecular and Optical Physics*, 45(18):183001, 2012.
- [51] E. P. Wigner. Lower Limit for the Energy Derivative of the Scattering Phase Shift. *Physical Review*, 98(1):145–147, 1955.
- [52] M. Lewenstein, Ph. Balcou, M. Yu. Ivanov, A. L. Huillier, and P. B. Corkum. Theory of high-harmonic generation by low-frequency laser fields. *Physical Review A*, 49(3):2117–2132, 1994.

- [53] J. Itatani, F. Quéré, G. L. Yudin, M. Yu. Ivanov, F. Krausz, and P. B. Corkum. Attosecond Streak Camera. *Physical Review Letters*, 88(17):173903, 2002.
- [54] F. Quéré, J. Itatani, G. L. Yudin, and P. B. Corkum. Attosecond Spectral Shearing Interferometry. *Physical Review Letters*, 90(7):073902, 2003.
- [55] Y. Mairesse and F. Quéré. Frequency-resolved optical gating for complete reconstruction of attosecond bursts. *Physical Review A - Atomic, Molecular, and Optical Physics*, 71(1):011401, 2005.
- [56] J. Gagnon and V. S. Yakovlev. The robustness of attosecond streaking measurements. *Optics Express*, 17(20):17678–17693, 2009.
- [57] P. D. Keathley, S. Bhardwaj, J. Moses, G. Laurent, and F. X. Kärtner. Volkov transform generalized projection algorithm for attosecond pulse characterization. *New Journal of Physics*, 18(7):073009, 2016.
- [58] M. Lucchini, M. H. Brüggmann, A. Ludwig, L. Gallmann, U. Keller, and T. Feurer. Ptychographic reconstruction of attosecond pulses. *Optics Express*, 23(23):29502–29513, 2015.
- [59] F. Schlaepfer, M. Lucchini, S. A. Sato, M. Volkov, L. Kasmi, N. Hartmann, A. Rubio, L. Gallmann, and U. Keller. Attosecond optical-field-enhanced carrier injection into the GaAs conduction band. *Nature Physics*, 14:560–564, 2018.
- [60] M. Volkov, S. A. Sato, F. Schlaepfer, L. Kasmi, N. Hartmann, M. Lucchini, L. Gallmann, A. Rubio, and U. Keller. Attosecond screening dynamics mediated by electron-localization in transition metals. *Nature Physics*, (doi.org/10.1038/s41567-019-0602-9), 2019.
- [61] B. L. Henke, E. M. Gullikson, and J. C. Davis. X-ray interactions: Photoabsorption, scattering, transmission, and reflection at E = 50–30000 eV, Z = 1–92. *Atomic Data and Nuclear Data Tables*, 54(2):181–342, 1993.
- [62] Center for X-ray Optics, "Filter transmission", http://henke.lbl.gov/optical_constants/filter2.html, 2019.
- [63] I. A. Artioukov, B. R. Benware, J. J. Rocca, M. Forsythe, Yu. A. Uspenkii, and A. V. Vinogradov. Determination of XUV Optical Constants by Reflectometry Using a High-Repetition Rate 46.9-nm Laser. *IEEE Journal on Selected Topics in Quantum Electronics*, 5(6):1495–1501, 1999.
- [64] D. E. Aspnes, S. M. Kelso, R. A. Logan, and R. Bhat. Optical properties of $\text{Al}_x\text{Ga}_{1-x}\text{As}$. *Journal of Applied Physics*, 60(2):754–767, 1986.

- [65] C. P. Hauri, W. Kornelis, F. W. Helbing, A. Heinrich, A. Couairon, A. Mysyrowicz, J. Biegert, and U. Keller. Generation of intense, carrier-envelope phase-locked few-cycle laser pulses through filamentation. *Applied Physics B: Lasers and Optics*, 79(6):673–677, 2004.
- [66] C. P. Hauri, A. Guandalini, P. Eckle, W. Kornelis, J. Biegert, and U. Keller. Generation of intense few-cycle laser pulses through filamentation - parameter dependence. *Optics Express*, 13(19):7541–7547, 2005.
- [67] C. Vozzi, M. Nisoli, G. Sansone, S. Stagira, and S. De Silvestri. Optimal spectral broadening in hollow-fiber compressor systems. *Applied Physics B: Lasers and Optics*, 80(3):285–289, 2005.
- [68] R. Locher, M. Lucchini, J. Herrmann, M. Sabbar, M. Weger, A. Ludwig, L. Castiglioni, M. Greif, M. Hengsberger, L. Gallmann, and U. Keller. Versatile attosecond beamline in a two-foci configuration for simultaneous femto-resolved measurements. *Review of Scientific Instruments*, 85(1):013113, 2014.
- [69] K. T. Kim, C. M. Kim, M.-G. Baik, G. Umesh, and C. H. Nam. Single sub-50-attosecond pulse generation from chirp-compensated harmonic radiation using material dispersion. *Physical Review A*, 69:051805(R), 2004.
- [70] R. López-Martens, K. Varjú, P. Johnsson, J. Mauritsson, Y. Mairesse, P. Salières, M. B. Gaarde, K. J. Schafer, A. Persson, S. Svanberg, C.-G. Wahlström, and A. L’Huillier. Amplitude and Phase Control of Attosecond Light Pulses. *Physical Review Letters*, 94(3):033001, 2005.
- [71] A. Ludwig, E. Liberatore, J. Herrmann, L. Kasmi, P. López-Tarifa, L. Gallmann, U. Rothlisberger, U. Keller, and Matteo Lucchini. Ultrafast Relaxation Dynamics of the Ethylene Cation $C_2H_4^+$. *The Journal of Physical Chemistry Letters*, (7):1901–1906, 2016.
- [72] M. Chini, H. Mashiko, H. Wang, S. Chen, C. Yun, S. Scott, S. Gilbertson, and Z. Chang. Delay control in attosecond pump-probe experiments. *Optics Express*, 17(24):21459–21464, 2009.
- [73] J. G. E. Harris, D. D. Awschalom, K. D. Maranowski, and A. C. Gosard. Fabrication and characterization of 100-nm-thick GaAs cantilevers. *Review of Scientific Instruments*, 67(10):3591–3593, 1996.
- [74] J. Liu, K. Usami, A. Naesby, T. Bagci, E. S. Polzik, P. Lodahl, and S. Stobbe. High-Q optomechanical GaAs nanomembranes. *Applied Physics Letters*, 99(24):243102, 2011.
- [75] G. C. DeSalvo, W. F. Tseng, and J. Comas. Etch Rates and Selectivities of Citric Acid/Hydrogen Peroxide on GaAs, $Al_{0.3}Ga_{0.7}As$, $In_{0.2}Ga_{0.8}As$, $In_{0.53}Ga_{0.47}As$, $In_{0.52}Al_{0.48}As$, and InP. *J. Electrochem. Soc.*, 139(3):831–835, 1992.

- [76] L. G. Gouy. Sur une propriété nouvelle des ondes lumineuses. *C. R. Acad. Sci. Paris.*, 110:1251–1253, 1890.
- [77] Zenghu Chang. *Fundamentals of Attosecond Optics*. Taylor and Francis Group, LLC, 2011.
- [78] F. Lindner, G. G. Paulus, H. Walther, A. Baltuška, E. Goulielmakis, M. Lezius, and F. Krausz. Gouy Phase Shift for Few-Cycle Laser Pulses. *Physical Review Letters*, 92(11):113001, 2004.
- [79] N. Shivaram, A. Roberts, L. Xu, and A. Sandhu. In situ spatial mapping of Gouy phase slip for high-detail attosecond pump-probe measurements. *Optics Letters*, 35(20):3312–3314, 2010.
- [80] Lukas Gallmann, Claudio Cirelli, and Ursula Keller. Attosecond Science: Recent Highlights and Future Trends. *Annual Review of Physical Chemistry*, 63(1):447–469, may 2012.
- [81] K. Klünder, J. M. Dahlström, M. Gisselbrecht, T. Fordell, M. Swoboda, D. Guénot, P. Johnsson, J. Caillat, J. Mauritsson, A. Maquet, R. Taïeb, and A. L’Huillier. Probing Single-Photon Ionization on the Attosecond Time Scale. *Physical Review Letters*, 106(14):143002, 2011.
- [82] C. Palatchi, J. M. Dahlström, A. S. Kheifets, I. A. Ivanov, D. M. Canaday, P. Agostini, and L. F. DiMauro. Atomic delay in helium, neon, argon and krypton. *Journal of Physics B: Atomic, Molecular and Optical Physics*, 47(24):245003, 2014.
- [83] D. Guénot, D. Kroon, E. Balogh, E. W. Larsen, M. Kotur, M. Miranda, T. Fordell, P. Johnsson, J. Mauritsson, M. Gisselbrecht, K. Varjü, C. L. Arnold, T. Carette, A. S. Kheifets, E. Lindroth, A. L’Huillier, and J. M. Dahlström. Measurements of relative photoemission time delays in noble gas atoms. *Journal of Physics B: Atomic, Molecular and Optical Physics*, 47(24):245602, 2014.
- [84] S. Heuser, Á. Jiménez Galán, C. Cirelli, C. Marante, M. Sabbar, R. Boge, M. Lucchini, L. Gallmann, I. Ivanov, A. S. Kheifets, J. M. Dahlström, E. Lindroth, L. Argenti, F. Martín, and U. Keller. Angular dependence of photoemission time delay in helium. *Physical Review A*, 94(6):063409, 2016.
- [85] M. Ossiander, F. Siegrist, V. Shirvanyan, R. Pazourek, A. Sommer, T. Latka, A. Guggenmos, S. Nagele, J. Feist, J. Burgdörfer, R. Kienberger, and M. Schultze. Attosecond correlation dynamics. *Nature Physics*, 13(3):280–285, 2017.
- [86] M. Lucchini, L. Castiglioni, L. Kasmi, P. Kliuiev, A. Ludwig, M. Greif, J. Osterwalder, M. Hengsberger, L. Gallmann, and U. Keller. Light-Matter Interaction at Surfaces in the Spatiotemporal Limit of Macroscopic Models. *Physical Review Letters*, 115(13):137401, 2015.

- [87] S. Feng and H. G. Winful. Physical origin of the Gouy phase shift. *Optics Letters*, 26(8):485–487, 2001.
- [88] F. Krausz and M. I. Stockman. Attosecond metrology: from electron capture to future signal processing. *Nature Photonics*, 8(3):205–213, 2014.
- [89] M. Zürch, H.-T. Chang, L. J. Borja, P. M. Kraus, S. K. Cushing, A. Gandman, C. J. Kaplan, M. H. Oh, J. S. Prell, D. Prendergast, C. D. Pemmaraju, D. M. Neumark, and S. R. Leone. Direct and simultaneous observation of ultrafast electron and hole dynamics in germanium. *Nature communications*, 8:15734, 2017.
- [90] Mi. Zürch, H.-T. Chang, P. M. Kraus, S. K. Cushing, L. J. Borja, A. Gandman, C. J. Kaplan, M. H. Oh, J. S. Prell, D. Prendergast, C. D. Pemmaraju, D. M. Neumark, and S. R. Leone. Ultrafast carrier thermalization and trapping in silicon-germanium alloy probed by extreme ultraviolet transient absorption spectroscopy. *Structural Dynamics*, 4(4):044029, 2017.
- [91] Y. Ji, B. Calderon, Y. Han, P. Cueva, N. R. Jungwirth, H. A. Alsalman, J. Hwang, G. D. Fuchs, D. A. Muller, and M. G. Spencer. Chemical Vapor Deposition Growth of Large Single-Crystal Mono-, Bi-, Tri-Layer Hexagonal Boron Nitride and Their Interlayer Stacking. *ACS Nano*, 11(12):12057–12066, 2017.
- [92] J. Li, X. Ren, Y. Yin, K. Zhao, A. Chew, Y. Cheng, E. Cunningham, Y. Wang, S. Hu, Y. Wu, M. Chini, and Z. Chang. 53-attosecond X-ray pulses reach the carbon K-edge. *Nature Communications*, 8:186, 2017.
- [93] P. J. Ireland, L. L. Kazmerski, and R. F. Fisher. X-ray photoemission spectra for $\text{Al}_x\text{Ga}_{1-x}\text{As}$. *Journal of Vacuum Science & Technology A*, 2(2):1129–1131, 1984.
- [94] T. Kendelewicz, P. H. Mahowald, K. A. Bartness, C. E. McCants, I. Lindau, and W. E. Spicer. Surface shifts in the In 4d and P 2p core-level spectra of InP(110). *Physical Review B*, 36(12):6543–6546, 1987.
- [95] E. A. Kraut, R. W. Grant, J. R. Waldrop, and S. P. Kowalczyk. Precise Determination of the Valence-Band Edge in X-Ray Photoemission Spectra: Application to Measurement of Semiconductor Interface Potentials. *Physical Review Letters*, 44(24):1620–1623, 1980.
- [96] S. P. Kowalczyk, W. J. Schaffer, E. A. Kraut, and R. W. Grant. Determination of the InAs-GaAs(100) heterojunction band discontinuities by x-ray photoelectron spectroscopy (XPS). *Journal of Vacuum Science and Technology*, 20(3):705–708, 1982.

- [97] M. Fondell, M. Gorgoi, M. Boman, and A. Lindblad. An HAXPES study of Sn, SnS, SnO and SnO₂. *Journal of Electron Spectroscopy and Related Phenomena*, 195:195–199, 2014.
- [98] P. John, T. Miller, and T.-C. Chiang. InSb(100) reconstructions probed with core-level photoemission. *Physical Review B*, 39(3):1730–1737, 1989.
- [99] A. K. Saxena. The conduction band structure and deep levels in Ga_{1-x}Al_xAs alloys from a high-pressure experiment. *Journal of Physics C: Solid State Physics*, 13:4323–4334, 1980.
- [100] J. R. Chelikowsky and M. L. Cohen. Nonlocal pseudopotential calculations for the electronic structure of eleven diamond and zincblende semiconductors. *Physical Review B*, 14(2):556–582, 1976.
- [101] S. A. Sato, K. Yabana, Y. Shinohara, T. Otake, and G. F. Bertsch. Numerical pump-probe experiments of laser-excited silicon in nonequilibrium phase. *Physical Review B*, 89(6):064304, 2014.
- [102] S. B. Desai, S. R. Madhupathy, A. B. Sachid, J. P. Llinas, Q. Wang, G. H. Ahn, G. Pitner, M. J. Kim, J. Bokor, C. Hu, H.-S. P. Wong, and A. Javey. MoS₂ transistors with 1-nanometer gate lengths. *Science*, 354(6308):99–102, 2016.
- [103] A. Sommer, E. M. Bothschafter, S. A. Sato, C. Jakubeit, T. Latka, O. Razskazovskaya, H. Fattahi, M. Jobst, W. Schweinberger, V. Shirvanyan, V. S. Yakovlev, R. Kienberger, K. Yabana, N. Karpowicz, M. Schultze, and F. Krausz. Attosecond nonlinear polarization and light-matter energy transfer in solids. *Nature*, 534:86–90, 2016.
- [104] A. Ludwig, J. Maurer, B. W. Mayer, C. R. Phillips, L. Gallmann, and U. Keller. Breakdown of the Dipole Approximation in Strong-Field Ionization. *Physical Review Letters*, 113(24):243001, 2014.
- [105] I. Vurgaftman, J. R. Meyer, and L. R. Ram-Mohan. Band parameters for III-V compound semiconductors and their alloys. *Journal of Applied Physics*, 89(11):5815–5875, 2001.
- [106] M. C. Beard, G. M. Turner, and C. A. Schmuttenmaer. Transient photoconductivity in GaAs as measured by time-resolved terahertz spectroscopy. *Physical Review B*, 62(23):15764–15777, 2000.
- [107] W. V. Houston. Acceleration of Electrons in a Crystal Lattice. *Physical Review*, 57:184–186, 1940.
- [108] A. Srivastava, R. Srivastava, J. Wang, and J. Kono. Laser-Induced Above-Band-Gap Transparency in GaAs. *Physical Review Letters*, 93(15):157401, 2004.

- [109] F. Novelli, D. Fausti, F. Giusti, F. Parmigiani, and M. Hoffmann. Mixed regime of light-matter interaction revealed by phase sensitive measurements of the dynamical Franz-Keldysh effect. *Scientific reports*, 3:1227, 2013.
- [110] J. S. Bakos. AC stark effect and multiphoton processes in atoms. *Physics Reports*, 31(3):209–235, 1977.
- [111] J. M. Dallesasse and N. Holonyak. Oxidation of Al-bearing III-V materials: A review of key progress. *Journal of Applied Physics*, 113(5):051101, 2013.
- [112] A. R. Sugg, N. Holonyak, J. E. Baker, F. A. Kish, and J. M. Dallesasse. Native oxide stabilization of AlAs-GaAs heterostructures. *Applied Physics Letters*, 58(11):1199–1201, 1991.
- [113] R. Ludeke, L. Ley, and K. Ploog. Valence and core level photoemission spectra of $\text{Al}_x\text{Ga}_{1-x}\text{As}$. *Solid State Communications*, 28(1):57–60, 1978.
- [114] J. A. Taylor. An XPS study of the oxidation of AlAs thin films grown by MBE. *Journal of Vacuum Science and Technology*, 20(3):751–755, 1982.
- [115] T. Otake, Y. Shinohara, S. A. Sato, and K. Yabana. Femtosecond time-resolved dynamical Franz-Keldysh effect. *Physical Review B*, 93(4):045124, 2016.
- [116] F. Schlaepfer, M. Volkov, N. Hartmann, A. Niedermayr, Z. Schumacher, L. Gallmann, and U. Keller. Phase stabilization of an attosecond beamline combining two IR colors. *Optics Express*, 27(16):22385–22392, 2019.
- [117] M. Huppert, I. Jordan, and H. J. Wörner. Attosecond beamline with actively stabilized and spatially separated beam paths. *Review of Scientific Instruments*, 86(12):123106, 2015.
- [118] M. Sabbar, S. Heuser, R. Boge, M. Lucchini, L. Gallmann, C. Cirelli, and U. Keller. Combining attosecond XUV pulses with coincidence spectroscopy. *Review of Scientific Instruments*, 85(10):103113, 2014.
- [119] Y. Pertot, C. Schmidt, M. Matthews, A. Chauvet, M. Huppert, V. Svoboda, A. von Conta, A. Tehlar, D. Baykusheva, J.-P. Wolf, and H. J. Wörner. Time-resolved x-ray absorption spectroscopy with a water window high-harmonic source. *Science*, 355(6322):264–267, 2017.
- [120] H. R. Telle, G. Steinmeyer, A. E. Dunlop, J. Stenger, D. H. Sutter, and U. Keller. Carrier-envelope offset phase control: A novel concept for absolute optical frequency measurement and ultrashort pulse generation. *Applied Physics B: Lasers and Optics*, 69(4):327–332, 1999.

- [121] W. Liu and S. L. Chin. Direct measurement of the critical power of femtosecond Ti:sapphire laser pulse in air. *Optics Express*, 13(15):5750–5755, 2005.
- [122] S. A. Sato, M. Lucchini, M. Volkov, F. Schlaepfer, L. Gallmann, U. Keller, and A. Rubio. Role of intraband transitions in photocarrier generation. *Physical Review B*, 98(3):035202, 2018.
- [123] D. E. Aspnes and A. A. Studna. Dielectric functions and optical parameters of Si, Ge, GaP, GaAs, GaSb, InP, InAs, and InSb from 1.5 to 6.0 eV. *Physical Review B*, 27(2):985–1009, 1983.
- [124] E. Runge and E. K. U. Gross. Density-Functional Theory for Time-Dependent Systems. *Physical Review Letters*, 52(12):997–1000, 1984.
- [125] Y. Hirokawa, T. Boku, S. A. Sato, and K. Yabana. Electron Dynamics Simulation with Time-Dependent Density Functional Theory on Large Scale Symmetric Mode Xeon Phi Cluster. *IEEE International Parallel and Distributed Processing Symposium Workshops (IPDPSW)*, pages 1202–1211, 2016.
- [126] F. Tran and P. Blaha. Accurate Band Gaps of Semiconductors and Insulators with a Semilocal Exchange–Correlation Potential. *Physical Review Letters*, 102(22):226401, 2009.
- [127] D. Koller, F. Tran, and P. Blaha. Improving the modified Becke–Johnson exchange potential. *Physical Review B*, 85(15):155109, 2012.
- [128] S. A. Sato and K. Yabana. Efficient basis expansion for describing linear and nonlinear electron dynamics in crystalline solids. *Physical Review B*, 89(22):224305, 2014.
- [129] J. B. Krieger and G. J. Iafrate. Time evolution of Bloch electrons in a homogeneous electric field. *Physical Review B*, 33(8):5494–5500, 1986.
- [130] P. Y. Yu and M. Cardona. *Fundamentals of Semiconductors*. Springer Verlag, 1996.
- [131] J. F. van der Veen, L. Smit, P. K. Larsen, and J. H. Neave. Core Level Binding Energy Shifts for Reconstructed GaAs(001) Surfaces. *Physica B+C*, 117-188:822–824, 1983.

Curriculum Vitæ

Name Fabian Schläpfer
Date of Birth 11th November 1989
Citizenship Switzerland

Education

Sep. 2015 - Aug. 2019 Doctoral studies in the Ultrafast Laser Physics group of Prof. Ursula Keller, Institute for Quantum Electronics, Department of Physics, ETH Zurich, Zurich, Switzerland.

Feb. 2013 - July 2014 MSc in Physics, ETH Zurich, Zurich, Switzerland.

Sep. 2009 - Jan. 2013 BSc in Physics, ETH Zurich, Zurich, Switzerland.

Aug. 2004 - July 2008 Matura, Kantonsschule Trogen, Trogen, Switzerland.

Research and Professional Experience

Sep. 2015 - Aug. 2019 Doctoral studies in the Ultrafast Laser Physics group of Prof. Ursula Keller, Institute for Quantum Electronics, Department of Physics, ETH Zurich, Zurich, Switzerland.
Attosecond Electron Dynamics in III-V Semiconductors

Sep. 2015 - Aug. 2019 Teaching assistant of the Department of Physics, ETH Zurich, Zurich, Switzerland.

Spring Semester 2014 Master thesis in the Advanced Semiconductor Quantum Materials group of Prof. Werner Wegscheider, Laboratory for Solid State Physics, Department of Physics, ETH Zurich, Zurich, Switzerland.
Photoluminescence Characterization of Semiconductor Samples grown by Molecular Beam Epitaxy

Spring Semester 2013 Semester thesis in the Ultrafast Laser Physics group of Prof. Ursula Keller, Institute for Quantum Electronics, Department of Physics, ETH Zurich, Zurich, Switzerland.
Optically Pumped Passive Soliton Mode-Locked Yb:KYW Laser

Sep. 2012 - Jan. 2013 Internship at Optotune, Dietikon, Switzerland.
Development, simulation and characterization of tunable lens prototypes

Acknowledgements

I would like to devote the last pages of this thesis to all those people who accompanied me on my ETH journey. This work would not have been possible without your support.

First of all, I would like to express my deepest gratitude to my family. You were a big support, even though you looked always very confused when I was talking about electrons and attoseconds. Another huge thank deserves my girlfriend Gioia. Spending my time with you was the best medicine to refill my batteries after frustrating measurement days. Thank you so much.

Obviously, the experiments performed during my last four years would not have been feasible without the whole attoline team. Many thanks go to Dr. Mikhail Volkov. Literally from the first day on, I was spending my time with you in the laboratory. I will not forget how we suffered to install this monster of a TOPAS. It was a big pleasure to work with you and I wish you all the best for your scientific career. I would also like to express special thanks to Dr. Matteo Lucchini for his support. I am very happy that we had at least one and a half years overlap. I learned amazing things from you ;-). Further, many thanks go to Dr. Lamia Kasmi. Your karaoke skills are crazy, but there is always a 50% chance that you hurt yourself. Many thanks go as well to Nadja Hartmann, your sport discipline is admirable, Zeno Schumacher, for taking care on the surface beast, Arthur Niedermayr, for your motivation to continue my work in FIRST, Sergej Neb, for the experience you brought into our team and finally to André Ludwig, for your amazing attoline-control-center software.

Further, I want to express special thanks to Dr. Matthias Golling for your enthusiasm and enormous knowledge about the growth of semiconductor structures. Whenever I came with some questions, you took your time to discuss them.

I will also keep all the other members of the ULP group in best memory. I would especially like to thank Luca Pedrelli for being the best office mate you could wish for. I am looking forward to meeting you in

Zanzibar ;-). Moreover, many thanks go to Francesco Saltarelli and Jaco Fuchs, for being amazing machine learning teammates, Dr. Jannie Vos, for all the beers and wines we had together, Dr. Laura Cattaneo, for being always happy, Dr. Nicolas Bigler, I am looking forward to the next festival with you, Dr. Cesare Alfieri, for doing beautiful SEM pictures of my samples, Dr. Dominik Waldburger, for all your sneaky pranks, Dr. Christopher Phillips, for sharing your enormous laser knowledge with me, Dr. Claudio Cirelli, for the coffee time in the morning, Dr. Florian Emaury, for teaching me how to become a lapper master, and to Ivan Graumann, for the good drinks during the ski weekend. Further, I would like to thank Dr. Jochen Maurer, Fabian Brunner, Benjamin Willenberg and Justinas Pupeikis for sharing the laboratory. The experimental setups you build are just impressive. Many thanks go also to all group members not explicitly mentioned. It was a pleasure to work with you. Let us keep in touch.

Further, I would like to thank Dr. Lukas Gallmann for your support and all the discussions we had.

Moreover, special thanks go to Shunsuke Sato for the excellent theory support. It was a huge pleasure to collaborate with you. You have always taken the time to answer my countless questions.

I would also like to thank Prof. Adrian Cavaliere for being the co-examiner of my doctor thesis.

Finally, I would like to express special thanks to Prof. Ursula Keller for giving me the opportunity to be part of the ULP group. I have learned so much during the last years and feel that I am now ready to leave ETH Zurich and start a new chapter in my life.



Zurich, August 2019